Sampling the Evolution of Solar System Cometoids

Thesis by
Qicheng Zhang

In Partial Fulfillment of the Requirements for the
Degree of
Doctor of Philosophy

CALIFORNIA INSTITUTE OF TECHNOLOGY
Pasadena, California

2024
Defended 2023 September 26

Qicheng Zhang
ORCID: 0000-0002-6702-191X

ACKNOWLEDGMENTS

I am privileged to have worked with my thesis advisor, Gregg Hallinan, whose expert guidance, unwavering support, and relentless encouragement to explore my interests has made possible the work contained herein and beyond. I am also grateful to Mike Brown, Katherine de Kleer, and Heather Knutson for serving on my thesis advisory committee and providing many interesting scientific discussions over the years leading up to this work, as well as to all members of both the planetary science and radio astronomy staff at Caltech for their work supporting this journey. This thesis furthermore incorporates the expertise and patience of numerous collaborators, including Quanzhi Ye, Karl Battams, Matthew Knight, Ludmilla Kolokolova, and others with whom I have been fortunate to have joined in pursuit of answers to many, often wacky yet enlightening questions. I also thank my friends and colleagues at Caltech, including Shreyas Vissapragada, Yayaati Chachan, Aida Behmard, and Harriet Brettle, for joining me on this planetary venture and making the experience an enjoyable one. I likewise thank Cameron Hummels and others on the astronomy outreach team, as well as Hesham Zaini, for many other adventures along the way. Finally, I give special thanks to my family, especially to my parents, for their enduring trust and support, without which none of these endeavors would have been possible.

ABSTRACT

Comets are commonly defined to be planetesimals visibly losing mass through volatile sublimation. In the solar system, such behavior characterizes but a brief stage in the overall evolution of these objects, as limited by their supply of accessible volatile materials and the often short dynamical lifetimes of orbits sufficiently near the Sun for said volatiles to actually volatilize. In this thesis, I explore the characteristics of several different types of "cometoids"—planetesimals visibly exhibiting comet-like mass loss sometime in their recent past, present, or near future—in both the outer and inner solar system at different stages in their physical and dynamical evolution. I first use stellar occultations—or rather, the lack thereof detected—to constrain their abundance of kilometer-scale objects in the Kuiper Belt, from which many comets are sourced. I then evaluate how the optical brightness, color, and polarization of dust ejected by a classical, currently active comet changes when exposed to the space environment in order to probe the material properties of its nucleus. Finally, I investigate an otherwise ordinary but active asteroid to explore how intense solar heating as it passes very near the Sun can volatilize its rocky surface to produce bright sodium emission explaining its comet-like behavior.

PUBLISHED CONTENT AND CONTRIBUTIONS

Zhang, Q., Battams, K., Ye, Q., Knight, M. M., & Schmidt, C. A. 2023a. Sodium Brightening of (3200) Phaethon near Perihelion. PSJ, 4, 70, doi: 10.3847/PSJ/acc866.
Q. Zhang formulated the main hypothesis as well as designed observations and developed models to test the hypothesis.

Zhang, Q., Hallinan, G. W., Saini, N. S., et al. 2023b. CHIMERA Occultation Constraints on the Abundance of Kilometer-scale Kuiper Belt Objects. AJ, 166, 242, doi: 10.3847/1538-3881/ad03e3.
Q. Zhang devised the data reduction procedure and performed the analysis.

Zhang, Q., Kolokolova, L., Ye, Q., & Vissapragada, S. 2022. Dust Evolution in the Coma of Distant, Inbound Comet C/2017 K2 (PANSTARRS). PSJ, 3, 135, doi: 10.3847/PSJ/ac6d58.
Q. Zhang designed the observation plan and led the analysis of the collected data.

TABLE OF CONTENTS

LIST OF ILLUSTRATIONS

LIST OF TABLES

Chapter 1

INTRODUCTION

1.1 An Evolving View of Comets

Comets can be among the brightest and most visually conspicuous celestial phenomena visible from Earth (e.g., Figure 1.1), sometimes appearing for days to months as luminescent figures in the sky casting shadows and even outshining the Moon, while featuring expansive tails extending for tens of degrees, if not fully across the sky (Kronk 1999, 2003). Unsurprisingly, they have drawn attention from cultures around the world, whether out of fear, superstition, or—more recently—scientific intrigue, with written records of their passage extending well into antiquity.

Their observational accessibility—rivaled only by that of the Sun, Moon, and the five brightest celestial planets—helped jumpstart scientific understanding of Earth's place in the universe during the scientific revolution. Two of the most significant events during this period involve the Great Comets of 1577 and 1680–1681. Tycho

Figure 1.1: An example of a classical comet, C/2020 F3 (NEOWISE)—the brightest seen by the author over the course of producing this thesis—displaying a dust tail several degrees in length, rising over the San Gabriel Mountains on 2020 July 7.

Brahe's meticulous records of the former comet demonstrated through its absence of discernible parallax that comets were in fact celestial bodies moving amongst the planets, a finding referenced by Johannes Kepler as key evidence refuting the then-popular crystalline sphere model of planetary motion (Seargent 2009). Isaac Newton, meanwhile, observed and followed the latter comet personally, later making extensive use of its unusual orbit—which approached the Sun almost directly, then took a hairpin turn to recede the way from which it approached—to support his theories of gravitation (Newton & Chittenden 1850). Edmond Halley likewise famously made use of the extensive historical records by showing in Halley (1705) the comets of 1456, 1531, 1607, and 1682 were the same comet returning every ~76 yr—now named 1P/Halley—demonstrating that comets can persist as recurrent visitors to the inner solar system.

Further observational insight into the true physical nature of comets came with advancements in astronomical instrumentation over the following centuries. François Arago used a polarimeter to find that the light from both the Great Comet of 1819 and 1P/Halley in 1835 were substantially polarized, suggesting that comets were not self-luminous and instead derived their brightness at least in part from sunlight scattered by dust (Kiselev & Rosenbush 2004). The advent of spectroscopy later in the 19th century led quickly to the detection of emission bands (Huggins 1882a) later identified to be produced by the fluorescence of various carbon-bearing molecules in sunlight (Swings 1942). Two comets passing extremely near the Sun in 1882—Comet Wells and the Great September Comet—provided the first detections of more refractory metallic vapors, including sodium (Huggins 1882b), iron, and nickel (Copeland & Lohse 1882), volatilized by intense heating from these particular comets' proximity to the Sun. Photographic imaging also became widespread after those taken by Gill (1882) of the latter comet demonstrated the technology had advanced beyond the sensitivity achieved by visual observers (Seargent 2009).

The comets of the 19th century also provided several examples of their rapid physical evolution. The first was Biela's Comet, a periodic comet discovered in 1772 observed to split in two in 1846 (Kronk 2003). The comet then disappeared after 1852, replaced with an unusually strong series of later in the 19th century seemingly supplied by meteoroids—fragments of the former comet—following the same orbit as the comet (Schimpff 1885).

Another demonstration began with the Great Comet of 1843, which appeared to share a sungrazing orbit—passing within one solar radius above the solar photosphere—

with the Great Comet of 1106. The two were widely presumed identical until the appearance of a comet in 1880 and then the much brighter Great September Comet of 1882, both of which also appeared to share this orbit yet clearly could not be the same comet (Marsden 1967). Following the appearance of the 1880 comet, Kirkwood (1880) suggested that the 1106, 1843, and 1880 comets instead represented a fragmentation family of comet torn apart from tidal stress near the Sun, a hypothesis quickly validated by the widely-observed disruption of the 1882 comet into a string of nuclei rapidly separating to become independent comets (Gill 1883). This event led Kreutz (1888) to develop a detailed model relating the dynamical history of these fragments of the now-named Kreutz sungrazing family.

Whipple (1950) proposed a physical model of a cometary nucleus as a solid conglomerate of rock and ices. Upon being heated by the Sun in the inner solar system, the ices—predominantly water ice—sublimate, lifting dust off the nucleus (Whipple 1951), and perturbing the nucleus ever so slightly from its gravitational trajectory. Subsequent observations have validated this general model, including the direct infrared detection of water vapor sublimated from 1P/Halley's nucleus (Mumma et al. 1986). The Giotto spacecraft's visit to this comet provided the first direct view of a comet nucleus beneath its enshrouding dust, finding the nucleus to be covered in an unexpectedly dark surface reflecting only a few percent of incident light, with sublimation activity confined to only a small fraction of the total surface (Keller et al. 1986). Later visits to other comets by the Deep Space 1 (Buratti et al. 2004), Stardust (Brownlee et al. 2004), Deep Impact/EPOXI (A'Hearn et al. 2005; A'Hearn et al. 2011), and Rosetta (El-Maarry et al. 2015) missions have since reaffirmed—with incremental revisions—this modern view of the physical nature of a comet.

1.2 Cometary Reservoirs

Between the findings of comets disrupting and disappearing over even human timescales, and contemporaneous dynamical analyses demonstrating their orbital instability to gravitational perturbations by the giant planets, it had become clear by the early 20th century that individual comets were not long-lived fixtures in the solar system, and that they must be supplied by one or more unseen reservoir for any to still be observable (Bobrovnikoff 1929). Oort (1950) evaluated a selection of non-periodic comets with near-parabolic trajectories, carefully integrating back their motion to determine their original, pre-perturbed orbits, and showed an unexpectedly high concentration of comets arriving from a spherical shell extending

~50,000–150,000 au from the Sun that could comprise such a reservoir—a structure now called the Oort Cloud.

Numerical modeling suggests an efficient pathway exists for objects within the planetary region of the outer solar system to be scattered outward by the giant planets (Fernandez 1980) into a large disk that is subsequently sphericized into this Oort Cloud by the action of the galactic tide (Hills 1981). A fraction of the objects within the Oort Cloud, however, could also have been captured from the protoplanetary disks of other stars within the star cluster in which the Sun formed (Levison et al. 2010). Oort Cloud objects could be driven toward the inner solar system to become active comets by perturbations from passing stars (Öpik 1932), although subsequent analyses suggest Milky Way galactic tides to be a more efficient perturbation mechanism (Heisler & Tremaine 1986; Morris & Muller 1986).

Many comets, however, also follow smaller orbits with periods on the order of a few years, often extending only slightly past or remaining entirely within the orbit of Jupiter (Levison & Duncan 1997). These Jupiter-family comets tend to orbit near the same plane as do the planets, so are unlikely to have arrived from a distant, spherical Oort Cloud. Edgeworth (1943) and Kuiper (1951) theorized the possibility of a disk of icy planetesimals orbiting just beyond Neptune, now commonly called the Kuiper Belt (or alternatively, Edgeworth–Kuiper Belt), from which objects can be perturbed inward by planets to become comets. While some of these Kuiper Belt objects (KBOs) formed in place within the Kuiper Belt and continue to follow relatively stable orbits (Batygin et al. 2011), others were—much like Oort Cloud objects—scattered into the Kuiper Belt after forming amongst the planets, and this latter, scattered population appears to possess orbits that permit them to be efficiently scattered inward by the outer planets to first become the centaurs of the outer solar system, then later the Jupiter-family comets of the inner solar system (Duncan & Levison 1997).

Large KBOs have been directly observed. In fact, the 1930 discovery of Pluto (Tombaugh 1946), the first and still volumetrically largest known KBO, predates the concept of the Kuiper Belt, although this planetoid's status as a KBO would not become clear until much later when additional, planetary-sized objects in the Kuiper Belt were discovered (Brown et al. 2005). Numerous sub-planetary KBOs have similarly been found, starting with the ~200 km (15760) Albion (1992 QB1; Jewitt & Luu 1993), with more recent surveys now sensitive to objects down to a few tens of kilometers in diameter (Bannister et al. 2016)—comparable in size to

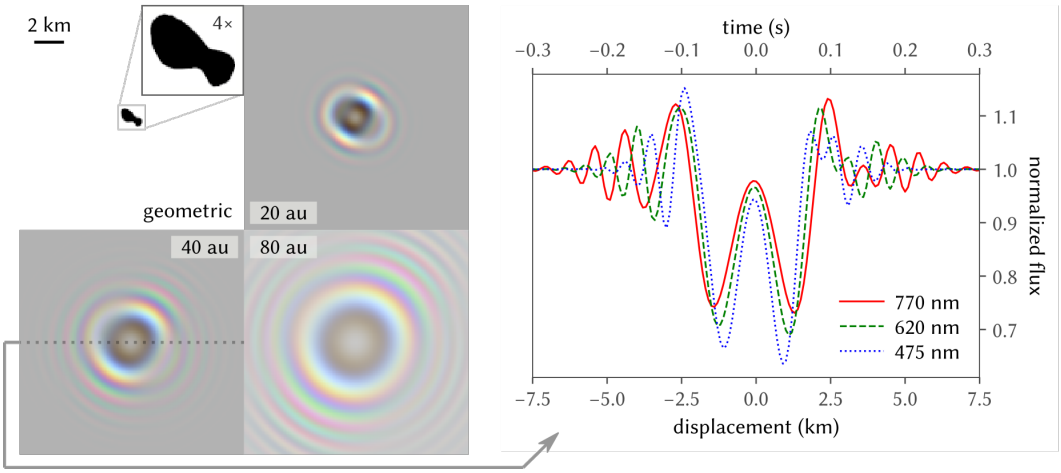

Figure 1.2: *Left*: Numerically simulated diffraction shadow of a 103P/Hartley-shaped comet nucleus (traced from an EPOXI spacecraft image of 103P/Hartley) in the geometric limit (upper left), and with diffraction at 20, 40, and 80 au away simulated for light of 770 nm (red), 620 nm (green), and 475 nm (blue) wavelengths. *Right*: Cross section through the center of the 40 au shadow moving at 25 km s^{-1} with respect to the observer (i.e., typical Kuiper Belt occultation parameters), representing the theoretical wavelength-dependent light curve profile seen by an Earth-based observer along the occultation centerline.

the largest known nuclei of active comets (Lamy et al. 2004).

However, kilometer-scale KBOs comparable in size to typical cometary nuclei remain too faint to be directly surveyed due to the steep, inverse-fourth fading of reflected light with distance from the Sun/Earth (one factor of inverse-square with distance from the Sun for total intercepted sunlight, followed by another factor of inverse-square with distance from the Earth for the fraction of reflected light collected by an Earth-based telescope). One alternative approach is to, instead, monitor for dips in the light curves of background stars when kilometer-scale KBOs pass in front these stars—events called occultations (Bailey 1976). At their distance (~40 au), the shadows of these KBOs—and thus the light curve signatures of their occultations—become substantially altered by diffraction (Roques et al. 1987), which creates wavelength- and distance-dependent fringes (see Figure 1.2).

Several surveys have been conducted to search for these occultations in order characterize the size and—in the case of positive detections—distance distributions of kilometer-scale KBOs (e.g., Roques et al. 2006; Zhang et al. 2013). Detections of such occultations have been claimed by several groups (e.g., Arimatsu et al. 2019; Liu et al. 2015; Schlichting et al. 2012), although the small number of claimed detections available without robust control samples to bound the rate of systematic,

occultation-like artifacts in light curves have raised skepticism as to the veracity of the claimed occultations (e.g., Nir et al. 2023). More sensitive occultations surveys that more robustly constrain the abundance of kilometer-scale KBOs will be required to validate or reject these claims. Chapter 2 presents an attempt at such a survey using the Caltech HIgh-speed Multi-color camERA (CHIMERA, Harding et al. 2016), an instrument on the Palomar Hale Telescope designed to monitor for occultations of stars by capturing the wavelength-dependent signatures of such occultations in high-speed, stellar photometry simultaneously in two different bandpasses.

1.3 Cometary Fading

One curiosity in Oort (1950)'s original results was that there appeared to be too many comets fresh from the Oort Cloud. Planetary perturbations will nearly always either decelerate these dynamically new comets to return again from an orbit clearly detached from the Oort Cloud or accelerate them out of the solar system permanently, with dynamical modeling predicting a far greater fraction of returning comets than actually observed. Later analyses working with larger samples of comets have validated the existence of this discrepancy, finding that a fading parameter is needed to dim or entirely remove a fraction of the comets after every passage around the Sun in order to accurately reproduce the observed distributions of associated comet characteristics (Wiegert & Tremaine 1999).

Comets have been indeed been known to fade/disappear since at least the 19$^{\text{th}}$ century, as discussed previously. Bortle (1991) noted that among Oort Cloud comets (both dynamically new or old), intrinsically fainter comets—i.e., fainter after correcting for differences in comet activity/brightness caused by differences in distance from the Sun and Earth—that approach more closely to the Sun (i.e., with low perihelion distances) appear to exhibit a greater propensity for total disintegration. Observationally debiased orbital statistics of known comets likewise show a deficiency of comets with low perihelion distances relative to dynamical model expectations (Boe et al. 2019). The principal mechanism for this low perihelion fading appears to be rotational instability, whereby torques from asymmetries in sublimation gradually spin up smaller nuclei until centrifugal forces overcome cohesive forces, splitting those nuclei apart into smaller fragments that further spin up and split until no single fragment is sufficiently large to be observed (Jewitt 2022).

However, the fading problem appears to still be present for both large and distant comets with rotation spin-up timescales well in excess of that capable of fully

explaining the observed fading rate (Kaib 2022). In fact, dynamically new comets have been extensively observed to fade over even a single apparition, tending to appear intrinsically much brighter while approaching (i.e., before perihelion) than while subsequently receding from the Sun (i.e., after perihelion, Whipple 1978). These first-time visitors to the inner solar system are, in fact, often already visibly active on approach while still well into the outer solar system (Meech et al. 2017), driven by the sublimation of ices volatile at lower temperatures than water ice, such as carbon monoxide (Yang et al. 2021). Moreover, these comets are sometimes visibly ejecting dust well before before sublimative pressure from even the most volatile of ices should be capable of overcoming typical electrostatic cohesion forces binding the dust grains to each other and the surface (Jewitt et al. 2019). The fresh surfaces of at least some of these inbound, dynamically new comets evidently have properties quite different from that of more thermally evolved cometary surfaces.

Chapter 3 investigates one such dynamically new comet, C/2017 K2 (PANSTARRS), using the Hubble Space Telescope to measure the optical color and polarization of the comet's dust following ejection from the nucleus in search of unusual dust properties or behavior that might be characteristic of the comet's newness. Optical color and polarization are two observable characteristics sensitive to the dust size distribution, structure, and composition (Kolokolova et al. 2004). While they often cannot unambiguously constrain all of these physical properties, they nonetheless serve as useful proxies in isolating spatial variations in these properties and thus probing the evolution of grain properties in the space environment as the dust moves away from the nucleus.

1.4 Hidden in Broad Daylight

Although the Kreutz sungrazing family had been identified by the end of 19$^{\text{th}}$ century, several additional prominent members appeared in the latter half of the 20$^{\text{th}}$ century (Marsden 1967). These comets included the particularly well-observed Comet Ikeya–Seki of 1965 whose spectra within a few solar radii of the Sun showed iron and nickel vapor for the first time since the 1882 Kreutz comet, as well as a host of other metal vapors including calcium, manganese, copper, vanadium, and titanium (Preston 1967) never detected from any other active comet prior or since, despite the advancements in spectroscopic capabilities in the intervening decades.

This lack of follow up is due in large part to the operational challenge of observing fainter comets adjacent to the much brighter Sun in the daytime sky, especially with

the danger that stray, focused sunlight poses to instruments not designed for such observations. However, one instrument designed specifically to observe the sky near the Sun is the Lyot (1933) coronagraph, intended to replicate the effect of a total solar eclipse by the Moon in order to study the faint solar corona directly adjacent to the brilliant disk of the solar photosphere.

Coronagraphs on Earth are ultimately limited by the luminance of the daytime sky—greatly amplified by the extreme forward scattering of sunlight by any fine particulates in the atmosphere near the line of the sight to the Sun—which could only be overcome by moving the coronagraphs above the atmosphere. The advent of long-lived space-borne coronagraphs on the Solwind ("Solar Wind") spacecraft, the SolarMax Mission (SMM), and later, the Solar and Heliospheric Observatory (SOHO) ushered in not only a new scientific era for heliophysics and space weather forecasting—the actual intent for these instruments—but also one for the study of near-Sun comets these instruments were coincidentally well-suited to image (Jones et al. 2018).

Beginning with the first Solwind discovery of a Kreutz comet Michels et al. (1982), these space-borne coronagraphs quickly revealed the Kreutz sungrazing family to be far more extensive than its few ground-observed members, and instead comprised a dense, nearly continuous stream of smaller fragments, each behaving as an independent comet, brightening on approach to the Sun before disintegrating hours before perihelion. Participants of the Sungrazer citizen science project have identified several thousands of these Kreutz comets in images from the SOHO's Large Angle Spectrometric Coronagraph (LASCO) cameras alone (Battams & Knight 2017). Figure 1.3 shows an example of a coronagraphic image by the LASCO C3 camera.

SOHO has also observed many near-Sun comets that do not appear to belong to the Kreutz sungrazing family or to any other known cometary fragmentation family. Several of these objects have short orbital periods of just a few years, and have been observed by SOHO multiple times, including two—322P/SOHO and 323P/SOHO—with perihelion distances of ~0.04–0.05 au that have been since recovered away from the Sun with ordinary, nighttime astronomical telescopes (Hui et al. 2022; Knight et al. 2016). Both of these SOHO comets appear to possess 200–300 m diameter nuclei that exhibit no discernible activity while ~1 au from the Sun, a location where solar heating of water ice on classical comets typically drives obvious dust loss.

These objects are therefore likely depleted of water ice, either due to having lost ice after repeated close encounters with the Sun, or because they had little ice to begin

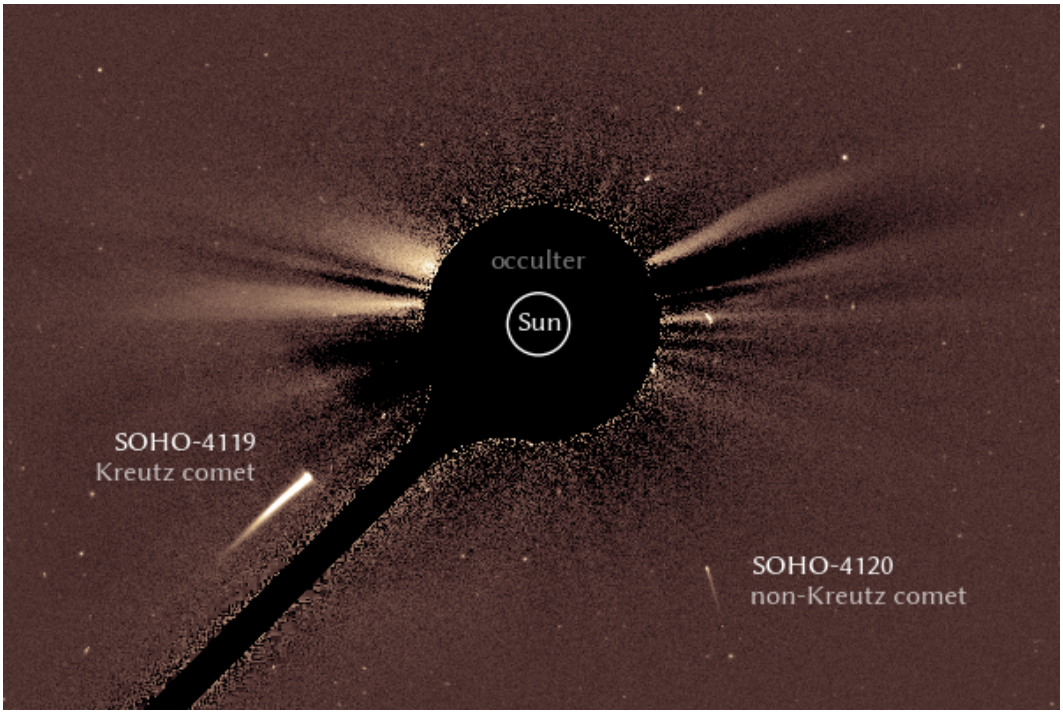

Figure 1.3: Example of imagery from SOHO's LASCO C3 coronagraph on 2021 January 17, showing the instrument's occulter blocking the Sun (size and position indicated by the labeled circle) to reveal the presence of two comets, one a member of the Kreutz family (SOHO-4119) and one not (SOHO-4120).

with if they originated in the inner solar system as ordinary asteroids rather than from the classical cometary reservoirs. Furthermore, both objects appear glow orange in SOHO color imagery from the fluorescence of sodium vapor (Lamy et al. 2013), activity that does not require the sublimation of water ice to produce. Both objects likewise appear to be rotating faster than any known classical cometary nuclei and may already be at their rotational breakup limits (Hui et al. 2022; Knight et al. 2016), providing a mechanism to refresh their surfaces—which would otherwise rapidly become sodium-depleted—for continued activity.

Even initially inactive objects can rotationally accelerate to their breakup limits by torques arising from asymmetries in their absorption of sunlight and in reradiation of thermal energy through the Yarkovsky–O'Keefe–Radzievskii-–Paddack (YORP) effect (Rubincam 2000), which is particularly efficient for such small objects approaching so closely to the Sun. Indeed, debiased orbital statistics show a pronounced deficit in the abundance of asteroids with low perihelion distances relative to dynamical models (Granvik et al. 2016) while simultaneously showing an overabundance of meteoroid streams—potential products of disrupted asteroids—on

such orbits (Ye & Granvik 2019).

Such a disruption mechanism could also be acting on the much larger, ~5 km diameter asteroid (3200) Phaethon, whose current orbit suggests it originated from the asteroid main belt rather than the Oort Cloud or Kuiper Belt (Bottke Jr et al. 2002). It nonetheless appears associated with the Geminids meteoroid stream—the trail of dust presently responsible for the strongest annually recurring meteor shower on Earth—with which the asteroid approximately shares an orbit (Whipple 1983), yet does not appear to exhibit ongoing dust release that could sustain this stream (Ye et al. 2021). The stream itself is likely several thousands of years old (Ryabova 1999), perhaps created in one or a few impulsive events as might be expected for an asteroid spun up past its breakup limit, which Phaethon may still be presently near (Nakano & Hirabayashi 2020).

Phaethon, however, is now known to be not entirely inactive thanks to the twin Solar Terrestrial Relations Observatory (STEREO) spacecraft, whose coronagraph-like Heliospheric Imager 1 (HI1) instruments have repeatedly caught the asteroid sharply brightening and developing a short tail near its 0.14 au perihelion (Hui & Li 2017; Jewitt & Li 2010; Li & Jewitt 2013). These phenomena were previously attributed to Phaethon impulsively ejecting a small amount of comet-like dust each perihelion, but this interpretation overlooked a shift in the HI1 filter bandpass from the published transmission profile following the launch of STEREO that vastly increased the sensitivity to sodium fluorescence emission (Halain 2012). Chapter 4 revisits the nature of Phaethon's perihelion brightening and tail, making use of both new and archival SOHO and STEREO data to show that these phenomena do, in fact, reflect the fluorescence of sodium vapor released by Phaethon, like the activity of 322P, 323P, and many other comets seen by SOHO.

Taxonomically, it remains unclear if objects like Phaethon and 322P/323P with activity not driven by the ice sublimation should appropriately be classified as comets due to a lack of consensus as to whether "comet" should refer to any object showing visible activity (the operational definition adopted by the Minor Planet Center for designating new discoveries), or only to objects physically similar to the classical, icy comets that populate the historical record. The title of this thesis uses "cometoid" as a catch-all term inclusive of both classes of comet-like objects to include the classical comets, active asteroids like Phaethon, as well as the icy planetesimals in Oort Cloud and Kuiper Belt that may become the classical comets in the future, with all of these small bodies populating the solar system connected

through their collective origin in the early solar system.

References

A'Hearn, M. F., Belton, M., Delamere, W., et al. 2005, Sci, 310, 258

Arimatsu, K., Tsumura, K., Usui, F., et al. 2019, NatAs, 3, 301

A'Hearn, M. F., Belton, M. J., Delamere, W. A., et al. 2011, Sci, 332, 1396

Bailey, M. 1976, Natur, 259, 290

Bannister, M. T., Kavelaars, J., Petit, J.-M., et al. 2016, AJ, 152, 70

Battams, K., & Knight, M. M. 2017, RSPTA, 375, 20160257

Batygin, K., Brown, M. E., & Fraser, W. C. 2011, ApJ, 738, 13

Bobrovnikoff, N. 1929, PASP, 41, 98

Boe, B., Jedicke, R., Meech, K. J., et al. 2019, Icar, 333, 252

Bortle, J. E. 1991, ICQ, 13, 89

Bottke Jr, W. F., Morbidelli, A., Jedicke, R., et al. 2002, Icar, 156, 399

Brown, M. E., Trujillo, C. A., & Rabinowitz, D. L. 2005, ApJ, 635, L97

Brownlee, D. E., Horz, F., Newburn, R. L., et al. 2004, Sci, 304, 1764

Buratti, B., Hicks, M., Soderblom, L., et al. 2004, Icar, 167, 16

Copeland, R., & Lohse, J. 1882, Coper, 2, 225

Duncan, M. J., & Levison, H. F. 1997, Sci, 276, 1670

Edgeworth, K. E. 1943, JBAA, 53, 181

El-Maarry, M. R., Thomas, N., Giacomini, L., et al. 2015, A&A, 583, A26

Fernandez, J. A. 1980, Icar, 42, 406

Gill, D. 1882, MNRAS, 43, 53

—. 1883, MNRAS, 43, 319

Granvik, M., Morbidelli, A., Jedicke, R., et al. 2016, Natur, 530, 303

Halain, J.-P. 2012, PhD thesis, Université de Liège

Halley, E. 1705, A Synopsis of the Astronomy of Comets (London: John Senex)

Harding, L. K., Hallinan, G., Milburn, J., et al. 2016, MNRAS, 457, 3036

Heisler, J., & Tremaine, S. 1986, Icar, 65, 13

Hills, J. 1981, AJ, 86, 1730

Huggins, W. 1882a, RSPS, 33, 1

—. 1882b, RSPS, 34, 148

Hui, M.-T., & Li, J. 2017, AJ, 153, 23

Hui, M.-T., Tholen, D. J., Kracht, R., et al. 2022, AJ, 164, 1

Jewitt, D. 2022, AJ, 164, 158

Jewitt, D., Agarwal, J., Hui, M.-T., et al. 2019, AJ, 157, 65

Jewitt, D., & Li, J. 2010, AJ, 140, 1519

Jewitt, D., & Luu, J. 1993, Natur, 362, 730

Jones, G. H., Knight, M. M., Battams, K., et al. 2018, SSRv, 214, 20

Kaib, N. A. 2022, SciA, 8, eabm9130

Keller, H. U., Arpigny, C., Barbieri, C., et al. 1986, Natur, 321, 320

Kirkwood, D. 1880, Obs, 3, 590

Kiselev, N., & Rosenbush, V. 2004, in Photopolarimetry in Remote Sensing, ed. M. M. Gorden Videen, Yaroslav Yatskiv (Dordrecht: Springer), 411–430

Knight, M. M., Fitzsimmons, A., Kelley, M. S., & Snodgrass, C. 2016, ApJL, 823, L6

Kolokolova, L., Hanner, M. S., Levasseur-Regourd, A.-C., Gustafson, B. Å., et al. 2004, in Comets II, ed. M. Festou, H. U. Keller, & H. A. Weaver (Tucson, AZ: Univ. of Arizona Press), 577–604

Kreutz, H. 1888, Untersuchungen über das Cometensystem 1843 I, 1880 I und 1882 II, Vol. 1 (Druck von C. Schaidt, CF Mohr nachfl.)

Kronk, G. W. 1999, Cometography: A Catalog of Comets, Volume 1: Ancient–1799 (London: Cambridge Univ. Press)

—. 2003, Cometography: A Catalog of Comets, Volume 2. 1800–1899 (London: Cambridge Univ. Press)

Kuiper, G. P. 1951, PNAS, 37, 1

Lamy, P., Faury, G., Llebaria, A., et al. 2013, Icar, 226, 1350

Lamy, P. L., Toth, I., Fernández, Y. R., Weaver, H. A., et al. 2004, in Comets II, Vol. 1 (Tucson, AZ: Univ. of Arizona), 223–264

Levison, H. F., & Duncan, M. J. 1997, Icarus, 127, 13

Levison, H. F., Duncan, M. J., Brasser, R., & Kaufmann, D. E. 2010, Sci, 329, 187

Li, J., & Jewitt, D. 2013, AJ, 145, 154

Liu, C.-Y., Doressoundiram, A., Roques, F., et al. 2015, MNRAS, 446, 932

Lyot, B. 1933, JRASC, 27, 265

Marsden, B. G. 1967, AJ, 72, 1170

Meech, K. J., Kleyna, J. T., Hainaut, O., et al. 2017, ApJL, 849, L8

Michels, D., Sheeley Jr, N., Howard, R., & Koomen, M. 1982, Sci, 215, 1097

Morris, D., & Muller, R. 1986, Icar, 65, 1

Mumma, M. J., Weaver, H. A., Larson, H. P., Davis, D. S., & Williams, M. 1986, Sci, 232, 1523

Nakano, R., & Hirabayashi, M. 2020, ApJL, 892, L22

Newton, I., & Chittenden, N. 1850, Newton's Principia: The Mathematical Principles of Natural Philosophy (New York: Geo. P. Putnam)

Nir, G., Ofek, E. O., Polishook, D., Zackay, B., & Ben-Ami, S. 2023, arXiv:2303.12020

Oort, J. 1950, BAN, 11, 91

Öpik, E. 1932, PAAAS, 67, 169

Preston, G. W. 1967, ApJ, 147, 718

Roques, F., Moncuquet, M., & Sicardy, B. 1987, AJ, 93, 1549

Roques, F., Doressoundiram, A., Dhillon, V., et al. 2006, AJ, 132, 819

Rubincam, D. P. 2000, Icar, 148, 2

Ryabova, G. 1999, SoSyR, 33, 224

Schimpff, R. D. 1885, Sci, 6, 519

Schlichting, H. E., Ofek, E. O., Nelan, E. P., et al. 2012, ApJ, 761, 150

Seargent, D. A. 2009, The Greatest Comets in History: Broom Stars and Celestial Scimitars (New York: Springer)

Swings, P. 1942, RvMP, 14, 190

Tombaugh, C. W. 1946, ASPL, 5, 73

Whipple, F. 1978, M&P, 18, 343

Whipple, F. L. 1950, ApJ, 111, 375

—. 1951, ApJ, 113, 464

—. 1983, IAUC, 3881, 1

Wiegert, P., & Tremaine, S. 1999, Icar, 137, 84

Yang, B., Jewitt, D., Zhao, Y., et al. 2021, ApJL, 914, L17

Ye, Q., & Granvik, M. 2019, ApJ, 873, 104

Ye, Q., Knight, M. M., Kelley, M. S., et al. 2021, PSJ, 2, 23

Zhang, Z.-W., Lehner, M., Wang, J.-H., et al. 2013, AJ, 146, 14

Chapter 2

CHIMERA OCCULTATION CONSTRAINTS ON THE ABUNDANCE OF KILOMETER-SCALE KUIPER BELT OBJECTS

Zhang, Q., Hallinan, G. W., Saini, N. S., et al. 2023, AJ, 166, 242, doi: 10.3847/1538-3881/ad03e3

2.1 Introduction

Kuiper Belt objects (KBOs) populate the outer solar system beyond the orbit of Neptune (Jewitt 1999; Jewitt & Luu 1993). These objects provide a record of the evolution of the early solar system (e.g., Kenyon & Bromley 2004; Morbidelli et al. 2003; Schlichting et al. 2013) and supply the transient population of Jupiter-family comets (JFCs) in the inner solar system (e.g., Duncan & Levison 1997). However, while objects larger than several kilometers in diameter can be directly found and observed by their reflected sunlight (e.g., Bernardinelli et al. 2020; Fraser & Kavelaars 2008; Fuentes & Holman 2008; Millis et al. 2002), the presumably more abundant kilometer-scale and smaller KBOs are too faint to be observed in this way with modern survey instrumentation.

The population of these small KBOs can thus currently only be probed indirectly, such as by monitoring for serendipitous occultations of background stars by such objects (Bailey 1976)—events generally lasting less than a second thus requiring high-cadence photometry to reliably detect—and several occultation surveys have been conducted to constrain the number density of small KBOs. Roques et al. (2006) used simultaneous high-speed imaging in g' and i'—thus obtaining two sets of simultaneous and only partially correlated light curves for each star—through the 4.2 m William Herschel Telescope. They reported three candidate events, but with properties inconsistent with those expected for true KBO occultations. Bianco et al. (2009) used single-channel, r' imaging from the 6.5 m MMT Observatory's Megacam and likewise reported no likely KBO occultations. The much deeper Taiwanese–American Occultation Survey (TAOS; Alcock et al. 2003) used a set of four separate 0.5 m telescopes simultaneously observing the same star field, and similarly set only an upper limit on the small KBO abundance (Zhang et al. 2008, 2013).

Another search by Schlichting et al. (2009) and Schlichting et al. (2012) of archival data from the 2.4 m Hubble Space Telescope (HST)'s Fine Guidance Sensors (FGS)—observing from above the atmosphere, thus providing photometry free of atmospheric scintillation effects—found two claimed occultations, while a search through Convection, Rotation and planetary Transits (CoRoT) spacecraft imagery by Liu et al. (2015) yielded another dozen claimed occultations. Additionally, Arimatsu et al. (2019) claimed an occultation detection by their ground-based Organized Autotelescopes for Serendipitous Event Survey (OASES) system of two co-aligned 0.3 m telescopes, although Nir et al. (2023) more recently report a nondetection from a survey with their 0.55 m Weizmann Fast Astronomical Survey Telescope (W-FAST; Nir et al. 2023) in tension with the OASES detection claim.

Curiously, crater counting with New Horizons imagery (Singer et al. 2019) and extrapolations of direct telescopic surveys (Kavelaars et al. 2021) have suggested kilometer-scale KBOs may be depleted to orders of magnitude below the abundances implied by the claimed occultations. The difference suggests that either these studies are sampling a different population within the Kuiper Belt with significantly fewer kilometer-sized objects than that sampled by occultations, they made erroneous assumptions in converting their respective data into KBO number densities, or the claimed occultation detections are actually artifacts missed by the respective statistical analyses. This discrepancy motivates further, more sensitive occultation surveys to validate or reject the earlier claims.

In this paper, we present results from a survey carried out with the Caltech HIspeed Multicolor camERA (CHIMERA; Harding et al. 2016) on the 5.1 m Palomar Hale Telescope over 2015–2017. CHIMERA was specifically designed for this survey, and uses a dichroic and two EMCCD cameras to provide high-speed imaging simultaneously in both a blue channel with a g' filter and a red channel with an i' filter, producing data of a similar nature to, but far more sensitive than, that previously collected by Roques et al. (2006). We discuss the nature of our observations, the photometric reduction process, and the use of occultation templates toward further constraining the rate of occultations by kilometer-scale KBOs and thus their overall abundance.

2.2 Observations

The design of a serendipitous occultation survey generally aims to monitor as many stars for as long as possible within available resource limits to maximize sensitivity.

KBOs are additionally concentrated around a mean plane tilted ∼1°.7 from the ecliptic plane (Brown & Pan 2004), so the KBO occultation rate will be higher for stars near this plane. Additionally, KBOs are at a distance (∼40 au) where effects from both diffraction and the apparent diameters of occulted stars become pronounced for kilometer-scale occulters (Roques et al. 1987, 2006), requiring the use of bright stars with high signal-to-noise (S/N) ratios and angularly small disks, in order to detect occultations by such small and distant objects. In exchange, both size (largely from occultation depth) and distance (largely from occultation duration) can be simultaneously extracted from a single light curve with sufficiently high S/N, whereas nearly geometric occultations by nearer objects constrain only the size.

Balancing these factors, we selected a dense star field centered on the M22 globular cluster at a distant ∼3 kpc (Gaia Collaboration et al. 2023) away just 0°.7 south of the ecliptic and 0°.3 south of the Kuiper Belt mean plane measured by Matheson & Malhotra (2023). While the predominantly old stars tend to be cooler and thus angularly large for their brightness, only a few dozen of the largest stars are angularly larger (Gaia Collaboration et al. 2023) than the optical Fresnel scale (Roques & Moncuquet 2000) of ∼1 km ∼ 0.05 mas at ∼40 au away. The smearing effect of nonzero stellar diameter on the occultation is therefore dwarfed by the diffraction effects for the overwhelming majority of stars in the cluster.

CHIMERA's $5' \times 5'$ field-of-view covers only the core of the cluster but already captures several thousand distinguishable stars in single 30.39 ms exposures through both the blue/g' and red/i' channels, as demonstrated in Figure 2.1. We ran CHIMERA with 2×2 binning at a plate scale of $0''.6$ px^{-1}, which enabled a frame rate of ∼33 Hz (30.39 ms exposure time + 0.67 ms overhead between frames), and successfully observed the M22 field for a total of 63.1 hr spread over 24 nights, as summarized in Table 2.1.

Observations were conducted similarly across all nights, with the telescope pointed at M22 at the start of the sequence and left to sidereally track without closed loop guiding for the duration of the observation period, over which the pointing typically drifts by on the order of $\sim 1'$. Also, most observations were collected at an airmass of ∼2 as limited by the southern declination of M22 and the northern latitude of Palomar Observatory.

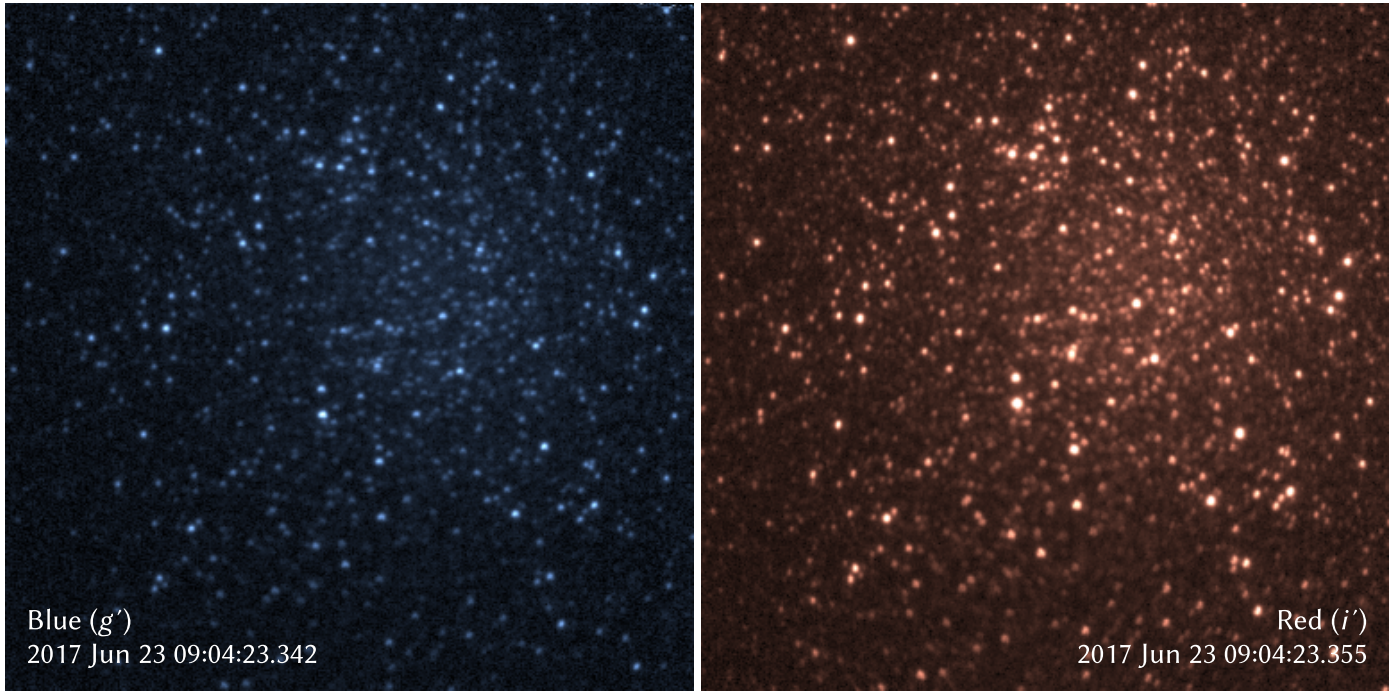

Figure 2.1: Example of nearly simultaneous 30.39 ms exposure frames of M22 through the blue (g'; left) and red (i'; right) channels after bias and flat calibration. The g'/i' images in this and subsequent figures are tinted blue/red for clarity.

Table 2.1: Summary of Observations

Date (UT)	M22 Data (hr)[a]	Seeing (arcsec)[b]
2015 Jul 12	3.4	1.0
2015 Jul 13	3.5	1.1
2015 Jul 14	3.3	1.2
2015 Jul 15	3.5	1.1
2015 Jul 16	4.1	1.0
2015 Aug 14	3.0	1.1
2015 Aug 15	1.7[c]	1.4
2015 Aug 16	3.1	1.4
2015 Aug 17	2.4	1.2
2016 Jul 4	3.3	1.5
2016 Jul 28	0.6[c]	1.3
2016 Jul 29	2.8	1.4
2016 Jul 30	2.7	1.1
2016 Jul 31	2.2	1.0
2016 Aug 1	3.3	1.3
2016 Aug 2	2.8	0.8
2016 Aug 4	1.0[c]	1.2
2017 Jun 23	3.3	1.8
2017 Jun 24	1.2[c]	1.8
2017 Jun 25	2.7	1.8
2017 Jun 26	1.2	1.7
2017 Jul 21	2.3	1.2
2017 Jul 22	3.0	1.5
2017 Jul 23	2.5	1.1
Total	63.1	–

[a]Hours of integration on M22 per night in each of i' and g'.

[b]Nightly average zenith seeing FWHM reported by seeing monitor.

[c]Partially disrupted by clouds.

2.3 Data Reduction

The process of transforming the image cubes of M22 into KBO occultation constraints is divided into two major steps: (1) extracting the light curves of the stars from each frame with a technique specifically adapted to the extremely dense star field of M22's core, and (2) a general approach of matching the processed light curves against templates of light curve patterns expected for true occultations by KBOs to place limits on the occultation rate, and subsequently the KBO number density. These steps are detailed in sections 2.3.1 and 2.3.2, respectively. For our present analysis, we used only the more sensitive red/i' channel data to set occultation rate and thus KBO number density constraints, and reserved the blue/g' data to subsequently evaluate the consistency of the limiting events with the wavelength-dependent light curve patterns expected for true occultations.

2.3.1 Photometry

The survey data set presents a couple of unique challenges to be overcome for accurate photometry:

1. The M22 star field packs many thousands of stars into a single $5' \times 5'$ CHIMERA field of view. While most are indistinguishable from being blended with brighter, adjacent stars or otherwise too faint for CHIMERA to detect KBO occultations of, their collective presence precludes the use of classical aperture photometry methods as any circular aperture or annulus will be contaminated by a numerous neighboring stars.

2. The full data set contains several million individual frames, each of which requires the photometric extraction of several thousand stars. Traditional dense-field photometry methods involving the direct fitting of point spread functions (PSFs) are computationally intensive and cannot be practically applied to the full data set with our available computing resources.

We developed a custom photometry method that combines both the classical aperture photometry and PSF fitting techniques to reliably and efficiently extract dense-field photometry from a fixed field-of-view.

Our data were written in cubes of 1000 frames (~30 s; much longer than the <1 s duration of targeted occultations) each, which we processed largely separately. However, we first selected one of these image cubes from the middle of the observation

sequence of each night to serve as the reference cube for that night. We applied standard bias frame and flat field corrections to all frames of this reference cube, corrected for the slight (∼1%) gain instability in recorded frames by normalizing to the median of all pixels in each frame, then used cross correlation minimization to align and shift all frames to correct telescope tracking and atmospheric tip-tilt effects. We then repeated the process for all image cubes from that night, aligning and shifting them to the pointing of the reference field such that all frames collected on each night are co-aligned.

Next, we astrometrically solved for the center and orientation of the reference field using a third-order polynomial distortion model previously derived by Harding et al. (2016). We then used the astrometric solution to select the 15 brightest stars contained in each field that are isolated >5 px (3″) horizontally and vertically from any other stars less than 2 mag fainter in order to generate an 11×11 px effective point spread function (ePSF, Anderson & King 2000) from the mean stack of each image cube, as well as from each frame individually. From the mean ePSF, we generated a simulated frame with astrometry matching the mean, containing all stars from the catalog within the observed field-of-view, and scaled the simulated star frame jointly with a flat sky background plus a 2D Gaussian distribution representing unresolved stars excluded from the catalog to photometrically fit the mean observed frame.

For astrometry, photometry, the generation of simulated frames, as well as star identification numbering, we used the M22 star catalog by Liu et al. (2015), which provides ∼12,000 total stars within our field-of-view—several times more than the Gaia DR3 catalog, which has poor completeness due to the high star density in the cluster (Gaia Collaboration et al. 2023). This catalog provides Johnson V magnitudes and Strömgren $b - y$ colors, which we converted to SDSS g' and i' magnitudes using the transformations described in Cousins (1987) and Jordi et al. (2006). These transformed magnitudes, however, can have sizable errors due to a combination of stellar properties not captured in the simplistic transformation functions and actual, long-term physical variability in the stars themselves.

Therefore, for each night, we performed a first iteration of light curve extraction on the reference cube alone to measure the mean stellar fluxes through our actual filter bandpasses. For each star in the catalog within the field, we performed the following steps:

1. We determined an optimal aperture for the star using the initial simulated

frame and the signal contribution of the star by starting the nearest pixel to the position of the star and its eight surrounding pixels, then iteratively testing the expected S/N of all adjacent pixels, adding only those pixels that increase the expected S/N into the aperture and repeating until no additional pixels can be added to the aperture to increase the expected S/N.

2. We used the initial simulated frame to estimate the total background flux from sky brightness plus all other resolved and unresolved stars contained within the aperture, taking the flux of the star to be the flux contained within the aperture minus the estimated total background flux.

This procedure produces a set of optimal apertures and mean fluxes for all catalogued stars on the frame. We then considered only the subset of stars whose light curves have S/N > 5 (as measured by the mean flux divided by the standard deviation), corrected the transformed catalog magnitudes of these stars to match their measured mean fluxes, then repeated the photometry process for each of these stars in all image cubes with a new set of simulated frames using the ePSFs of every individual frame. Figure 2.2 illustrates the closeness of the match between an observed frame and its corresponding simulated frame.

The match, however, is still not perfect with clear systematic errors that vary on a frame-to-frame basis, including variations in the true PSF across the frame, as well as temporal variation in the image distortion from atmospheric effects. These errors then translate into artifacts in the measured light curve, which can sometimes appear similar to patterns expected from true occultations. Such events, however, can often be distinguished from occultations by their tendency to simultaneously affect many stars at once, e.g., when a particularly turbulent patch of atmosphere crosses the field, so can in principle be identified by searching for times when a large fraction of light curves all significantly stray from their mean values.

To quantify this source of uncertainty, we took all the light curves from each image cube and first normalized them to a mean of zero and a standard deviation of one, i.e., into a times series of z-scores. Next, we compared these light curve z-scores across all stars at every individual frame/time. When a patch of turbulence (or a similar effect) affects at least a portion of the frame, the ensemble of light curve z-scores from the corresponding frames/times exhibits a much larger spread than the standard normal distribution (since these z-scores of focus are ones normalized to the standard deviations of the individual light curves, and not to that of the ensemble of values

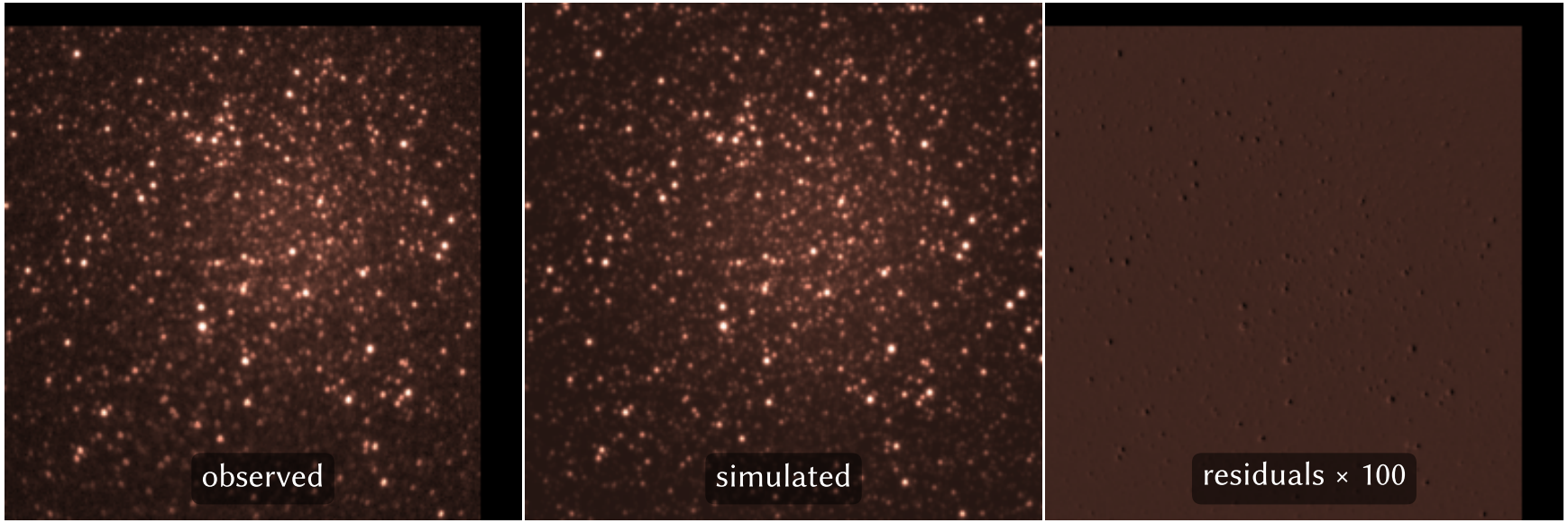

Figure 2.2: Demonstration of simulated frame matching, showing the red channel (i') frame in Figure 2.1 (left), the simulated model frame (center), and the observed minus simulated residual frame (right), with the residuals (on the order of only ∼0.1% of the peak flux) amplified by 100× for visibility. Note that the observed frame has been shifted into alignment with the simulated frame centered on the field of the nightly reference frame, from which the true camera pointing slightly drifts over the course of each night.

across light curves). We originally used the standard deviation of these z-scores directly as the standard error at each frame/time in the normalized light curves. However, we found that in practice, the light curve z-score ensembles often deviate substantially from normal distribution during periods of high turbulence/similar events, and the ordinary standard deviation fails to adequately capture the much larger excursions exhibited a small number of stars/light curves than expected by the normal distribution. These photometrically poor time periods appear to cover only a small fraction of the total observing time, so we chose to simply minimize the contributions of these periods of all light curves at each frame/time to reflect the spread of all normalized light curves at that frame/time.

More specifically, we used the stars with the second highest and lowest z-scores across the ensemble of all light curves at each frame/time. We chose to consider the second highest/lowest values, so the procedure does not downweight a light curve with a deep, real occultation, if one is responsible for the highest/lowest z-score. It would be unlikely for multiple such occultations to occur simultaneously, and consider the second highest/lowest z-scores to reflect only noise. These raw values, however, would not be appropriate to use as the standard errors, because the second highest/lowest values of a large sample drawn from even a normal distribution will be several σ from the mean, e.g., the second highest/lowest values of a normally distributed sample of 1000 items will fall near $\pm 3\sigma$. We then considered the normal distributions whose quantile functions match the second highest/lowest z-scores stars at their respective quantiles (i.e., $1 - 1.5/N_\star$ and $1.5/N_\star$ for the second highest and lowest values out of $N_\star$ light curves, respectively), and used the mean of the standard deviations of these two matched normal distributions as the standard error for the frame/time. Finally, we applied a shift to the nominal flux at each frame/time to set the mean z-score of all light curves at each frame/time to zero, as a final step to reduce the degree of artifacts correlated between multiple light curves.

The resulting, processed light curves still exhibit a great degree of correlated noise, which we have quantified by fitting an exponential decay model to the autocorrelation of every light curve. Across our full data set, light curves exhibit an average, effective correlation length of ~4 frames (~0.1 s), corresponding to a factor of ~2 loss in S/N in time-binned light curves compared to a similar light curve with fully independent (e.g., readout or shot noise limited) points. Figure 2.3 illustrates the distribution of both the raw light curve S/N and the equivalent, correlation-corrected per-frame S/N within our M22 data set, showing that the number of stars in each frame with a

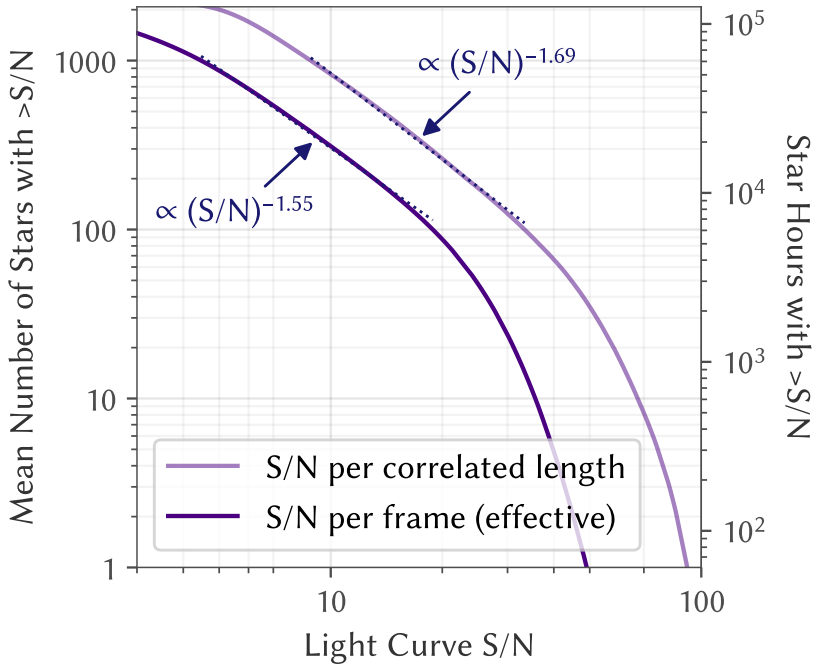

Figure 2.3: Cumulative distribution of stars by effective S/N measured per correlated length of light curve (light blue) and per 30.39 ms exposure frame (dark blue). The distributions roughly follow a truncated power law, with the mean number of stars per frame above a given S/N scaling approximately with $(S/N)^{-1.6}$ at between 100 and 1000 stars.

light curve above a particular S/N roughly follows a power law $\propto (S/N)^{-1.6}$ in the range of 100–1000 stars.

2.3.2 Occultation Search

2.3.2.1 Occultation Templates

Due to their size and distance, occultations by kilometer-scale KBOs are significantly altered by diffraction effects, so are poorly represented by a near-instantaneous total disappearance and re-emergence of the occulted star (Roques et al. 1987). Instead, diffraction effectively sets a minimum radius for the KBOs' shadows that is approximately the Fresnel scale of ∼1 km (Roques & Moncuquet 2000), with the physical sizes of smaller KBOs affecting only the depth rather than the size of the shadow, and also produces a ringing pattern of both positive and negative brightness excursions extending well beyond the shadow core. We used the analytic model of Roques & Moncuquet (2000) for the occultation shadow of KBOs modeled as circular disks, and accounted for smearing of the shadow from nonzero stellar diameters by convolving the analytic model with stellar disks approximated as

circular and uniformly bright.

The light curve of an occultation is a 1D cross section through this 2D diffraction shadow, scaled for the relative speed between the occulter and observer. To generate this cross section of the wavelength-dependent shadow, we performed Monte Carlo sampling of wavelengths over 695–844 nm for i' and 401–550 nm for g', approximated with uniform weighting over those intervals, i.e., neglecting the higher order impact of star color. Our observations of M22 were predominantly made near opposition, where the relative speed of KBOs is predominantly set by Earth's 30 km s^{-1} orbital speed around the Sun, which dwarfs the ~5 km s^{-1} circular orbital speed of KBOs at $r \sim 40$ au from the Sun. Nonetheless, given the simplicity of the correction, we modeled the relative speed for the actual viewing geometry at each epoch, with KBOs treated as moving parallel to the ecliptic in circular, heliocentric orbits.

From this model, we can simulate the light curve signature of occultations with any given KBO heliocentric distance r, diameters D, occultation impact parameter (minimum linear distance of the observer from the shadow center) b, and stellar angular diameter δ. The δ is fixed for each star, which we computed by estimating its effective temperature from its $g' - i'$ color using Fukugita et al. (2011), then crudely approximating its emission as blackbody and treating all stars as being at common distance of 3 kpc, with the understanding that errors in δ of several tens of percent, or even a factor of a few, only minimally affect the actual diffraction shadow as the stellar disk is dwarfed by the angular Fresnel scale for the vast majority of observed stars. The other three parameters—r, D, and b—can take on a wide range of values that will vary between events.

For our survey of occultations by kilometer-scale KBOs, we targeted a cube of parameter space encompassing at least 35 au $< r <$ 50 au (covering most classical KBOs, e.g., Bannister et al. 2018), 0.5 km $< D <$ 2 km, and $b <$ 1.5 km, and set up a grid of occultation templates covering the region against which the observed light curves can be compared. We experimented with various grid densities, evaluating each choice comparing the root-mean-squared (RMS) differences of all adjacent templates on the grid—calculated by subtracting one template from another, squaring the resulting points, and taking the square root of the mean of the result (i.e., the RMS residuals of using templates to fit adjacent templates acting as simulated occultations)—and that of the template with an occultation-free flat line. We settled on the following grid points:

1. r = 35 au, 40 au, 45 au, 50 au
2. D = 0.5 km, 0.6 km, 0.7 km, 0.8 km, 1.0 km, 1.2 km, 1.4 km, 1.7 km, 2.0 km
3. b = 0 km, 0.5 km, 1.0 km, 1.5 km

With this grid, >90% of all pairs of adjacent templates have RMS differences <10% that of the RMS difference of either compared with the occultation-free flat line, in i'. An exact match of an occultation with a template of its actual properties provides the maximum S/N, and corresponds to a template compared to itself, with zero RMS difference. Matching any occultation with a flat line yields a zero S/N match. Both signal (and thus S/N) and RMS difference scale linearly with occultation/template amplitude, so this set of templates generally provides <10% loss of S/N fitting an occultation on a grid point with the neighboring template. We treat each of these templates as representing the centers of their respective bins fully covering the entire spanned region of parameter space, with each bin separated from the next at the midpoint of the respective templates' parameters and endpoint bins treated as symmetric about their central value (e.g., the D = 2.0 km bins cover 1.85–2.15 km), aside from b = 0 km which is treated as covering 0–0.25 km since $b \geq 0$ by definition. We computed all occultation templates out to a radius of 3× the largest Fresnel scale of occultations on the grid, set by the r = 50 au templates, which typically corresponds to an occultation duration of 18 frames ~ 0.5 s in i'.

2.3.2.2 Template Fitting

Demonstrating that an occultation-like signature in an observed light curve actually arises from an occultation rather than atmospheric turbulence artifacts amplified by dense-field photometric errors is a difficult challenge requiring a detailed model accurately capturing not only how those effects typically behave, but also their extreme, low probability tail behavior at the frequency of the targeted occultation rate. Such a model could be obtained, for example, with a dedicated, comparably-sized control data set targeting stars angularly too large to be occulted by kilometer-sized KBOs, or near the ecliptic poles where few KBOs are present. The results of such an undertaking, however, only become useful if the main survey has identified plausible candidate occultations that cannot be ruled out as occultations by other means.

In fact, demonstrating that a light curve does *not* contain a particular occultation signature is a far simpler task that requires only a straightforward statistical test

comparing the observed light curve with a template of that occultation signature, with the null hypothesis that the observed light curve arises from that template plus noise. The corresponding p-value is the conditional probability for that section of light curve to be at least as different from the template as it is given the assumption that an occultation matching the template did actually occur there. Any given real occultation is unlikely to be disrupted by occasional, high-amplitude fluctuations arising from atmospheric or related systematic effects, so we can perform this test using only the typical noise characteristics of the light curve, quantifying the distance between the light curve and template by the Mahalanobis distance ($\mathbf{d}^{-1}\mathbf{C}\mathbf{d}$ for residuals vector $\mathbf{d}$ and covariance matrix $\mathbf{C}$) using the flux uncertainties and autocorrelation measurements previously described in section 2.3.1. We then estimate the expected distribution of this template–light curve distance for real occultations by injecting the template everywhere along the light curve and measuring the resulting distribution of distances.

Figure 4.5 illustrates the full process, starting with the raw light curve of a star from an image cube with uncertainties derived from the light curves of other stars, then passing it through a high-pass filter to remove features longer than the occultation template, and finally sliding the template along the processed curve to compute the template–light curve distance at each point along the light curve. This process quantifies the similarity of the light curve to a template, identifying locations where that similarity (i.e., the template–light curve distance) is comparable to values expected if there were a real occultation with the template's parameters at that position. Real occultations will likewise not match the template exactly due to the presence of noise, so will have a nonzero template–light curve distance distributed by a χ^2-like probability distribution. We quantify this expected distribution by adding ("injecting") the template at each point along the light curve to represent the appearance of a true occultation. We then take the resulting collection of template–light curve (with injected occultation) distances as the probability distribution for the value of the template–light curve distance a real occultation with the parameters of the template would take, if such an occultation were actually present on the light curve. Under this formalism, light curves farther from/more dissimilar to the template than all except a false negative fraction β of injected occultations can be ruled out as containing a real occultation to a confidence level of $1 - \beta$.

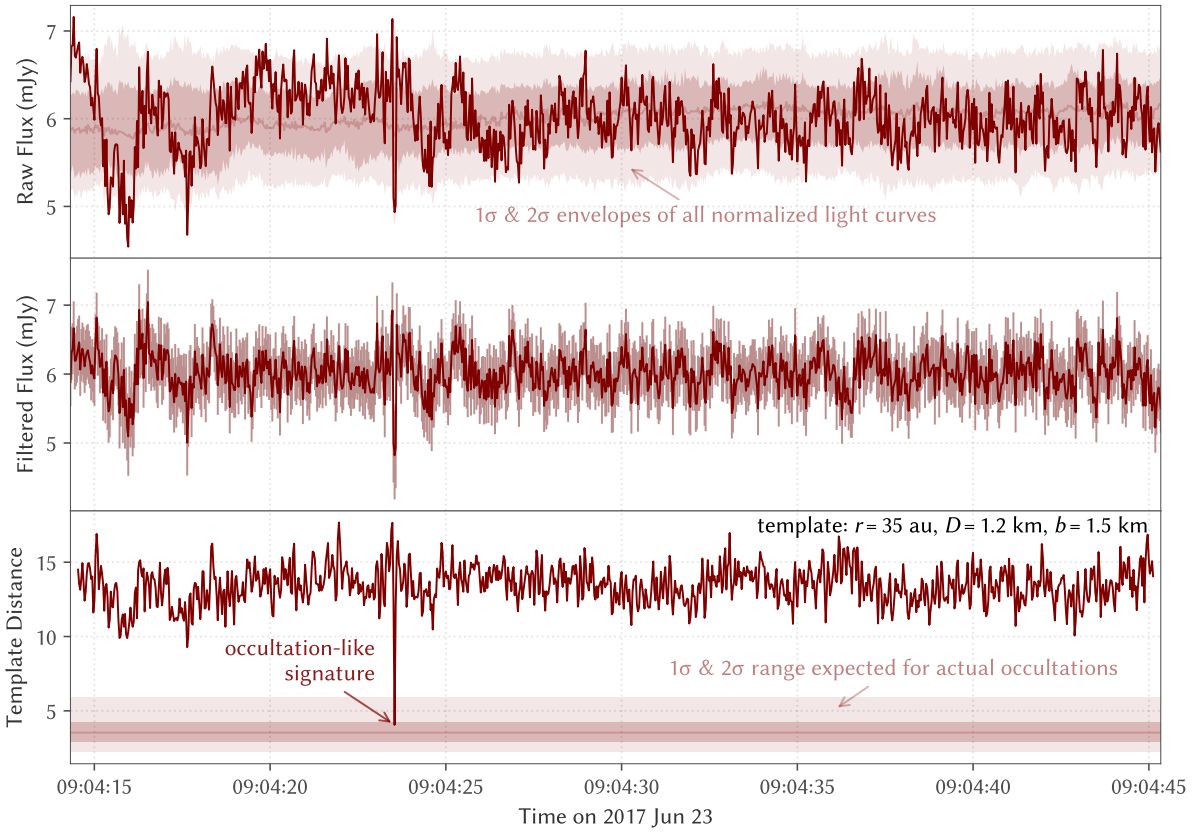

Figure 2.4: Example of an i' light curve being fit with a template. *Top:* The raw light curve for star 2636 compared with the envelope of light curves of other stars in the field normalized to the same brightness and S/N. *Middle:* The same light curve passed through a high-pass filter, corrected with the mean offset of the other normalized light curves with error bars set by the spread of those light curves. *Bottom:* The goodness of fit of an occultation template sliding along the light curve, as measured by the Mahalanobis distance between the observed light curve and template at each point based on the autocorrelation measured from the light curve. The 1σ and 2σ ranges of the template distance expected from simulated, injected occultation events are indicated here. An inset of the labeled occultation-like signature in this light curve alongside the associated template is shown in the upper row of Figure 2.7.

2.3.2.3 Constraining the Occultation Rate

We use the template–light curve distance to define another S/N: that of the light curve with respect to each template. Here, we consider the "signal" to be the difference in the mean template–light curve distance of the actual light curve (i.e., the expected value of the template–light curve distance in the absence of an occultation) and that with an occultation injected (i.e., the expected value of the template–light curve distance if an occultation matching the template were present). Meanwhile, we consider the "noise" of this template S/N to be the quadrature sum of the standard deviation of the template–light curve distance along the actual light curve (i.e., the data curve in the bottom panel of Figure 4.5), and that of the light curve with injected occultations (i.e., the spread of the probability distribution of the template–light curve distance of a real occultation, corresponding to the indicated range expected for actual occultations in the bottom panel of Figure 4.5). Then, for each template or set of templates spanning the range of occultation parameters of interest, we constrain the overall occultation rate by sorting all the light curves by their template S/N, counting the number of star hours of light curves from which occultations can be rejected starting from highest to lowest S/N until reaching a light curve our selected threshold is unable to reject as containing an occultation, and assuming the occultations follow Poisson statistics, with the final rate corrected for the permitted β.

Under this method, the choice of a β threshold significantly affects the overall survey sensitivity. Enforcing a very low β ensures with high confidence that light curves with no template–light curve distances meeting the threshold do not contain any occultations with the template's parameters, but is only capable of ruling out occultations from high S/N light curves, limiting search depth. In contrast, permitting a higher β will expand the number of usefully searchable light curves at the cost of allowing that fraction of real occultations to slip through, which requires a larger correction factor $(1 - \beta)^{-1}$ to the occultation rate limit that likewise harms sensitivity.

Figure 2.5 illustrates the balance between these two factors in selecting a threshold that allows a large number of stars/light curves to be used without losing too many of the true occultations present within those light-curves. In other words, we aim to maximize the effective number of stars of usable stars hours of light curve—the number of star hours of light curves with a high S/N beyond the threshold contributing to the constraint, corrected for the chosen β. Assuming the number of stars

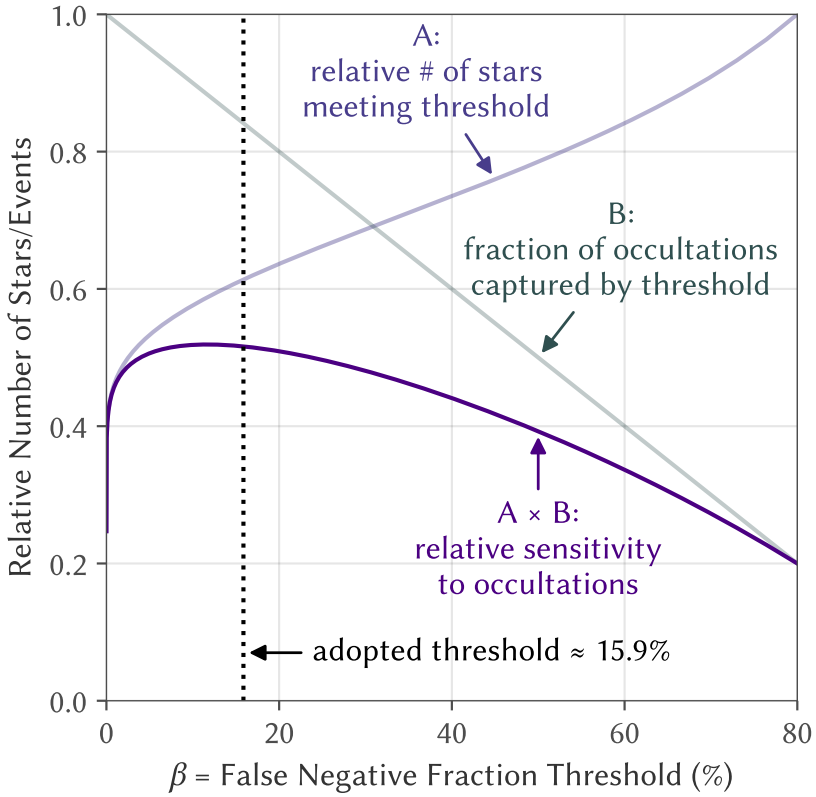

Figure 2.5: Comparison of the estimated number of included stars vs. fraction of included occultations for a range of false negative fraction thresholds β, showing an optimum in relative sensitivity (the product of the two quantities) near the chosen ~15.9% (i.e., 1σ level of the normal distribution).

above a given S/N scales as $(\mathrm{S/N})^{-1.6}$, as previously estimated in section 2.3.1, we estimate an optimal sensitivity near $\beta \sim 5$–20%, with only a few percent difference over this range. We opted for a value of ~15.9% at the $+1\sigma$ limit of template–light curve distance for true occultations. With this selection, any light curve in which an occultation cannot be rejected by this relative weak threshold should qualitatively appear to be well-fit to the template, and the limiting light curves setting the occultation rate limits conveniently become the well-fit occultation candidates with the highest S/N for further evaluation in section 2.4.

2.3.2.4 Occultation Rate to KBO Sky Density

In order to convert the constraint on occultation rate into one on the actual sky density of KBOs, we consider the scanned area of sky corresponding to the high S/N light curves in which occultations can be rejected, which is computed from the relative speed v_i of a KBO at geocentric distance d_i (approximately equal to

heliocentric distance r_i), a template impact parameter bin width Δb_i, and duration Δt_i of the light curve segment with the i^{th} highest template S/N satisfying the β threshold as

$$\Omega = \sum_i \frac{v_i \times \Delta b_i \times \Delta t_i}{d_i} \tag{2.1}$$

where we have treated scans of the same star/light curve by templates of different b equivalently to separate stars, since each additional range of b for which an occultation can be rejected also rules out the presence of a corresponding KBO in an additional parallel, band of sky.

If the limiting event—the highest template S/N light curve segment in which an occultation cannot be rejected—is considered a true occultation, then the sky density Λ of KBOs with the parameters of the searched templates is nominally $\langle\Lambda\rangle = \Omega^{-1}$, since the area of sky searched before encountering the first occultation follows a probability distribution $\Lambda \exp(-\Lambda\Omega)$ under this Poisson process. Likewise, the Λ that places Ω^{-1} at the 95$^{\text{th}}$ percentile of this probability distribution, equal to the 95% confidence upper limit on the true Λ, is $\Lambda_{95} \approx 3\Omega^{-1}$, which we adopt as a robust constraint irrespective of whether the corresponding limiting event is a true occultation.

2.4 Survey Results

2.4.1 Constraints on KBO Sky Density

We computed the cumulative 95% confidence upper limits on sky density for all KBOs larger than various D within various r, and plotted the resulting set of upper limit curves in Figure 2.6. Note that we have little sensitivity to occultations by KBOs larger than the $D \sim 1.8$–2.2 km covered by the 2 km template bin, the contribution of these larger KBOs to the cumulative sky densities is negligible if the size distribution follows a power law $N(>D) \propto D^{-s} \equiv D^{1-q}$ (i.e., cumulative power index s and differential index q) extending to the sky density of KBOs observed by direct telescopic surveys. We corrected our limits assuming a break at $D = 90$ km with $\Lambda(>90\text{ km}) = 5.4$ deg^{-2} as measured by Fraser & Kavelaars (2008), but found that any $\Lambda(>90\text{ km}) \lesssim 10^6$ km^{-2} negligibly affects the results, so our upper limits remain effectively independent of any realistic size distribution model.

Our derived 95% confidence upper limit of $\Lambda(>1\text{ km}) < \Lambda_{95}(>1\text{ km}) \sim 10^7$ deg^{-2} is comparable to the corresponding upper limits set by TAOS (Zhang et al. 2013) and

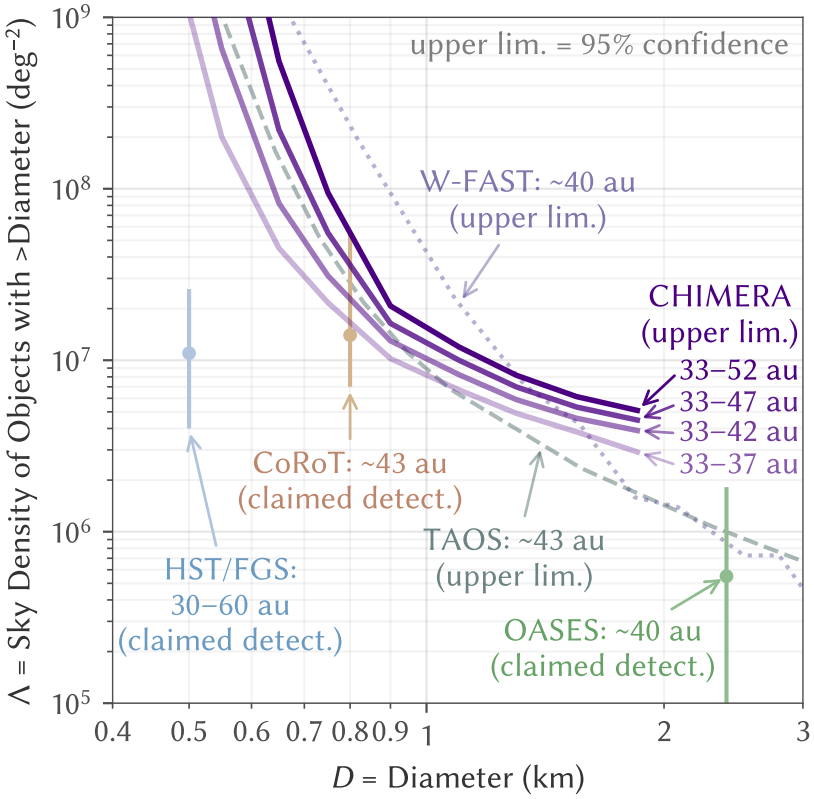

Figure 2.6: The 95% confidence upper limits for the ecliptic sky density of kilometer-scale KBOs larger than the plotted diameters, compared with earlier limits set by TAOS (Zhang et al. 2013) and W-FAST (Nir et al. 2023), as well as the claimed detections from HST/FGS (Schlichting et al. 2012), CoRoT (Liu et al. 2015), and OASES (Arimatsu et al. 2019). The labeled distances indicate the approximate range of KBO distances covered by each survey/upper limit curve.

W-FAST (Nir et al. 2023), as well as the density implied by the claimed detections by CoRoT (Liu et al. 2015). We did not search for occultations as large as the claimed detection by OASES (Arimatsu et al. 2019), although our power law extension to $\Lambda(>90\text{ km}) = 5.4\text{ deg}^{-2}$ of Fraser & Kavelaars (2008) yields a 95% upper limit on the differential index of $q \equiv s + 1 < 4.3$ for the full range of $r = 33$–52 au spanned by our template bins. The claimed detections by HST/FGS (Schlichting et al. 2012) primarily constrain the sky density of KBOs around $D = 0.5$ km which create occultations with insufficient S/N to be detected for most of our light curves, so we do not have a comparable constraint at that size.

We caution, however, that although we have placed all of these constraints together on the same plot for reference, the precise numbers may not be directly comparable. In addition to being derived through different methods with different standards for

interpretation of results, the various surveys also differ in the definition of sky density being measured, with most targeting KBOs around $r = 40$ au or 43 au, often without specifying the actual sensitivity range. Occultations appear fairly similar over the relatively narrow range of considered r, although our results do show slightly weaker constraints when searching for occultations over a wider range out to larger r from a couple of effects:

1. Searching a larger region of parameter space provides more opportunity for noise to create occultation-like signatures. For example, a noisy light curve might coincidentally match an $r = 45$ au template sufficiently well for the corresponding occultation to not be rejected while differing sufficiently from all other templates for those occultations to be rejected, which weakens the 33–47 au and 33–52 au upper limits without affecting the 33–37 au and 33–42 au limits.

2. More distant KBOs create shallower, longer duration occultations that more easily blend in with the strongly correlated, atmospheric noise, so they require light curves to have higher S/N to reject than do occultations by nearer KBOs.

The surveys also target stars over different ranges of ecliptic/Kuiper Belt mean plane latitude, where the actual sky density of KBOs may vary. Our M22 dataset contains only light curves from stars only $0.^{\circ}3$ from the Kuiper Belt mean plane. OASES (Arimatsu et al. 2019) similarly monitored a single field of stars within 2° of the ecliptic. TAOS (Zhang et al. 2013) used a sample of stars 90% within 6° of the ecliptic, while W-FAST (Nir et al. 2023) derived their limit from a sample of stars with 95% within 4° of the ecliptic. The CoRoT (Liu et al. 2015) and HST/FGS (Schlichting et al. 2012) surveys used stars spread as far as several tens of degrees from the ecliptic, and corrected their constraints to ecliptic sky densities based on modeled inclination distributions of kilometer-scale KBOs. Given the uncertain model-dependence of such corrections and differences in methodology across the studies, we have not attempted to correct any of these other reported constraints to match our results, which we instead simply consider to provide a related but separate upper limit.

2.4.2 Limiting Events

We now look more closely at a few of the occultation-like signatures that set the upper limits on occultation rate in order to investigate their viability as occultations

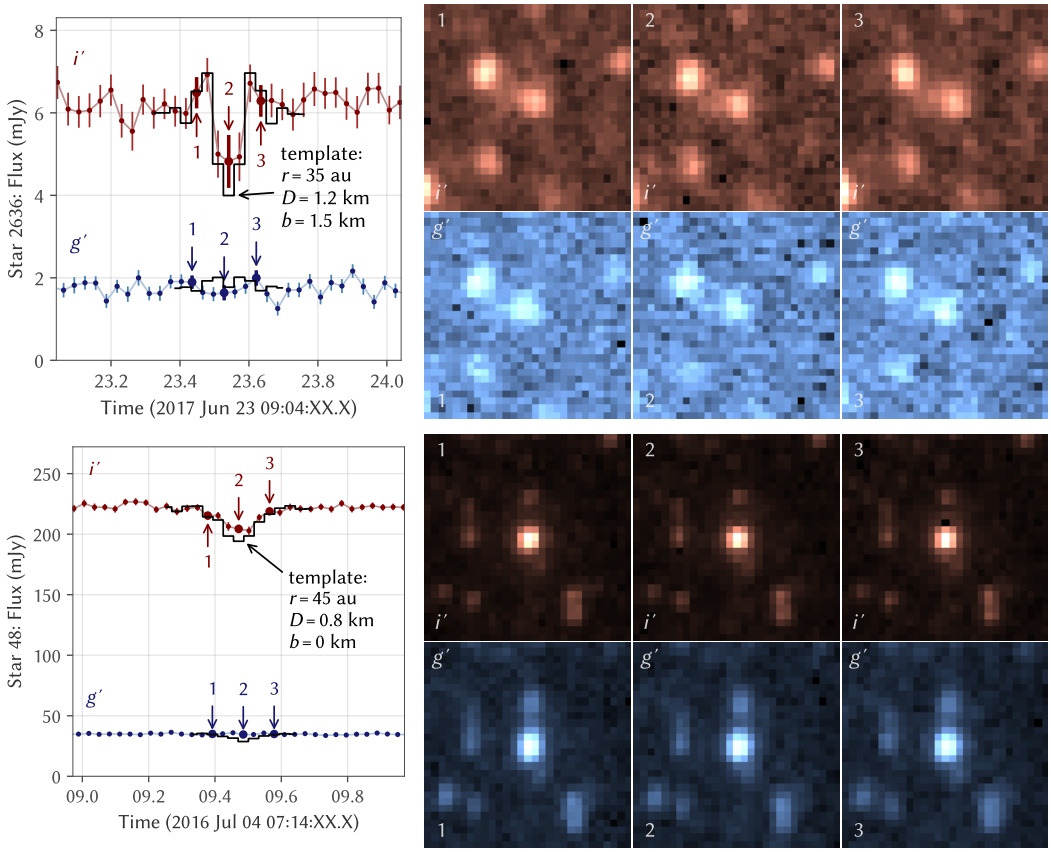

Figure 2.7: Two examples of limiting events showing occultation-like signatures in i' light curves, setting the upper limits on the total 33–52 au KBO sky density for $D > 0.9$ km (upper row) and $D > 0.65$ km (lower row) shown in Figure 2.6. The left column shows the searched i' and simultaneously observed g' light curves for each star with the corresponding templates in black, while the bolded points indicate the corresponding i' and g' inset frames centered on the respective stars shown to the right (1 px = 0″.6). Templates are well-matched to the actually fitted i' light curves as expected, but are not as well-matched to the simultaneous g' light curves, while the star-centered insets do not obviously show changes in the brightness of those stars (although we caution even real fluctuations with similar ∼10–20% amplitude may be only marginally discernible visually), suggesting these events in the i' light curve likely represent artifacts of dense-field photometry rather than true occultations.

and the potential for future improvement of these limits. Figure 2.7 presents two examples of such events setting the $D > 0.9$ km and $D > 0.65$ km upper limits, showing both their fitted red/i' and simultaneous blue/g' light curves, along with the corresponding templates they matched to, and insets centered on the respective stars for a few key frames around each event.

For all of these examples, the red/i' light curve signatures closely resemble the corresponding templates, thus validating the efficacy of our template matching

approach which identified these as red/i' light curves sections with the highest S/N for which these particular occultations cannot be rejected. Note, however, that these templates are not actually the best fit templates to these light curves; lower amplitude occultations actually match these light curves with lower residuals, but give lower template S/N, so they do not provide as limiting a constraint as these worse-fitting but higher S/N templates representing occultations that would still produce a light curve with a comparable or worse fit to the template $\beta \sim 15.9\%$ of the time.

Additionally, the simultaneous blue/g' light curves, which were not template-matched in our current analysis (thus serving as a partially independent source of validation), do not appear as well-matched as the red/i' light curves to their corresponding templates. The star-centered insets also do not reveal any clear dimming corresponding to the dips in the light curves, and instead show slight changes in the PSF around those times. These factors suggest that the occultation-like signatures in the light curves are likely artifacts arising from dense-field photometry errors rather than true variations in the brightness of those stars, so we conclude our limiting events are highly unlikely to be true occultations.

From this qualitative analysis, one potential future improvement to sensitivity could come from jointly fitting occultation templates against both the red/i' and the blue/g' light curves (instead of just red/i', as in our current analysis) to generate a combined template–light curve distance using all of the data. However, the red color of most stars in M22 along with the worse atmospheric turbulence and instrumental image quality in the blue/g' channel led most of the blue/g' light curves to be significantly lower in S/N than the red/i' counterparts. Given also the noticeable correlation between the light curves from the two channels, this effort may only minimally improve our limits with the existing M22 dataset.

The quality of the photometry leaves more clear room for improvement, with the light curves of most stars having S/N well below both the shot noise and atmospheric scintillation limit. About 5,000 stars in the M22 field should have shot noise-limited S/N > 10—far above the typical ~800 light curves with S/N (per correlated length) > 10 indicated in Figure 2.5. Meanwhile, atmospheric scintillation alone should affect stars of all brightness similarly, indicating it contributes noise only at 1–2% of the total flux, given the S/N of the brightest stars. Improving the photometry to these theoretical limits would vastly improve our sensitivity, especially to the smallest, $D < 1$ km KBOs whose occultations can only be distinguished in very high S/N light curves.

The extremely high star density in our M22 field, however, presents a serious challenge for any significant photometry improvements, which will also likely be very computationally expensive. Some improvement to our upper limit may be feasible by reprocessing only the light curves with limiting events and other occultation-like signatures of similar S/N using proper PSF fitting methods, where the improved photometry could potentially reject those features as being from occultations. Due to the spatial variation in PSF across the field, such methods aiming to improve upon our existing photometry must be able to derive a PSF entirely from a dense field without any isolated stars much brighter than surrounding stars, as the few such stars present in this field (used in our method to compute our per-frame ePSFs) are largely distributed toward the outer edge where the PSF may significantly differ from that in the dense core of the cluster. Any future, follow up survey following our strategy may benefit from a lower density field, which circumvents such complications by allowing large photometric apertures insensitive to small changes in the PSF, which we anticipate can more than offset the reduced star count.

2.5 Conclusions

In summary, we used the CHIMERA instrument on the Palomar Hale Telescope to observe stars near the core of the M22 globular cluster for a cumulative ~63 hr over 24 nights to monitor for serendipitous occultations by kilometer-scale KBOs of those stars. We developed and used a modified aperture photometry technique to efficiently extract light curves from the dense star field, then compared the processed light curves against templates of light curve signatures from occultations by kilometer-scale KBOs to set upper limits on the sky density of such KBOs. Finally, we presented a couple of examples of limiting events—the highest S/N light curves from which we cannot exclude an occultation—which appear to likely represent artifacts arising from our imperfect dense-field photometry procedure rather than actual occultations.

The 95% confidence upper limits on kilometer-scale KBO abundance set by our nondetections are comparable in magnitude to those set by several other recent occultation surveys, at $\lesssim 10^7$ deg^{-2} of KBOs >1 km in diameter. This limit, however, remains insufficiently constraining for comparison with several of the claimed occultations, which will require at least another order-of-magnitude improvement in sensitivity to robustly validate or reject. Future surveys following a similar strategy may find such an improvement in observing efficiency by targeting lower density star fields with well-separated stars that permit high quality aperture photometry,

avoiding the dense-field photometry artifacts that limited the S/N of our light curves to well below theoretical scintillation and shot noise limits. Such improvements, together with the addition of a high latitude control data set constraining the baseline noise, may eventually permit constraints on not only the number density but also orbital distribution of these kilometer-sized KBOs once a sample of true occultations can be definitively isolated.

References

Alcock, C., Dave, R., Giammarco, J., et al. 2003, EM&P, 92, 459

Anderson, J., & King, I. R. 2000, PASP, 112, 1360

Arimatsu, K., Tsumura, K., Usui, F., et al. 2019, NatAs, 3, 301

Bailey, M. 1976, Natur, 259, 290

Bannister, M. T., Gladman, B. J., Kavelaars, J., et al. 2018, ApJS, 236, 18

Bernardinelli, P. H., Bernstein, G. M., Sako, M., et al. 2020, ApJS, 247, 32

Bianco, F. B., Protopapas, P., McLeod, B. A., et al. 2009, AJ, 138, 568

Brown, M. E., & Pan, M. 2004, AJ, 127, 2418

Cousins, A. 1987, MNASSA, 46, 144

Duncan, M. J., & Levison, H. F. 1997, Sci, 276, 1670

Fraser, W. C., & Kavelaars, J. 2008, AJ, 137, 72

Fuentes, C. I., & Holman, M. J. 2008, AJ, 136, 83

Fukugita, M., Yasuda, N., Doi, M., Gunn, J. E., & York, D. G. 2011, AJ, 141, 47

Gaia Collaboration, Vallenari, A., Brown, A., et al. 2023, A&A, 674, A1

Harding, L. K., Hallinan, G., Milburn, J., et al. 2016, MNRAS, 457, 3036

Jewitt, D. 1999, AREPS, 27, 287

Jewitt, D., & Luu, J. 1993, Natur, 362, 730

Jordi, K., Grebel, E. K., & Ammon, K. 2006, A&A, 460, 339

Kavelaars, J., Petit, J.-M., Gladman, B., et al. 2021, ApJL, 920, L28

Kenyon, S. J., & Bromley, B. C. 2004, AJ, 128, 1916

Liu, C.-Y., Doressoundiram, A., Roques, F., et al. 2015, MNRAS, 446, 932

Matheson, I., & Malhotra, R. 2023, AJ, 165, 241

Millis, R., Buie, M., Wasserman, L., et al. 2002, AJ, 123, 2083

Morbidelli, A., Brown, M., & Levison, H. 2003, EM&P, 92, 1

Nir, G., Ofek, E. O., Polishook, D., Zackay, B., & Ben-Ami, S. 2023, MNRAS, 526, 43

Roques, F., & Moncuquet, M. 2000, Icar, 147, 530

Roques, F., Moncuquet, M., & Sicardy, B. 1987, AJ, 93, 1549

Roques, F., Doressoundiram, A., Dhillon, V., et al. 2006, AJ, 132, 819

Schlichting, H., Ofek, E., Wenz, M., et al. 2009, Natur, 462, 895

Schlichting, H. E., Fuentes, C. I., & Trilling, D. E. 2013, AJ, 146, 36

Schlichting, H. E., Ofek, E. O., Nelan, E. P., et al. 2012, ApJ, 761, 150

Singer, K., McKinnon, W., Gladman, B., et al. 2019, Sci, 363, 955

Zhang, Z.-W., Bianco, F., Lehner, M., et al. 2008, ApJL, 685, L157

Zhang, Z.-W., Lehner, M., Wang, J.-H., et al. 2013, AJ, 146, 14

Chapter 3

DUST EVOLUTION IN THE COMA OF DISTANT, INBOUND COMET C/2017 K2 (PANSTARRS)

Zhang, Q., Kolokolova, L., Ye, Q., & Vissapragada, S. 2022, PSJ, 3, 135, doi: 10.3847/PSJ/ac6d58

3.1 Introduction

C/2017 K2 (PANSTARRS) is an Oort cloud comet discovered by the Pan-STARRS survey (Kaiser et al. 2002) in 2017 May while inbound at a heliocentric distance $r = 16.1$ au from the Sun, over five years before its upcoming perihelion in the inner solar system at $r = 1.8$ au in 2022 December (Williams 2017). The comet was later identified in archival imagery that traced its activity back to 2013 May at a then-unprecedented $r = 23.8$ au (Hui et al. 2017), while modeling of its continued coma evolution has since traced its production of large, millimeter-sized dust grains to $r \sim 35$ au (Jewitt et al. 2021). Such activity well into the outer solar system is too distant for sunlight to effectively drive water ice sublimation on the nucleus—the principal mechanism behind most observed cometary activity in the inner solar system (Whipple 1951)—and suggests the presence of a more volatile substance like carbon monoxide (CO) ice that can sublimate efficiently at much lower temperatures (Meech et al. 2017). Submillimeter observations later confirmed the presence of CO in the coma (Yang et al. 2021).

C/2017 K2 may furthermore be considered dynamically new. Królikowska & Dybczyński (2018) performed dynamical simulations showing that C/2017 K2 has likely never previously entered the inner solar system ($r \lesssim 5$ au) where substantial water ice activity on the nucleus can take place, as it will on its current apparition. Photometric analyses have suggested that dynamically new comets tend to behave differently from returning comets and often exhibit more asymmetric light curves that are substantially brighter before than after perihelion (e.g., A'Hearn et al. 1995; Meech 1989). Such differences in photometric behavior may arise from underlying changes in nucleus and coma properties effected by thermal processing in the inner solar system. C/2017 K2's high brightness while still in the outer solar system makes it a particularly compelling target to evaluate the effects of solar heating on the properties of a relatively fresh comet.

Observations of the color and polarization of scattered sunlight probe spatial heterogeneity of dust within the coma. Both characteristics are sensitive to grain size and absorbance, while polarization is also sensitive to shape and structure (e.g., Hoban et al. 1989; Kolokolova et al. 2004). Previous color imaging of distant comets have revealed the presence of a wide range of structures including reddened jets as well as both red and blue halos (e.g., Ivanova et al. 2019; Korsun et al. 2010; Li et al. 2013).

Polarization varies strongly as a function of phase angle α. Distant comets like C/2017 K2 well beyond the orbit of Earth are geometrically constrained to low $\alpha \lesssim 20°$, where light backscattered by dust grains with a typical aggregate structure can undergo multiple scatterings within the grain. While singly scattered light is polarized perpendicular to the scattering plane—conventionally defined as positive polarization—low order multiple scattered light is polarized in the direction parallel to the scattering plane—defined as negative polarization (Clarke 1974). Negative polarization is typically strongest near $\alpha \sim 10°$ for cometary aggregates, and polarimetry at these α have previously revealed strongly polarized jets and halos. Such structures represent variations in grain structure and absorbance that affect the degree of multiple scattering within those grains (Levasseur-Regourd et al. 2015).

In the following sections, we present high spatial resolution color imagery and polarimetry by the Hubble Space Telescope (HST) of the inner coma of C/2017 K2 to probe spatial variations in dust properties, and subsequently the evolution of dust grains after ejection into the coma space environment. We also discuss follow up near-infrared imaging results by the Palomar Hale Telescope in the context of our model.

3.2 Observations

We observed C/2017 K2 at two epochs, the first with HST on 2021 March 19–20 to collect optical photometry and polarimetry, and the second from Palomar on 2021 May 18 to collect near-infrared photometry. These observations are summarized in Table 3.1.

3.2.1 Hubble Space Telescope (HST)

We used HST's Advanced Camera for Surveys/Wide Field Channel (ACS/WFC) to obtain color and polarization maps of C/2017 K2 over two consecutive spacecraft orbits on 2021 March 19–20 while the comet was at a heliocentric distance r = 6.82 au and geocentric distance Δ = 6.85 au under the HST observing program

Table 3.1: Observations of C/2017 K2

Date/Time (UT)	r (au)[a]	Δ (au)[b]	α (°)[c]	Instrument	Filter(s)	Exposures
2021 Mar 19 21:44–Mar 20 00:01	6.82	6.85	8.35	HST ACS/WFC	F475W + CLEAR2L	204 s + 203 s
					F775W + CLEAR2L	2×160 s
					F775W + POL0V	2×500 s
					F775W + POL60V	2×500 s
					F775W + POL120V	2×500 s
2021 May 18 10:50–12:03	6.34	5.95	8.70	Palomar/WIRC	J	19×60 s
					H	44×20 s
					K_s	25×5 s

[a]Heliocentric distance.

[b]Geocentric distance.

[c]Phase angle.

GO 16214. The $\alpha = 8\overset{\circ}{.}35$ at this epoch is near the $\alpha \sim 10^\circ$ at which negative polarization is typically strongest.

Across the two orbits, we collected a total of ten frames: two unpolarized frames through each of the F475W (comparable to SDSS g') and F775W (SDSS i') filters (i.e., paired with CLEAR2L in the second filter wheel), and two frames through F775W paired with each of the POL0V, POL60V, and POL120V linear polarizers. We arranged exposures symmetrically, with F775W/POL0V → F775W/POL60V → F775W/POL120V → F775W/CLEAR2L → F475W/CLEAR2L for the first orbit, and in the reverse order for the second orbit.

We processed the raw frames through a non-standard approach adapted to mitigate artifacts in our data that is detailed in Appendix 3.5.1. This procedure produced five combined frames, one for each filter combination, cleaned of bad pixels and reprojected onto a common, distortion-free, rectilinear pixel grid covering the coma centered on the observed position of the nucleus.

As discussed in the appendix, we found this observed nucleus position to be offset in the sunward direction by a large $\sim 0''.6$ from the JPL ephemeris position. This offset is far beyond the stated error ellipse, indicating that formal uncertainties for orbital parameters greatly underestimate the true uncertainties, most likely due to uncorrected tailward bias in the ground-based astrometry. The offset is readily corrected and has little impact on our present analysis, but has implications for future dynamical analyses of this comet which may be highly unreliable if such systematic offsets in the astrometry are not considered.

Next, we computed the F475W–F775W color over the coma in the form of the spectral reflectance slope

$$S = \frac{I_{\mathrm{F775W}}/\odot_{\mathrm{F775W}} - I_{\mathrm{F475W}}/\odot_{\mathrm{F475W}}}{I_{\mathrm{F775W}}/\odot_{\mathrm{F775W}} + I_{\mathrm{F475W}}/\odot_{\mathrm{F475W}}} \times \frac{2}{\lambda_{\mathrm{F775W}} - \lambda_{\mathrm{F475W}}} \tag{3.1}$$

where I_{F475W} and I_{F775W} are the absolute fluxes from the standard photometric calibration of the combined F475W/CLEAR2L and F775W/CLEAR2L frames, $\lambda_{\mathrm{F475W}} \approx 475$ nm and $\lambda_{\mathrm{F775W}} \approx 769$ nm are the corresponding pivot wavelengths associated with that calibration, and $\odot_{\mathrm{F475W}}$ and $\odot_{\mathrm{F775W}}$ are the corresponding solar fluxes derived from Willmer (2018).

Similarly, we computed Stokes I, Q, and U and subsequently the polarization degree P and orientation θ_P by combining the frames following the standard procedure outlined in the ACS Data Handbook[1], which corrects for instrumental polarization and imperfect rejection of cross-polarized light by the polarizers (Biretta 2004). Uncertainties arising the presently unmeasured HST roll dependence of the absolute polarimetric calibration are stated to ±1% in P and ±10° in θ_P, but do not impact the relative spatial variations in polarization measured in images.

The plane of polarization for light scattered by randomly oriented particles must remain invariant under reflection across the scattering plane, which constrains the polarization to be perpendicular or parallel to the scattering plane. That plane for scattered sunlight projects to a line that is aligned with the sunward direction $\theta_\odot = 94\overset{\circ}{.}9$, so the observed orientation of such light will be perpendicular or parallel to this direction. As introduced earlier, comet dust grains can be polarized at either angle, with polarization in the perpendicular direction conventionally regarded as positive and polarization in the parallel direction as negative. We define a single, signed parameter $-P\cos(2(\theta_P - \theta_\odot))$ that is the polarization referenced to the perpendicular direction (i.e., equal to $+P$ when $\theta_P - \theta_\odot = 90°$ and $-P$ when $\theta_P - \theta_\odot = 0°$) which we refer to in this text simply as the polarization, as distinguished from P which we refer to as the polarization degree.

3.2.2 Palomar Hale Telescope

We obtained near-infrared J, H, and K_s photometry of C/2017 K2 with the Wide-field Infrared Camera (WIRC) at Palomar on 2021 May 18, 60 d after the HST epoch. Imaging was concentrated in J and H, with cumulative usable integration times of 1140 and 880 s, respectively, but we also collected an additional usable 125 s of exposures in K_s. All science frames were dark and flat-field corrected with matching dark frames and dome flats taken at the end of the night. Exposures through each filter were dithered in five-point pattern comprised of a north-aligned square of four dither positions 8′ on each side, with a fifth position in the center. We astrometrically and photometrically solved each frame with field stars from the Gaia EDR3 (Gaia Collaboration et al. 2021, 2016) and 2MASS (Skrutskie et al. 2006) catalogs, respectively, before aligning all frames on the position of the comet.

To mitigate the impacts of background star trails in the final stacked frames, we measured the PSF FWHM from the reference stars and mask all pixels within 1

[1] `https://hst-docs.stsci.edu/acsdhb`

FWHM of all 2MASS stars within each frame. We iteratively clipped pixels of $>3\sigma$ within each set of aligned frames to capture the remaining stars, and masked these pixels plus all other pixels within 1 FWHM. Finally, we took the mean of the unmasked pixels for each of the J, H, and K_s frames to produce the three final, combined frames from which we measured the associated $J-H$, $H-K_s$, and $J-K_s$ colors.

3.3 Results

3.3.1 Optical Color and Polarization

Figure 3.1 shows the color and polarization in the coma of C/2017 K2 measured by our 2021 March 19–20 HST observations. The dust appears redder than solar color with negative polarization present, indicating substantial optical contributions throughout the coma by micron-sized or larger (i.e., non-Rayleigh scattering) grains bearing optically red materials and with aggregate structures, although other grains may also be present. No features larger than ~1,000 km with $\gtrsim$2% per 100 nm color and $\gtrsim$3% polarization contrast from the surrounding coma appear within $\rho \sim$ 10,000 km of the nucleus. Smaller features can be attributed to artifacts from the expected slight misalignment errors and differences in PSF between frames (Hines et al. 2013). A jet-like fan of dust relatively brighter than the surrounding coma is apparent extending south of the nucleus, similar to features previously reported in HST imagery (Jewitt et al. 2021). Its color and polarization, however, are not distinguishable from those of its surroundings.

At larger scales of several 10,000 km, the nucleus of C/2017 K2 appears to be surrounded by a nearly symmetric region of dust that is both bluer and less negatively polarized compared to dust farther out, as evident in the radial profiles of color and polarization in Figure 3.2. The F475W–F775W slope reddens from ~4.5% per 100 nm within $\rho \sim$ 10,000 km to ~7% per 100 nm by $\rho \sim$ 50,000 km, where the latter is near the middle of the (8.3 ± 3.5)% per 100 nm 2σ range of comet dust (Solontoi et al. 2012). Polarization, meanwhile, strengthens from about −2% to −3.5% over the same $\rho \sim$ 10,000–50,000 km. These lengths scales correspond to dust ages $\tau \sim$ 15–75 d for the predominant millimeter-sized grains leaving nucleus at $v_d \sim 8$ m s^{-1}, and to $\tau \sim$ 1–4 d for any micron-sized grains moving with the gas outflow at $v_d \sim 100$ m s^{-1} (Jewitt et al. 2021).

The concurrent reddening and strengthening in negative polarization indicates a temporal evolution of grain properties following ejection from the nucleus. These

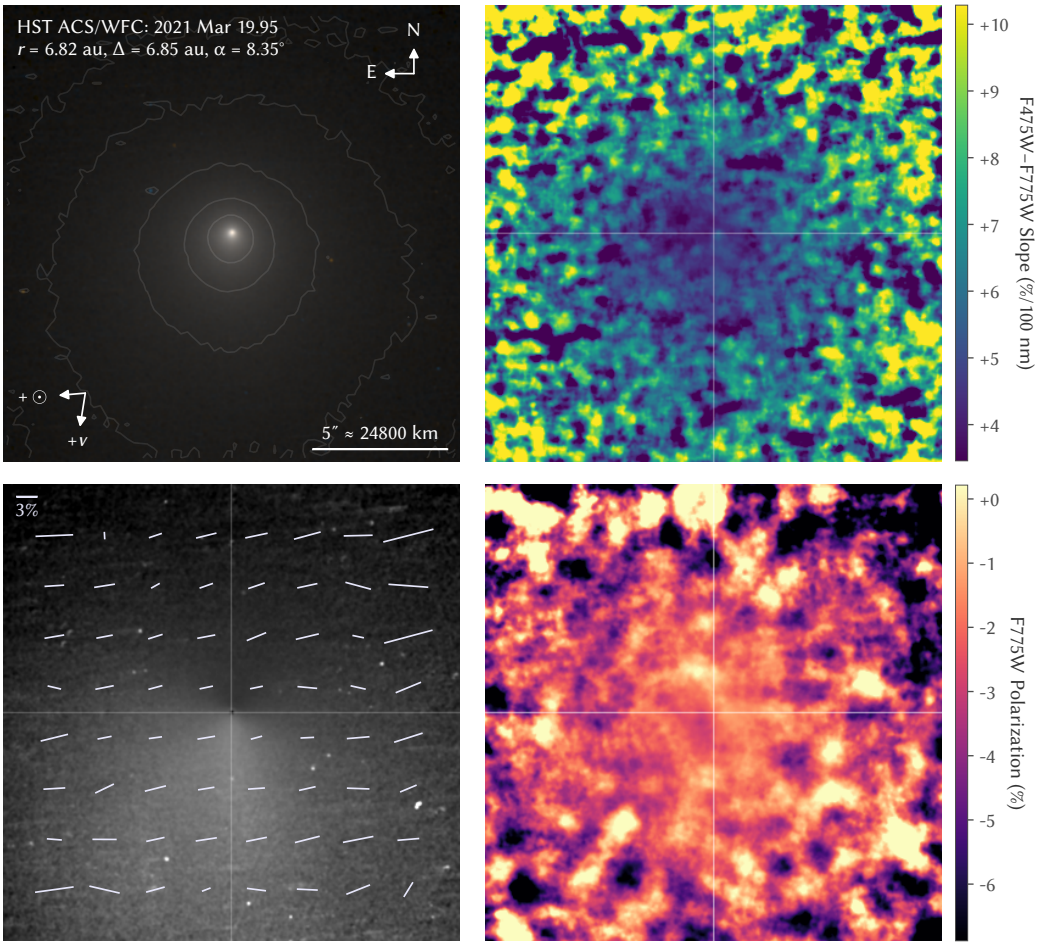

Figure 3.1: HST ACS/WFC color imaging and polarimetry of C/2017 K2. *Upper left:* Composite of non-polarized F475W (g') and F775W (i') frames, overlaid with a selection of isophots. The compasses indicate north (N), east (E), as well as the sunward (+⊙) and heliocentric velocity (+v) directions. *Upper right:* F475W–F775W color map of the same region, with values labeled as reflectance slopes relative to solar color, median smoothed to 0″.5 ~ 2,500 km resolution for display clarity. The color map shows a relatively bluer region surrounding the nucleus. *Lower left:* F775W intensity divided by a $1/\rho$ model, overlaid with markers indicating the direction and degree of polarization. The scale bar to the upper left indicates the length of a marker representing 3% polarization degree. *Lower right:* F775W polarization map, smoothed to 1″ ~ 5,000 km resolution, showing a region of relatively weaker negative polarization surrounding the nucleus. All panels are displayed at the same scale and orientation.

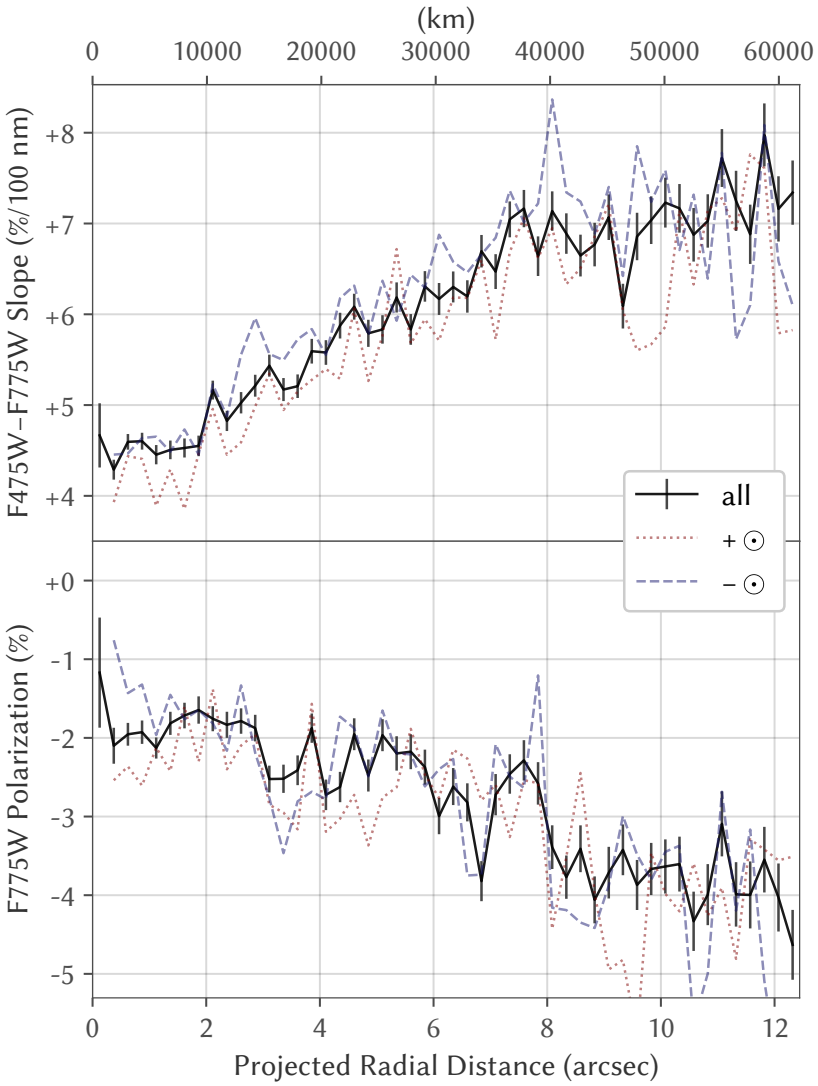

Figure 3.2: Radial profiles of F475W–F775W reflectance slope (top) and F775W polarization (bottom), showing a trend of reddening and strengthened negative polarization outward from the nucleus. The solid black curves with error bars indicate values measured from full, 360° annuli, while the dotted red (labeled +⊙) and dashed blue (−⊙) curves show values measured from 90° annular segments centered on the sunward and antisunward directions, respectively.

trends could arise from changes in grain composition and structure, such a loss of an ice layer from a redder, more absorbing underlying grain. Alternatively, they could arise from changes in the size distribution, such as the destruction of short-lived, micron-sized grains which generally exhibit both a bluer color and more positive polarization at low α (Kolokolova et al. 2004).

3.3.2 Radial Intensity Profiles

In addition to their effects on color and polarization, changes to grain composition, structure, and size distribution can also affect the scattering cross section. In particular, we would like to quantify changes in the cross section of dust after ejection from the nucleus. We can extract this information from the radial intensity profile, as grains are radially sorted from the nucleus by age, albeit with a size dependence.

Stable dust grains ejected from the nucleus at a steady rate in the absence of external forces will form a coma with a $1/\rho$ radial intensity profile (Gehrz & Ney 1992). To evaluate deviations from steady-state, we divided the observed profiles by the $1/\rho$ profile and normalized the result to match the equivalent $Af\rho$ (A'Hearn et al. 1984) for a $1/\rho$ intensity profile tangent to each ρ. These annular $Af\rho$ values are proportional to the scattering cross section per unit interval of ρ. Deviations from a flat annular $Af\rho$ (i.e., a $1/\rho$ profile) can arise when (1) the dust production rate has changed since the grains in the coma were ejected from the nucleus, (2) solar radiation pressure drives grains from the coma into the tail, and (3) the individual grains break down or otherwise change scattering cross section as they drift away from the nucleus. To isolate (3), we modeled the profile expected from (1) and (2) alone with a Monte Carlo simulation following the approach described in Ye et al. (2016, § 2.2).

For this simulation, we used a nucleus radius of 6 km, a differential dust size distribution $\propto a_d^{-3.5}$ for millimeter-sized grains of a_d = 0.1–10 mm, a dust bulk density of ρ_d = 500 kg m^{-3}, and a dust production rate $\propto r^{-2}$ starting at r = 35 au. These parameters are consistent with those estimated by Jewitt et al. (2019, 2021) from the morphology of the outer coma and tail. We then computed the sky-plane brightness of the coma at the epoch of the HST observation, and convolved it with the ACS/WFC F775W PSF produced by Tiny Tim (Krist et al. 2011) for comparison with the observed profiles. Finally, we repeated the simulation for a coma of only micron-sized (a_d = 1 μm) grains for comparison.

Figure 3.3 shows that the radial intensity profile modeled for a coma containing only the stable, millimeter-sized dust grains found by Jewitt et al. (2021) is much steeper than $1/\rho$ as a result of the slowness of those grains: the dust at several times 10,000 km from the nucleus were ejected several months prior to the observation, since when the dust production rate has substantially risen. Moreover, this profile steepens toward the nucleus, as the rate at which the dust production rises is itself rising as the comet approaches the Sun. Stable millimeter-sized grains therefore appear inconsistent with the nearly $1/\rho$ profile actually observed within $\rho \sim$ 10,000 km that steepens away from the nucleus. Removal of an ice layer from otherwise stable millimeter-sized grains can likewise only darken the grains and thus steepen the intensity profile, so appears inconsistent with the observed profile. Additionally, Jewitt et al. (2019, 2021) found that the innermost portion of the coma has maintained a consistent $1/\rho$ profile in HST WFC3/UVIS F350LP imagery since 2017, indicating that the shallowness of the profile is unlikely a result of short-term dust production fluctuations.

One possible explanation for the unusual profile of the inner coma is the fragmentation of millimeter-sized grains at $\rho <$ 10,000 km, which would increase the scattering cross section of the dust outward from the nucleus to produce a shallower-than-modeled intensity profile over those distances. Such a profile, however, would not necessarily match the observed $1/\rho$ except by sheer coincidence. Moreover, fragmentation tends to distort the coma isophots into teardrop shapes by concentrating dust into an antisunward beam due to the increased susceptibility of the smaller, fragmented grains to radiation pressure (Combi 1994). No such features are apparent in Figure 3.1, with the sunward side of the coma instead appearing similar to or slightly brighter than the antisunward side at the several 10,000 km scale.

On the other hand, an inner coma optically dominated by micron-sized grains would naturally produce a nearly steady-state $1/\rho$ profile there: in contrast to the millimeter-sized grains at $\rho \sim$ 10,000 km ejected weeks earlier when the comet was substantially farther from the Sun and thus dust production rate was substantially lower, the much faster-moving micron-sized grains at the same ρ were only about a day old, ejected when the dust production rate was little different from that at the observation time. Destruction of those micron-sized grains past $\rho \sim$ 10,000 km is necessary to then steepen the profile beyond $1/\rho$ and eventually beyond the stable millimeter-sized dust profile into the outer coma, as observed. As this process is also consistent with the concurrent color and polarization trends, we consider the

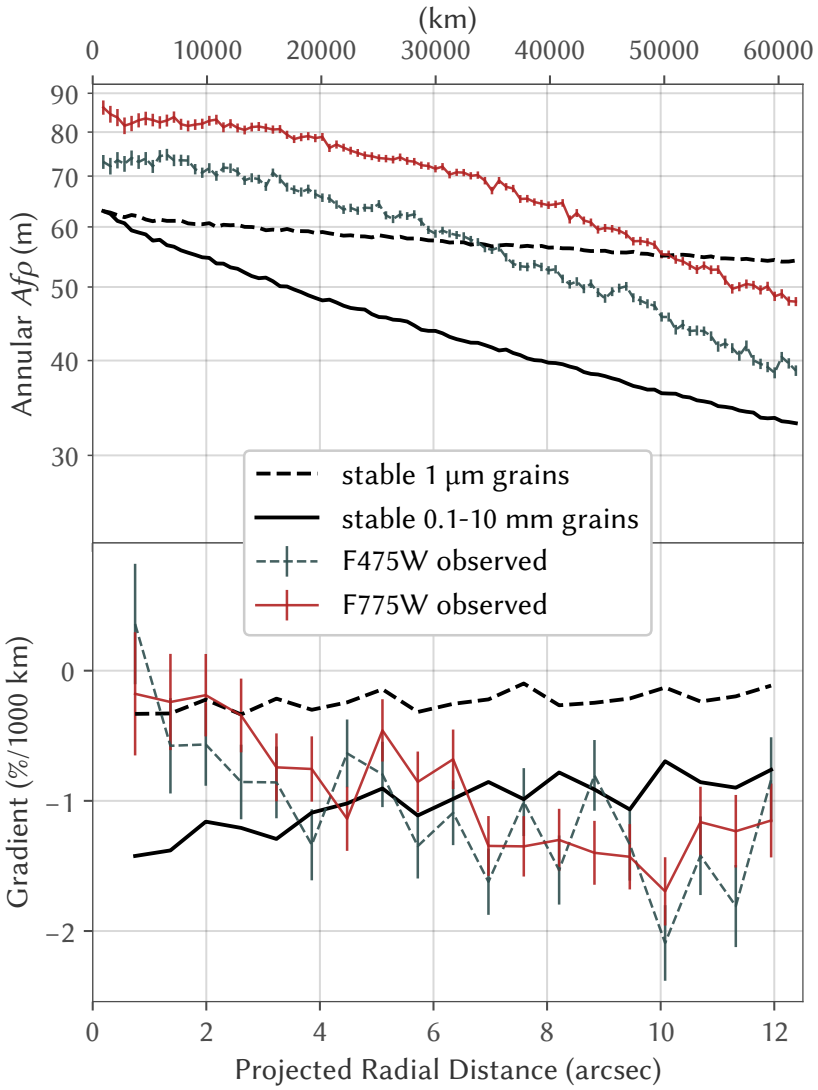

Figure 3.3: The $1/\rho$-equivalent $Af\rho$ of annuli (top)—proportional to the intensity divided by a $1/\rho$ profile—and their radial gradient (bottom). Both observed profiles (red and blue curves) are nearly $1/\rho$ (~0%/1000 km gradient) within $\rho \sim 10{,}000$ km, which is shallower than expected by Monte Carlo simulations (black curves; arbitrarily scaled) of only stable, millimeter-sized grains (solid), as found in the outer coma and tail. Faster, micron-sized grains (dashed) produce a shallower profile consistent with the observed profiles within $\rho \sim 10{,}000$ km.

presence and destruction of micron-sized grains in the inner coma to be the most likely explanation for the observed intensity profile.

3.3.3 Tail Morphology

Refractory remnants of the short-lived, micron-sized grains can theoretically be constrained in the tail by their motion under solar radiation pressure. While similarly distant comets have previously been seen producing such stable micron-sized dust grains (Hui et al. 2019), monitoring of C/2017 K2 has not found any evidence for $a_d \ll 0.1$ mm grains in the tail (Hui et al. 2017; Jewitt et al. 2019, 2021).

A tail morphology analysis of our wide field Palomar/WIRC J and H composite image in Figure 3.4 shows a continued lack of micron-sized grains surviving into the tail. Under the model of Finson & Probstein (1968), dust grains ejected from the nucleus at rest distribute into a grid of two properties: (1) the time since the grain was released, τ, and (2) a parameter β, defined as the ratio of force of solar radiation pressure acting on the grain to that of solar gravitation, which is related to the size of the grain. For typical low albedo grains of $\rho_d \sim 500$ kg m^{-3}, the effective grain radius a_d is roughly related to β by $a_d \sim 1\ \mu\text{m}/\beta$ for $a_d \gtrsim 1$ um with a maximum $\beta \sim 1$ for $a_d \sim 0.1$–$1\ \mu$m (Kimura 2017).

We overlaid the composite image with curves indicating the positions of such zero velocity grains of several representative β (syndynes) and τ (synchrones), where dust released during the HST observations have $\tau = 60$ d. The actual nonzero ejection velocity spreads the dust over a wide area surrounding the labeled curves, and requires a numerical model to properly invert. Even visual inspection, however, shows the brightness along the $\beta = 1$ syndyne beyond the coma to be indistinguishable from that of the background, with only the previously characterized $\beta \lesssim 0.01$ grains evident in the tail. We place a bound of $\gtrsim$24 mag arcsec^{-2} in J on the surface brightness of $\beta \sim 1$ dust at $\tau \sim 60$ d, equivalent to $\lesssim$20% of the dust cross section production actually observed by HST. Evidently, little of the scattering cross section from the micron-sized grains remains into the tail.

3.3.4 Water Ice Sublimation

Water ice serves as an appealing candidate to comprise the observed short-lived grains, being an abundant cometary volatile that leaves no optical remnant after sublimation. Pure water ice grains are highly reflective and can survive for thousands of years at $r > 5$ au, so such ice grains must necessarily be darkened by a highly absorbing contaminant to explain the observations. In fact, light scattering models

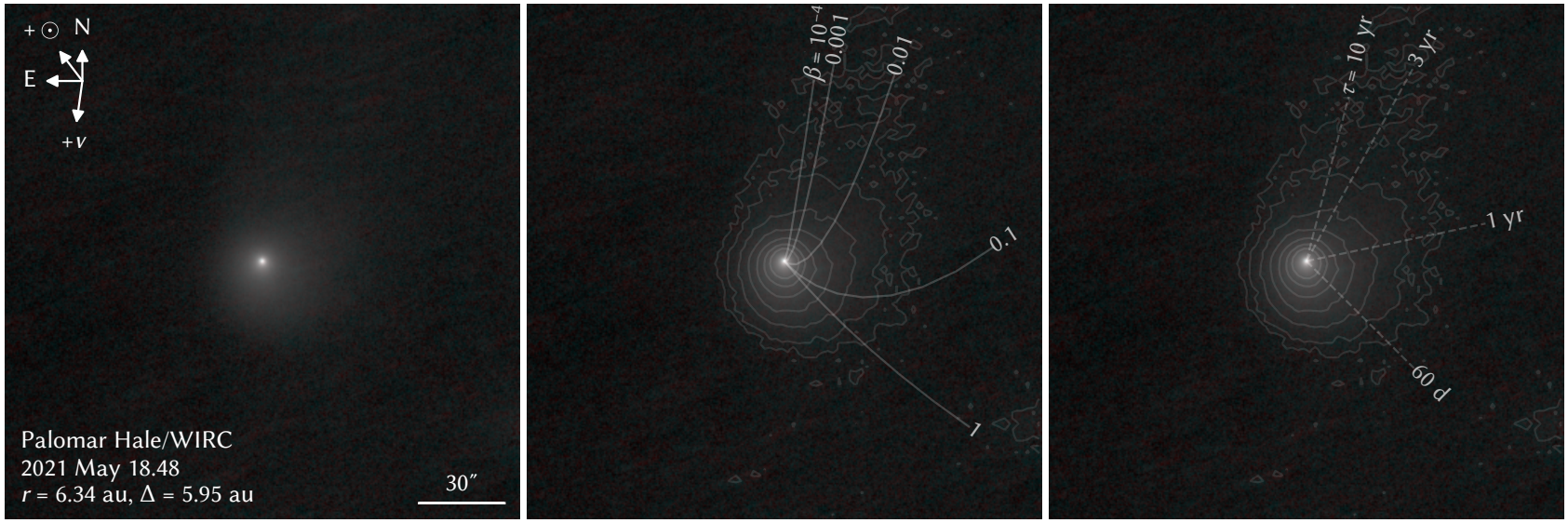

Figure 3.4: Composite of J and H frames by Palomar/WIRC. Representative syndynes and synchrones are drawn over the same image and a selection of isophots in the middle and right panels, respectively, and show the prominent northward tail to be predominantly comprised of large $\beta \lesssim 0.01$ ($a_d \gtrsim 0.1$ mm) grains produced years earlier.

show that even a few percent carbon by volume can darken the ice grains to near zero albedo and thus dramatically lower their lifetime (Beer et al. 2006).

Small, carbonaceous grains radiate inefficiently at wavelengths over than ∼10 times their radii, so can readily exceed the isothermal blackbody temperature in the outer solar system (Hanner et al. 1998). At the $r \sim 7$ au of the HST observation, $a_d \sim 1$ μm carbonaceous grains equilibrate at $T_d \sim 150$ K. At this temperature, water ice has a vapor pressure of a few millipascals, which is sufficient to sublimate the water ice from the $a_d \sim 1$ μm grains over timescales on the order of a day (Hansen & McCord 2004). The observed color, polarization, and intensity profile trends occurring over a length scale of a few times 10,000 km—which micron-sized grains cover over a timescale of days—therefore all appear broadly consistent with the sublimation of micron-sized, carbon-filled water ice grains.

Water ice grains have also been previously detected in other comets through the characteristic near-infrared absorption bands near wavelengths of 1.5 and 2.0 μm (e.g., Kawakita et al. 2004; Protopapa et al. 2018). Kareta et al. (2021) recently confirmed the presence of these absorption bands in the coma of C/2017 K2 with near-infrared spectroscopy on 2021 April 30 at $r = 6.49$ au. Their spectral extraction region covered the portion of the coma at $\rho < 4'' \sim 18{,}000$ km where we infer micron-sized grains to be abundant, so the observed absorption features may originate from these same grains. However, without a comparison with the strength of the absorption bands in the outer coma, we cannot exclude that these observations are instead sampling a separate, longer-lived icy grain population unrelated to our observed optical signatures.

These 1.5 and 2.0 μm features also contribute a blue near-infrared color that could, in theory, be imaged if the water ice abundance is sufficiently high (Hanner 1981). We searched for a corresponding halo of relatively bluer dust in the near-infrared colors, but the coma appears featureless in our $J-H$, $H-K_s$, and $J-K_s$ color maps, beyond likely artifacts from alignment errors and PSF variations. Figure 3.5 presents radial profiles of these colors, which reveal no clear trend out to $\rho \sim 70{,}000$ km above the level of systematic uncertainty arising from background subtraction. Comparison with Kareta et al. (2021) suggests our sensitivity limit was likely near the level of the absorption features, and so may not have been sufficient to distinguish spatial variations in those features if they did exist. We measured $J = 12.32 \pm 0.02$, $H = 11.94 \pm 0.02$, and $K_s = 11.91 \pm 0.03$ within a circular aperture of radius $\rho = 70{,}000$ km, corresponding to $J - H = 0.38 \pm 0.03$ and $H - K_s = 0.03 \pm 0.04$.

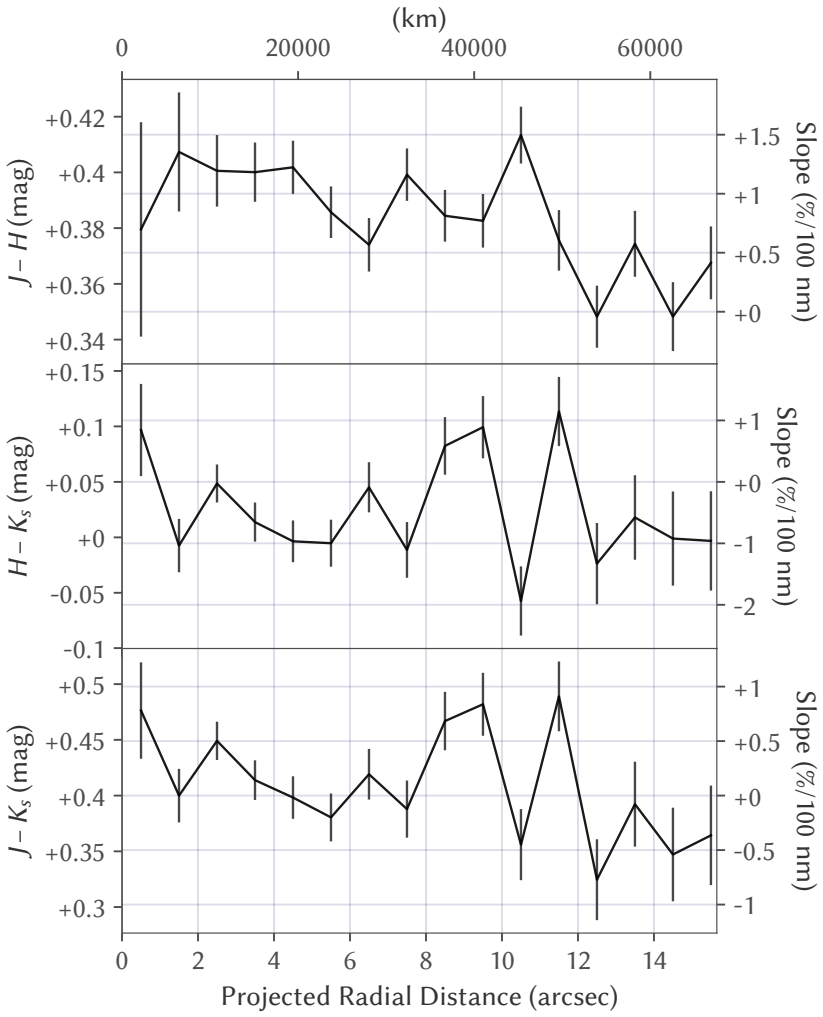

Figure 3.5: Radial profiles of $J - H$ (top), $H - K_s$ (middle), and $J - K_s$ (bottom) colors from Palomar/WIRC on 2021 May 18, showing no clear trend in any color above the noise limit.

These colors are comparable to the typical $J-H = 0.41\pm0.06$ and $H-K = 0.14\pm0.05$ for comets measured by Jewitt & Meech (1988), albeit slightly bluer than average.

3.3.5 Comparison with Other Distant Comets

The relatively featureless inner coma color and polarization maps of C/2017 K2 stands in contrast to those of C/1995 O1 (Hale–Bopp), which showed prominent reddened and positively polarized (near +2%) jets superimposed on a strongly negatively polarized (near −5%) halo at a similar $\alpha = 6^\circ.9$, but at a closer $r = 4.1$ au (Hadamcik & Levasseur-Regourd 2003a). Similarly negatively polarized halos appear around a number of periodic comets (Hadamcik & Levasseur-Regourd 2003b;

Hadamcik et al. 2016), although some of these halos may instead be recording the polarization of the nucleus (Kiselev et al. 2020). It remains unclear how many of observed differences are due to true physical differences between the physical properties of these comets, or if similar features will develop on C/2017 K2 as it approaches the Sun.

Additionally, Hines et al. (2013) collected HST imaging polarimetry of C/2012 S1 (ISON) at $r = 3.81$ au and $\alpha = 12^{\circ}.16$. They found its coma to be weakly polarized at a similar -1.6% through F606W (approximately V) within a projected $\rho \sim 5{,}000$ km, except for a sharp, +2% polarized peak at $\rho \lesssim 500$ km. We revisited that data set in Appendix 3.5.2 and determined this feature to be a processing artifact. Correction of this artifact leaves the coma polarization indistinguishable from uniform.

On the other hand, halos of relatively bluer dust, as observed on C/2017 K2, have been previously observed in other distant comets, including C/1995 O1 (Hale–Bopp) at $r \sim 12$ au (Weiler et al. 2003) and C/2003 WT_{42} (LINEAR) at $r \sim 5$ au (Korsun et al. 2010). HST also observed one such halo extending out to $\rho \sim 10{,}000$ km around C/2012 S1 (ISON) at $r \sim 4$ au (Li et al. 2013). These features may similarly reflect an abundance of short-lived ice grains produced by those comets. However, unlike C/2017 K2, the optical halo around C/2012 S1 was not accompanied by detectable 1.5 and 2.0 μm absorption (Yang 2013), which Li et al. (2013) proposes could be explained if the icy grains of C/2012 S1 were much smaller, as the absorption features for submillimeter ice grains are much weaker than for larger grains (Hansen & McCord 2004). In contrast, another dynamically new Oort cloud comet, C/2013 US_{10} (Catalina), presented 1.5 and 2.0 μm water ice absorption features at $r \gtrsim 3$ au that were similarly attributed to micron-sized, darkened water ice grains (Protopapa et al. 2018). However, no contemporaneous optical observations of this comet are available that could constrain the presence of any corresponding optical halo.

Finally, many distant comets have been clearly observed to not exhibit blue halos, with some (e.g., C/2014 A4; Ivanova et al. 2019) instead exhibiting similarly-sized red halos that require alternative, or at least modified explanations. More extensive optical and near-infrared observations together with more detailed modeling of C/2017 K2 and other distant comets will be required to more firmly and generally connect observed dust behavior to properties of their nuclei.

3.4 Conclusions

We observed the inbound Oort cloud comet C/2017 K2 with HST ACS/WFC at $r = 6.82$ au and found that

1. The dust at $\rho \lesssim 10{,}000$ km from the nucleus appeared consistent with being spatially uniform in optical color and polarization, with a $1/\rho$ steady-state brightness profile.

2. The dust becomes increasingly redder and more strongly negatively polarized beyond $\rho \sim 10{,}000$ km. The F475W–F775W reflectance slope increases from about 4.5% to 7% per 100 nm, and the polarization strengthened from −2% to −3.5% between $\rho \sim 10{,}000$ km and 50,000 km.

3. The observed radial intensity profiles are indistinguishable from a steady-state $1/\rho$ profile within $\rho \sim 10{,}000$ km—much shallower than expected by a Monte Carlo model of stable, millimeter-sized grains—then steepen farther out, as measured by the gradient in scattering cross section within annuli.

We also observed the comet 60 d later with Palomar/WIRC at $r = 6.34$ au and found that

1. The tail continues to lack micron-sized grains, with none ejected near the HST epoch being visible alongside an abundance of older, millimeter-sized dust.

2. The coma exhibits typical $J - H = 0.38 \pm 0.03$ and $H - K_s = 0.03 \pm 0.04$, with no distinguishable radial trend.

We conclude from these observed dust properties that

1. At least one component of the dust produced by C/2017 K2 breaks down over a distance on the order of a few times 10,000 km at $r = 6.82$ au.

2. The short-lived component may take the form of micron-sized water ice grains darkened by a small fraction of highly absorbing contaminant, such as carbon. Their expected sublimation lifetime on the order of a day appears broadly consistent with the observed color, polarization, and intensity profiles.

Finally, we showed that

1. The positive polarization reported by Hines et al. (2013) over the nucleus of C/2012 S1 (ISON) is likely an artifact of trailing in one of the polarized frames collected by their program. The polarization otherwise appears indistinguishable from uniform, like that of C/2017 K2's inner coma.

2. Ground-based astrometry of C/2017 K2 exhibits a tailward bias of ∼0″.6 near the epoch of our HST observations that already far exceeds the effect of random noise on the orbital solution. Future investigations into the dynamical history or nongravitational acceleration of this comet that incorporate such data must accordingly model this bias.

3.5 Appendix

3.5.1 HST ACS/WFC Frame Preparation

We initially processed all ten raw science frames by reapplying the calibration frames using the ACS Destripe Plus routine supplied by ACSTools (Lim et al. 2020), with the "destripe" setting on to remove banding artifacts, and used STWCS (Dencheva et al. 2011) to load an initial distortion-corrected astrometric solution for each frame. We then used the Gaia EDR3 catalog (Gaia Collaboration et al. 2021, 2016) and Tiny Tim model PSFs (Krist et al. 2011) to generate simulated frames with the star trails in each observed frame, then cross correlated the simulated and observed frames to determine their relative shifts and subsequently correct the errors in the astrometric solutions of the observed frames.

We fitted for the position of the comet nucleus in every frame by modeling the coma as a 2D Moffat function (Moffat 1969) with a FWHM matching that of the corresponding Tiny Tim PSF and a power index of 0.5 to approximate a $1/\rho$ brightness profile convolved with the PSF. Comparison of the fitted positions with JPL orbit solution 63 reveals a consistent sunward offset of ∼0″.6. We shifted the JPL ephemerides by the mean offset measured from all frames to obtain the nucleus position for frame alignment and further processing. We attribute this large offset to a ∼0″.6 average tailward bias in the ground-based astrometry used for the orbit determination, whereby the fitted center of light is offset from the true position of the nucleus in the tailward direction (e.g., Farnocchia et al. 2016). While not abnormal in magnitude, our measured offset falls well outside the $3\sigma = 0''.09 \times 0''.06$ formal error ellipse of the orbit solution, indicating that tailward bias must be modeled in any future dynamical investigations of this comet that require reliable measures of orbital uncertainty.

Next, we prepared all frames for combination by masking pixels flagged with data quality issues, as well as those contaminated by the trails of all Gaia EDR3 stars. We also performed rudimentary cosmic ray rejection by masking all pixels and neighbors to pixels where the flux within a centered 1 FWHM radius aperture (i.e., peak brightness) divided by the median brightness in a 1–2 FWHM annulus minus that of a 2–3 FWHM annulus (i.e., wing brightness) exceeds the ratio for the equivalent Tiny Tim PSF model by more than a 3σ noise buffer (i.e., masking the peaks that are sharper than a point source as cosmic rays). We then projected all frames and associated masks onto a new rectilinear pixel grid at half the pixel scale, with each frame centered on their respective corrected ephemeris position, and interpolated pixel uncertainties onto the same grid. We performed a second round of star and cosmic ray masking by comparing the exposure-normalized brightness of unmasked pixels between each pair of identically filtered frames, masking the brighter pixel and its neighbors when more than four times brighter than the formal uncertainty of the fainter pixel.

We combined each pair of frames as the minimum of the two frames for pixels are not masked in either frame, as a final star and cosmic ray rejection step. The minimum of two values with a random error σ is typically lower than their mean by $\sigma/\sqrt{\pi}$, which we approximately corrected using the formal σ of the fainter pixel. We then filled in pixels masked in both frames with the values of adjacent pixels. Finally, we subtracted the background brightness measured as the sigma-clipped median in the ρ = 25″–35″ (~124,000–174,000 km) region to the sunward side of the nucleus, beyond where the coma has been visibly truncated by the radiation pressure. We evaluated the background brightness uncertainty by measuring the brightness in annular subsets and found variations limited to $\lesssim$1% of the average coma brightness at ρ = 12″.5, and restricted our analysis to this region.

This procedure produces five combined science frames, one for each of the five unique filter combinations used, which serve as the direct inputs to produce the color and polarization maps, as discussed in Section 3.2.1.

3.5.2 Revisiting C/2012 S1 (ISON)

We revisited the results of Hines et al. (2013), which found an unusual positively polarized region over the nucleus of comet C/2012 S1 (ISON) in HST ACS/WFC polarimetry through F606W when the comet was at r = 3.81 au, Δ = 4.34 au, and α = 12°.16. We processed the six polarized frames taken by the associated HST

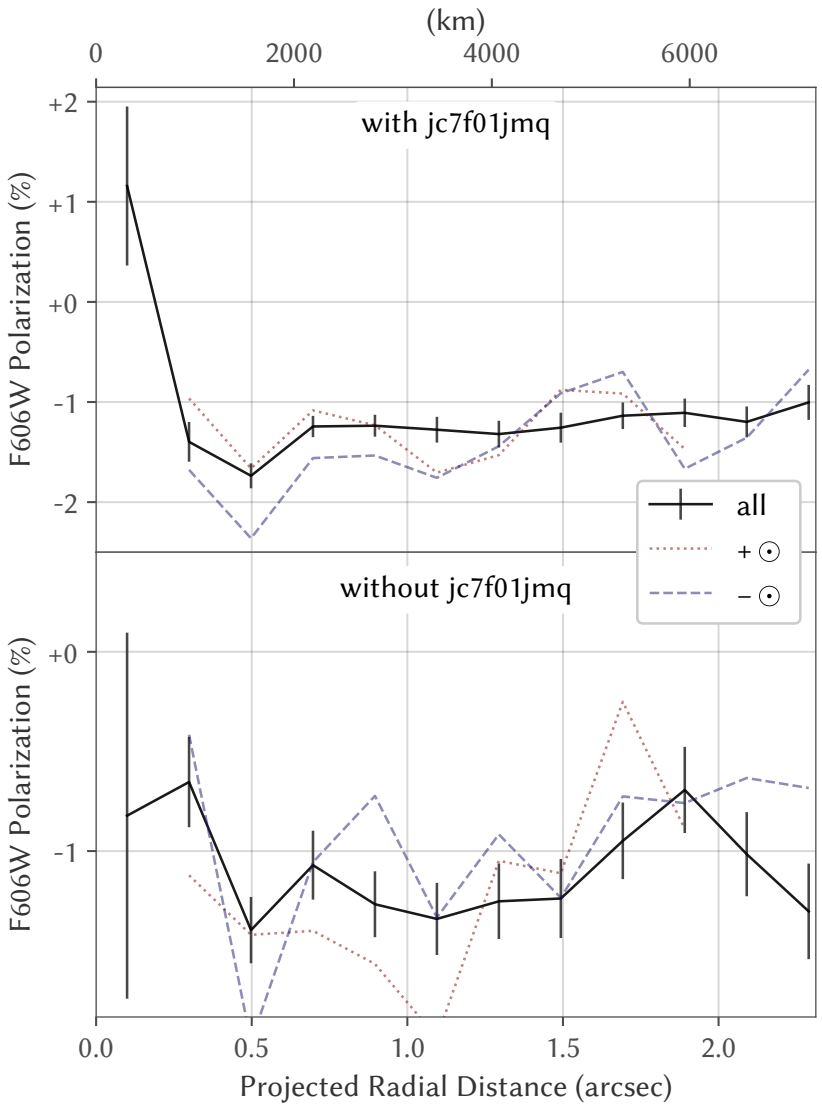

Figure 3.6: Radial profiles of the polarization of C/2012 S1 (ISON), analogous to the one in Figure 3.2 for C/2017 K2, processed from data collected by HST program GO/DD 13199 (PI: D. Hines) with all frames included (top) and excluding the trailed POL60V frame jc7f01jmq (bottom), showing that removal of this trailed frame effectively eliminates the apparent positively polarized region over the nucleus.

program GO/DD 13199 between 2013 May 7 19:47 and 2013 May 8 00:22 using the same procedure described in Section 3.2.1 and Appendix 3.5.1, and successfully reproduced the sharp, positively polarized region over the nucleus, as shown in the top panel of Figure 3.6.

However, a frame-by-frame investigation of the collected data revealed that the first of the two POL60V frames (ID: jc7f01jmq) captured a ~1–2 px tracking error that

is visually apparent as a break in the background star trails, and noticeably trails the near-nucleus coma. Excluding this single frame from the reduction eliminates the positively polarized peak, as shown in the bottom panel of Figure 3.6. This feature was therefore most likely an artifact of the trailed PSF artificially lowering the measured brightness of the near-nucleus coma in the POL60V stack. No such tracking errors appear to impact any of our C/2017 K2 frames.

References

A'Hearn, M. F., Millis, R. C., Schleicher, D. G., Osip, D. J., & Birch, P. V. 1995, Icar, 118, 223

A'Hearn, M. F., Schleicher, D., Millis, R., Feldman, P., & Thompson, D. 1984, AJ, 89, 579

Beer, E., Podolak, M., , & Prialnik, D. 2006, Icar, 180, 473

Biretta, J. 2004, ACS Polarimetry Calibration, HST Proposal

Clarke, D. 1974, in Planets, Stars and Nebulae Studied with Photopolarimetry, ed. T. Gehrel (Tucson, AZ: Univ. of Arizona Press), 45–53

Combi, M. R. 1994, AJ, 108, 304

Dencheva, N., Hack, W., Droetboom, M., Fruchter, A., & Greenfield, P. 2011, in Astronomical Data Analysis Software and Systems XX, Vol. 442, 73

Farnocchia, D., Chesley, S. R., Micheli, M., et al. 2016, Icar, 266, 279

Finson, M., & Probstein, R. 1968, ApJ, 154, 327

Gaia Collaboration, Brown, A. G., Vallenari, A., et al. 2021, A&A, 649, A1

Gaia Collaboration, Prusti, T., De Bruijne, J., et al. 2016, A&A, 595, A1

Gehrz, R., & Ney, E. 1992, Icar, 100, 162

Hadamcik, E., & Levasseur-Regourd, A. C. 2003a, A&A, 403, 757

Hadamcik, E., & Levasseur-Regourd, A.-C. 2003b, JQSRT, 79, 661

Hadamcik, E., Levasseur-Regourd, A. C., Hines, D. C., et al. 2016, MNRAS, 462, S507

Hanner, M., Gehrz, R., Harker, D. E., et al. 1998, EM&P, 79, 247

Hanner, M. S. 1981, Icar, 47, 342

Hansen, G. B., & McCord, T. B. 2004, JGR, 109

Hines, D. C., Videen, G., Zubko, E., et al. 2013, ApJL, 780, L32

Hoban, S., A'Hearn, M. F., Birch, P. V., & Martin, R. 1989, Icar, 79, 145

Hui, M.-T., Farnocchia, D., & Micheli, M. 2019, AJ, 157, 162

Hui, M.-T., Jewitt, D., & Clark, D. 2017, AJ, 155, 25

Ivanova, O., Luk'yanyk, I., Kolokolova, L., et al. 2019, A&A, 626, A26

Jewitt, D., Agarwal, J., Hui, M.-T., et al. 2019, AJ, 157, 65

Jewitt, D., Kim, Y., Mutchler, M., et al. 2021, AJ, 161, 188

Jewitt, D., & Meech, K. 1988, AJ, 96, 1723

Kaiser, N., Aussel, H., Burke, B. E., et al. 2002, Proc. SPIE, 4836, 154

Kareta, T., Harris, W. M., & Reddy, V. 2021, RNAAS, 5, 153

Kawakita, H., Watanabe, J.-i., Ootsubo, T., et al. 2004, ApJL, 601, L191

Kimura, H. 2017, ApJL, 839, L23

Kiselev, N., Rosenbush, V., Ivanova, O., et al. 2020, Icar, 348, 113768

Kolokolova, L., Hanner, M. S., Levasseur-Regourd, A.-C., Gustafson, B. Å., et al. 2004, in Comets II, ed. M. Festou, H. U. Keller, & H. A. Weaver (Tucson, AZ: Univ. of Arizona Press), 577–604

Korsun, P. P., Kulyk, I. V., Ivanova, O. V., et al. 2010, Icar, 210, 916

Krist, J. E., Hook, R. N., & Stoehr, F. 2011, Proc. SPIE, 8127, 81270J

Królikowska, M., & Dybczyński, P. A. 2018, arXiv:1802.10380v3

Levasseur-Regourd, A., Shkuratov, Y., Renard, J., & Hadamcik, E. 2015, in Polarimetry of Stars and Planetary Systems, ed. L. Kolokolova, J. Hough, & A. Levasseur-Regourd (Cambridge: Cambridge Univ. Press), 62–80

Li, J.-Y., Kelley, M. S., Knight, M. M., et al. 2013, ApJL, 779, L3

Lim, P. L., Davis, M., Hack, W., et al. 2020, ASCL, 2011

Meech, K. J. 1989, in IAU Colloq. 116: Comets in the post-Halley era, ed. J. Newburn, R. L., M. Neugebauer, & J. Rahe, Vol. 167, Cambridge University Press, 629–669

Meech, K. J., Kleyna, J. T., Hainaut, O., et al. 2017, ApJL, 849, L8

Moffat, A. 1969, A&A, 3, 455

Protopapa, S., Kelley, M. S., Yang, B., et al. 2018, ApJL, 862, L16

Skrutskie, M., Cutri, R., Stiening, R., et al. 2006, AJ, 131, 1163

Solontoi, M., Ivezić, Ž., Jurić, M., et al. 2012, Icar, 218, 571

Weiler, M., Rauer, H., Knollenberg, J., Jorda, L., & Helbert, J. 2003, A&A, 403, 313

Whipple, F. L. 1951, ApJ, 113, 464

Williams, G. V. 2017, MPEC, 2017-K35

Willmer, C. N. 2018, ApJS, 236, 47

Yang, B. 2013, CBET, 3622

Yang, B., Jewitt, D., Zhao, Y., et al. 2021, ApJL, 914, L17

Ye, Q.-Z., Hui, M.-T., Brown, P. G., et al. 2016, Icar, 264, 48

Chapter 4

SODIUM BRIGHTENING OF (3200) PHAETHON NEAR PERIHELION

Zhang, Q., Battams, K., Ye, Q., Knight, M. M., & Schmidt, C. A. 2023, PSJ, 4, 70, doi: 10.3847/PSJ/acc866

4.1 Introduction

Near-Earth asteroid (3200) Phaethon is recognized as the likely parent of the Geminids meteoroid stream (e.g., Davies et al. 1984; Fox et al. 1984; Gustafson 1989; Whipple 1983). Unlike typical icy, cometary meteoroid progenitors, Phaethon has never been observed to present any measurable dust or gas production while near or beyond Earth's orbit (e.g., Hsieh & Jewitt 2005; Jewitt et al. 2019; Wiegert et al. 2008; Ye et al. 2021). While formerly active comets that have exhausted their accessible supply of icy volatiles can appear similarly devoid of activity (e.g., Asher et al. 1994; Jewitt 2005), Phaethon exhibits higher albedo (Green et al. 1985), bluer optical and near-infrared colors (Binzel et al. 2001; Green et al. 1985), and a higher bulk density (Hanuš et al. 2018) than typical of cometary nuclei. Dynamical simulations also indicate that Phaethon most likely originated from the Main Belt like most near-Earth asteroids, rather than the Kuiper Belt or Oort Cloud from which comets are typically sourced (e.g., Bottke Jr et al. 2002; de León et al. 2010). Meanwhile, its dynamical lifetime appears too long for water ice to survive even deep within its interior (Jewitt & Li 2010).

Phaethon, however, approaches the Sun more closely than any other known asteroid of its size, to a sunskirting perihelion distance of only $q = 0.14$ au (Jones et al. 2018). The intense solar heating at such distances can volatilize material much more refractory than water ice to potentially produce comet-like, sublimation-driven activity on even an ice-free Phaethon (e.g., Lisse & Steckloff 2022; Mann et al. 2004; Masiero et al. 2021). While its low solar elongation near perihelion thwarts observation of the asteroid by nighttime astronomical facilities during this period, space-borne heliospheric observatories, like the twin Solar Terrestrial Relations Observatory Ahead and Behind (STEREO-A and B) spacecraft (Kaiser et al. 2008), do not face this limitation. STEREO-A's Heliospheric Imager 1 (HI1) camera (Eyles et al. 2009) provided the first reported direct observations of Phaethon near

perihelion, which showed that the asteroid underwent a sudden brightening episode during the 2009 apparition that peaked a few hours after perihelion and faded within 2 days (Battams & Watson 2009).

Jewitt & Li (2010) attributed the observed brightening to an impulsive ejection of dust grains from Phaethon's surface, implying that the asteroid is indeed actively losing mass, albeit at a level insufficient to sustain the Geminids stream. The subsequent observable apparitions in 2012 (Li & Jewitt 2013) and 2016 (Hui & Li 2017) showed this brightening to be a recurrent phenomenon that repeats with nearly identical timing and amplitude each orbit. Jewitt et al. (2013) performed a more careful analysis of the HI1 imagery that further revealed a tail extending a few arcminutes antisunward from Phaethon that develops over the course of ∼1 day alongside the brightening, and attributed this tail to micron-sized dust grains being rapidly accelerated and swiftly dispersed by solar radiation pressure. Such grains would constitute a class of dust distinct from the millimeter-sized and larger grains still orbiting alongside Phaethon as part of the Geminids meteoroid stream.

Our current analyses, however, show that the observed brightening and tail cannot be attributed to dust grains of any form. In the following sections, we present additional observations of Phaethon's activity collected by the HI1 cameras of both STEREO-A and B, as well as by the Large Angle Spectrometric Coronagraph (LASCO) C2 and C3 coronagraphs (Brueckner et al. 1995) onboard the Solar and Heliospheric Observatory (SOHO) spacecraft (Domingo et al. 1995). We use the morphology and photometry provided by these observations to demonstrate that Phaethon's observed brightening and tail actually capture resonance fluorescence by atomic sodium (henceforth, Na I) liberated under solar heating, compare this behavior with that of several other sunskirting objects, and discuss the associated implications on the formation of the Geminids stream.

4.2 Data

Phaethon's perihelic activity has previously only ever been reported to be seen by STEREO-A HI1, with detailed analyses published of the 2009, 2012, and 2016 apparitions as discussed above. Phaethon, however, should also have been observable by STEREO-B HI1 near perihelion in several apparitions, and crosses the field of SOHO LASCO C3, if not also C2, near perihelion in every apparition. We anticipated the 2022 apparition to be particularly favorable for LASCO, with Phaethon crossing the C2 field ∼0.5 day after perihelion at the expected peak of its brighten-

ing, and carried out a special observing sequence with both coronagraphs to better characterize the activity with higher spatial resolution through photometric bandpasses different from that of previously analyzed HI1 data. Below, we discuss our analysis of both the new and archival data, which collectively capture Phaethon's activity in all 18 apparitions from 1997 to 2022, as summarized in Table 4.1.

4.2.1 Instruments

4.2.1.1 STEREO-A/B HI1

The STEREO mission involves two, functionally identical spacecraft on heliocentric orbits similar to that of Earth (Kaiser et al. 2008): STEREO-A, which orbits slightly interior to and faster than Earth, and STEREO-B, which orbits slightly exterior to and slower than Earth. Their slight orbital differences cause them to separate, drifting from Earth at ∼22 deg yr^{-1}. Since the commencement of standard operations in 2007 January, STEREO-A and B have drifted nearly one complete orbit ahead and behind to return to the vicinity of Earth in 2023, although STEREO-B ceased operations in 2014 after its loss of contact (Ossing et al. 2018).

The Sun Earth Connection Coronal and Heliospheric Investigation (SECCHI) instrument suite (Howard et al. 2008) onboard each spacecraft contains a pair of coronagraphs (COR1/2) and heliospheric imagers (HI1/2). Our analysis covers only the HI1 instruments, the inner heliospheric imagers targeting the region of sky between 4° and 24° from the Sun along the Sun–Earth line—fields well-suited to observing Phaethon near perihelion. Each camera has an unbinned image scale of 36 arcsec px^{-1} (Brown et al. 2009). Under its standard, synoptic observing program, HI1 typically returns 36 onboard-processed frames per day, each of which is a sum of 30×40 s exposures binned 2×2 to 72 arcsec px^{-1}. For our analysis, we used the standard level 2 data, which provide astrometric calibrations and eliminate the gradient of the F-corona through subtraction of a background frame calculated as the mean of the lowest quartile of each pixel across all frames over a 1 day window. However, we used the updated photometric calibrations by Tappin et al. (2017) and Tappin et al. (2022) in place of the standard level 2 photometric calibrations. To improve sensitivity, we also subtracted field stars from each frame, using a sidereally-aligned median stack of neighboring frames for the stellar background model.

Each HI1 camera observes through a fixed bandpass filter, which preflight calibrations showed had full width at half maximum (FWHM) wavelength spans of

Table 4.1: Observable Apparitions of (3200) Phaethon

Apparition T_p (UT)[a]	Instrument	Observable Period (UT)[b]
1996 Jul 25 23:49	SOHO LASCO C3	Jul 24–27[c]
1997 Dec 31 13:25	SOHO LASCO C3	Dec 30–1998 Jan 02
1999 Jun 08 03:21	SOHO LASCO C2	Jun 08–09
	SOHO LASCO C3	Jun 06–08[c]
2000 Nov 12 20:19	SOHO LASCO C2	Nov 12–13
	SOHO LASCO C3	Nov 11–14
2002 Apr 20 09:52	SOHO LASCO C3	Apr 18–21
2003 Sep 25 22:55	SOHO LASCO C3	Sep 24–27
2005 Mar 02 13:04	SOHO LASCO C3	Feb 28–Mar 02
2006 Aug 08 04:13	SOHO LASCO C3	Aug 06–09
2008 Jan 13 18:54	SOHO LASCO C3	Jan 13–15
	STEREO-B HI1	Jan 03–13
2009 Jun 20 07:21	SOHO LASCO C2	Jun 21–22
	SOHO LASCO C3	Jun 19–21
	STEREO-A HI1	Jun 17–22
	STEREO-B HI1	Jun 21–30
2010 Nov 25 17:51	SOHO LASCO C2	Nov 25–26
	SOHO LASCO C3	Nov 24–27
	STEREO-B HI1	Nov 15–19[c]
2012 May 02 07:48	SOHO LASCO C3	Apr 30–May 03
	STEREO-A HI1	Apr 30–May 04
	STEREO-B HI1	Apr 22–May 03
2013 Oct 07 21:18	SOHO LASCO C3	Oct 06–09
	STEREO-B HI1	Oct 09–18[c]
2015 Mar 15 07:47	SOHO LASCO C3	Mar 13–15
2016 Aug 19 19:45	SOHO LASCO C3	Aug 18–20
	STEREO-A HI1	Aug 18–30
2018 Jan 25 08:24	SOHO LASCO C3	Jan 25–27
2019 Jul 02 23:59	SOHO LASCO C3	Jul 02–04
	STEREO-A HI1	Jul 03–13
2020 Dec 07 14:35	SOHO LASCO C2	Dec 08–09
	SOHO LASCO C3	Dec 06–09
2022 May 15 04:21	SOHO LASCO C2	May 15
	SOHO LASCO C3	May 13–17[d]
	STEREO-A HI1	May 15–25[e]

[a]Time of perihelion for apparition.

[b]Period with Phaethon observable in the field of C2/C3 at $r < 0.16$ au, or in the field of HI1 at $r < 0.4$ au (but only periods containing $r < 0.16$ au are listed).

[c]Insufficient sensitivity for clear detection of activity.

[d]Only detected in special May 15–16 Orange observations.

[e]Only May 15–20 included in analysis.

~615–740 nm, with a blue leak near 400 nm and a red leak near 1000 nm (Bewsher et al. 2010). The filters effectively blocked the 589.0/589.6 nm Na I D resonance lines with a relative transmission of only 1–2%, which led Jewitt et al. (2013) and Hui & Li (2017) to rule out Na I D emission as the source of Phaethon's brightening in HI1. However, the appearance of Mercury's Na I tail several times brighter than expected in HI1 called the preflight filter measurements into question (Schmidt et al. 2010a). Halain (2012) subsequently re-evaluated the filter transmission on the HI1 engineering qualification model, which revealed the true HI1 bandpass to actually be blueshifted from preflight values by ~20 nm, raising the relative Na I D transmission to ~15%, roughly in line with observations. The MESSENGER mission has shown that Mercury's Na escape rate varies in a seasonally repeating pattern (Cassidy et al. 2021). This property enables us to use the tail as a flux standard to calibrate HI1's sensitivity to Na I D emission, as we present in Appendix 4.6.1.

4.2.1.2 SOHO LASCO C2/C3

Unlike STEREO, SOHO monitors the Sun and the heliospheric environment from the vicinity of Earth in a halo orbit around the Sun–Earth L1 point. Its LASCO C2 and C3 coronagraphs have observed thousands of other objects active near the Sun, and unlike HI1, each contain a set of interchangeable bandpass filters that can measure the colors of observation targets (Battams & Knight 2017). LASCO C2 covers a narrow region 1.5–6 $R_\odot$ above the solar limb at 12 arcsec px^{-1}, while LASCO C3 observes a wider region 3.7–30 $R_\odot$ from the limb at a coarser 56 arcsec px^{-1}. Under their standard, synoptic program, C2 and C3 generally alternate in observations, presently with a 12 minute interval between images from the same camera. C2 records 25 s exposures through a ~540–620 nm (FWHM span) Orange filter while C3 records 18 s exposures through a ~530–840 nm Clear filter, with only sporadic exposures through other filters (Battams & Knight 2017). Special observing sequences can be scheduled several days in advance to use other filter and exposure combinations.

For our analyses, we began with the minimally processed level 0.5 data and applied the equivalent of level 1 bias and vignetting corrections (Thernisien et al. 2003). We also removed the coronal gradient by subtracting the median of exposure-normalized frames with the same camera/filter combination in each apparition as a background frame. To avoid further degradation to LASCO's already undersampled point spread functions (PSFs), we skipped the level 1 stage that corrects image distortions

by interpolation onto an undistorted grid. We instead incorporated the supplied radial polynomial distortion coefficients into our astrometric solutions, which we then fitted to stars in the Gaia DR3 catalog (Gaia Collaboration et al. 2022). Visual inspection suggests these solutions are accurate to <1 px over roughly half the C2 field, and over all but the inner and outermost few percent of the C3 field. We also performed new photometric calibrations of C2 and C3 that span SOHO's lifetime in order to more confidently constrain potential variations in the sensitivity of the cameras over time. We present these calibrations in Appendix 4.6.2.

4.2.2 Observations

4.2.2.1 2022 Apparition

During its 2022 apparition, Phaethon reached perihelion at 2022 May 15 04:21 UT (JPL orbit solution 777). It crossed the LASCO C3 field of view over May 14–17 and the C2 field of view on May 15 13–20h UT, with the latter interval coinciding with the timing of Phaethon's previously reported HI1 brightening peak ~0.5 days after perihelion. We conducted a special sequence of color observations to characterize Phaethon with LASCO within this period. Phaethon also entered the STEREO-A HI1 field of view on May 15 where it was concurrently monitored by the standard, synoptic observing program alongside our special LASCO C2 and C3 observations, and for the remainder of the apparition. Figure 4.1 illustrates Phaethon's trajectory through the fields of all three cameras.

Typical sunskirting comets tend to appear much brighter in Orange than in Clear-filtered observations, often by $\gtrsim$1 mag relative to solar color, due to intense Na I fluorescence that outshines the sunlight scattered by dust (e.g., Biesecker et al. 2002; Knight et al. 2010; Lamy et al. 2013). Both the Orange and Clear filters strongly transmit the Na I D lines, but the much narrower Orange bandpass preferentially transmits Na I D emission relative to light with Sun-like spectra, leading pure Na I D emission to appear ~1.3 mag brighter in Orange than in Clear data, as calculated in Appendix 4.6.2. We considered that Phaethon may behave similarly, so to improve LASCO's sensitivity to Phaethon's potential Na I activity, we scheduled a sequence of mainly 60 s Orange exposures by both C2 and C3 spanning 2022 May 15 0h and May 16 12h, with only C2 observations during its May 15 13–20h window, and C3 observations filling the remaining time. We also scheduled blocks of 120 s exposures through the ~460–515 nm C2 and C3 Blue filters, which effectively block Na I D emission at <1% relative transmission, to constrain the presence of any micron-sized

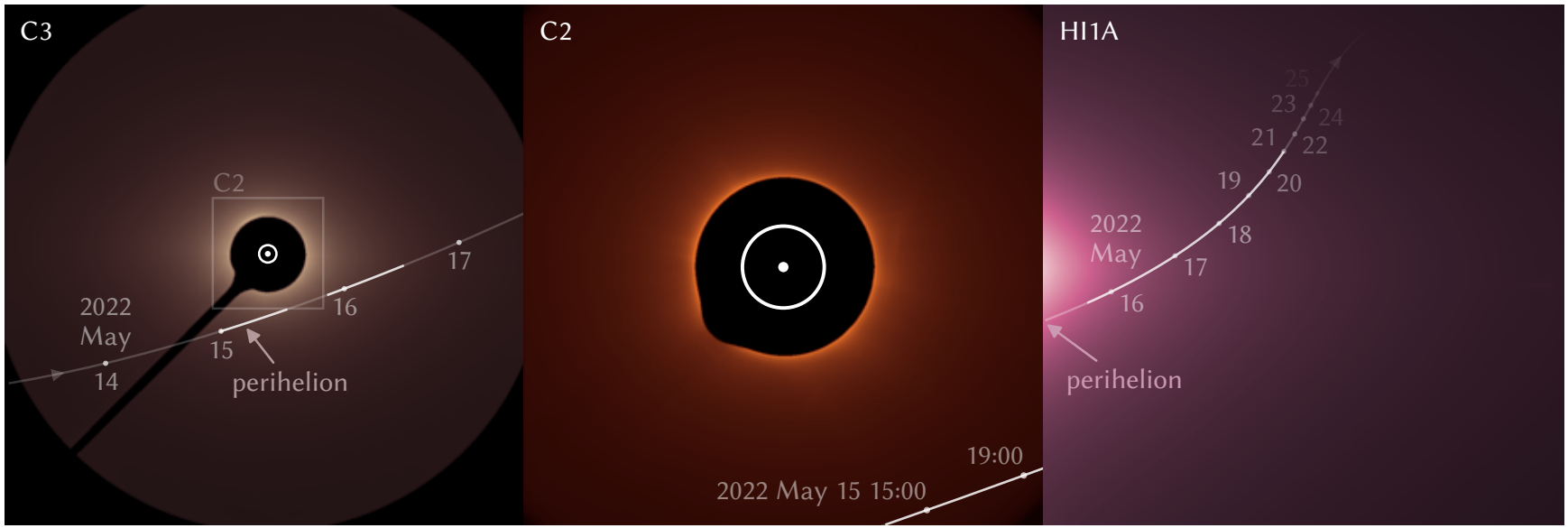

Figure 4.1: Apparent trajectory of (3200) Phaethon during its 2022 apparition through the fields of view of the SOHO LASCO C3 (left) and C2 (middle) coronagraphs, and of the STEREO-A HI1 imager (HI1A; right), with dates and the location of perihelion labeled. Highlighted sections of the track indicate periods of each camera's observations included in our analysis of this apparition. The ⊙ markers on the C3 and C2 panels indicate the size and position of the Sun behind each camera's occulter, while the square on the C3 panel indicates the relative field of view of C2. The Sun is off the left edge of the HI1A frame.

Table 4.2: Observations from the 2022 Apparition of (3200) Phaethon

Instrument	Exposures	Observation Time (UT)	r (au)[a]	Δ (au)[b]	α (°)[c]
SOHO LASCO C3	166 × 60 s Orange	2022 May 15 00:00–12:41, 23:03–May 16 11:57	0.140–0.151	0.863–0.868	151.2–167.1
	19 × 120 s Blue	2022 May 15 20:39–22:57	0.143–0.144	0.863	162.7–164.3
SOHO LASCO C2	30 × 60 s Orange	2022 May 15 13:14–15:07, 17:42–20:03	0.141–0.143	0.863	164.4–167.1
	15 × 120 s Blue	2022 May 15 15:16–17:35	0.142	0.863	166.0–166.8
STEREO-A HI1[d]	152 × 1200 s	2022 May 15 16:23 –May 20 23:53	0.142–0.270	0.856–1.067	60.4–135.7

[a]Heliocentric distance.

[b]Distance from observer.

[c]Phase angle.

[d]Data from standard, synoptic observing program.

dust associated with the activity. Table 4.2 summarizes these observations.

The plan immediately proved successful, with Phaethon appearing so bright in our C2 Orange frames that it was unwittingly noticed and reported to the Sungrazer citizen science project as a new comet by Zhijian Xu. Closer inspection also revealed it to be visible in the C3 Orange sequence, but not in either of the Blue sequences. Figure 4.2 compares the 2.5σ-clipped, JPL Horizons ephemeris-aligned stacks of all Orange and Blue frames from each camera, illustrating Phaethon's activity to be prominent in Orange at apparent magnitude 8.8 in C2 within a 45″ radius aperture, yet not at all in Blue to a 3σ limiting magnitude of 10.9.

Thanks to the strong forward scattering enhancement at its high phase angle of $\alpha \approx 166°$, the C2 Blue limit translates to a stringent absolute magnitude limit of $H > 20.2$ for any comet-like, micron-sized dust following the Schleicher–Marcus phase function (Marcus 2007; Schleicher & Bair 2011), corresponding to a cross section of $\lesssim 0.1$ km^2 at Phaethon's ~11% geometric albedo over visible wavelengths (i.e., including the C2 Blue bandpass; Binzel et al. 2001; MacLennan et al. 2022), or $\lesssim 400$ kg of 1 μm radius grains with a Geminids-like density of 2.6 g cm^{-3} (Borovička et al. 2010)—three orders of magnitude below Jewitt et al. (2013)'s estimate. Following a discussion on our findings, Hui (2023) separately performed a similar analysis showing Phaethon's lack of forward scattering in archival data from STEREO's COR2 coronagraphs, which are also insensitive to Na I D emission, and subsequently arrived at constraints comparable to our result. These initial findings validate our suspicion that Phaethon's activity is observationally similar to that of typical sunskirting comets seen by LASCO, and constitutes our first line of evidence attributing the observed brightening to Na I D emission rather than dust.

4.2.2.2 Earlier Apparitions

Encouraged by the prominence of Phaethon in our 2022 Orange data, we revisited all of the C2 Orange and C3 Clear data collected by the synoptic program over SOHO's operating lifetime where Phaethon was within the frame at $r < 0.16$ au, and produced similar ephemeris-aligned stacks to evaluate Phaethon's activity across apparitions. We repeated the process with both STEREO-A and B HI1 for completeness. In doing so, we recovered Phaethon in LASCO C2 and/or C3 at all 18 apparitions since 1997 as well as at several additional apparitions in HI1, as shown in Figure 4.3. Sensitivity varies between apparitions due to differences in the viewing geometry and track Phaethon takes across each camera's field of view at every apparition,

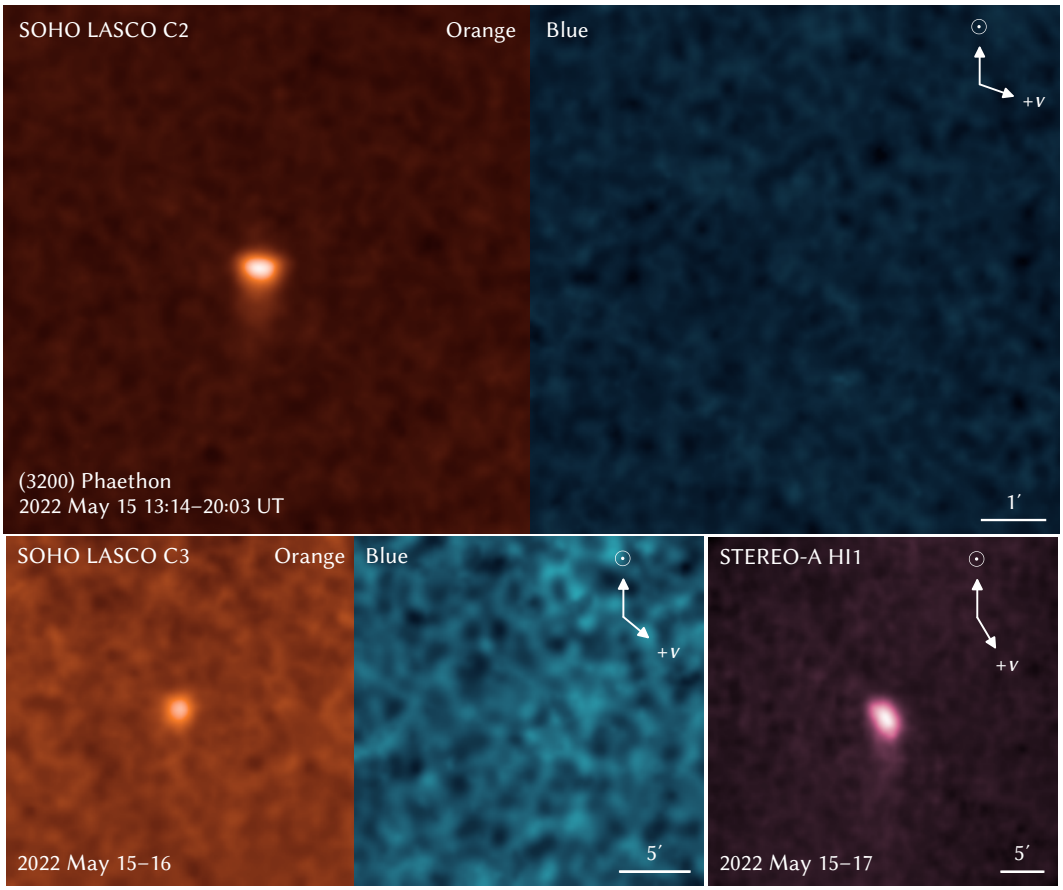

Figure 4.2: Stacked frames of Phaethon during its 2022 apparition from SOHO LASCO C2 (top), LASCO C3 (lower left), and STEREO-A HI1 (lower right). Phaethon and its tail are much brighter through the Orange filters, which transmit Na I D emission, than through the Blue filters, which block Na I D emission and where Phaethon is not visible. Each Orange/Blue pair has been scaled such that a solar-colored source would appear similarly bright in both frames to permit visual comparison. The upward ⊙ arrows indicate the sunward direction, to which individual frames were aligned prior to stacking, while the $+v$ arrows indicate the heliocentric velocity direction near the midpoint time of each stack. The C2 and HI1 stacks show slight trailing due to the motion of Phaethon over individual exposures together with small errors in the astrometric solutions used to align the individual frames.

which affects the both the time span of observations and the level of noise from coronal background, the latter of which increases at lower elongations. Only the 1996 apparition lacks a clear detection due to the low cadence of LASCO data at the commencement of SOHO operations. As we demonstrate in the next section, Phaethon appears brighter in these near-perihelion detections than expected from sunlight scattered by its solid surface alone, indicating they capture the sizable

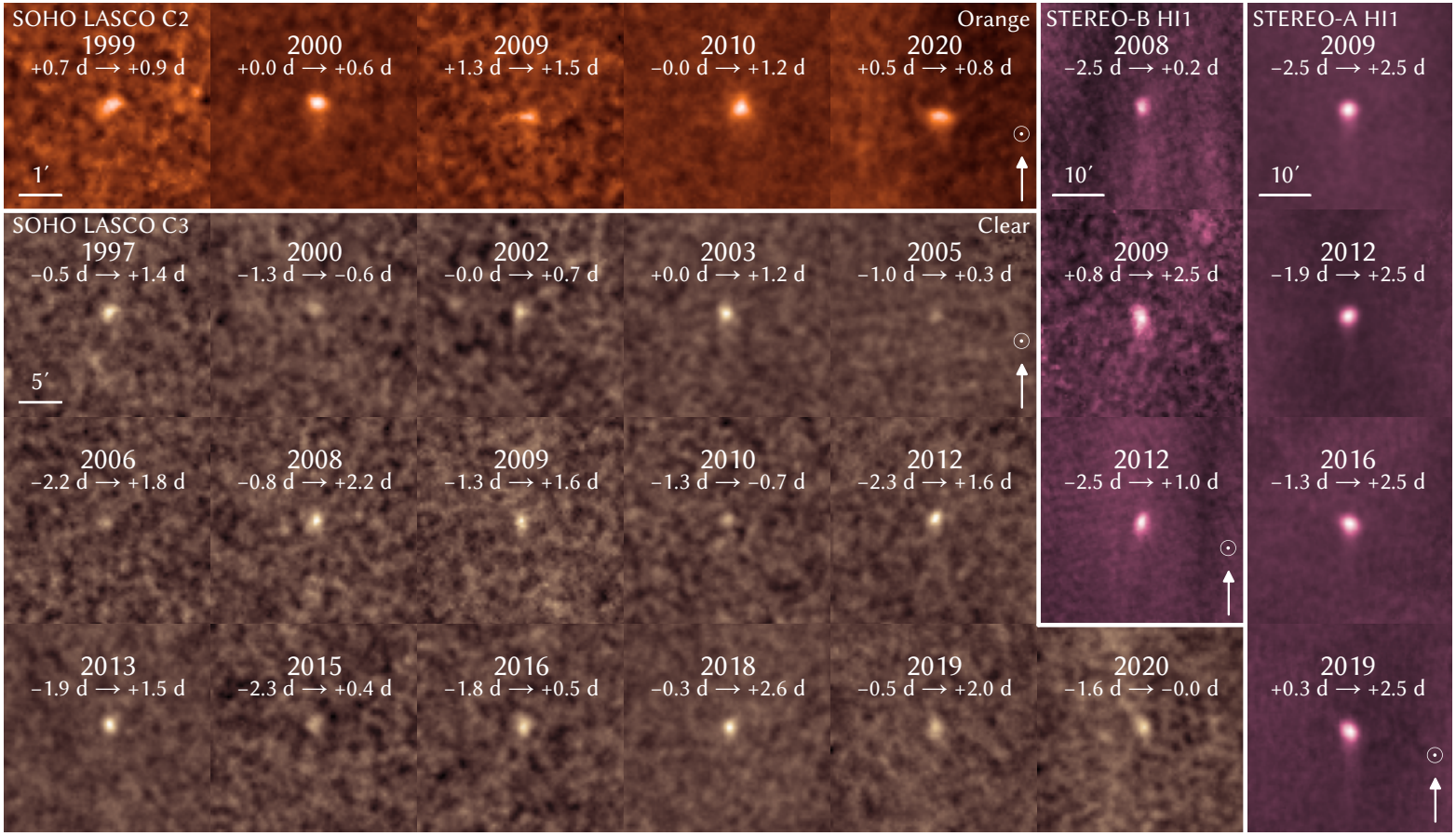

Figure 4.3: Phaethon's perihelion activity at all 17 apparitions between 1997 and 2020, as observed by SOHO LASCO C2/C3 and by both STEREO-A and STEREO-B HI1. Text labels in each image indicate the perihelion year of the respective apparition along with the time spanned by the image stack, given in days relative to the perihelion time. The sunward direction is oriented upward in all frames.

brightness contribution of its Na I activity.

4.3 Analysis

The fluorescence rate of each Na I atom varies as a function of not only heliocentric distance r, but also radial velocity $\dot{r}$ under the Swings effect (Swings 1941) due to the influence of deep Na I D Fraunhofer absorption lines in the solar spectrum, which drives resonance fluorescence. The actual tail brightness is further strongly modified by the Greenstein effect (Greenstein 1958) of the significant variation in r and $\dot{r}$ of Na I along the tail. In Appendix 4.6.4, we detail a model to compute the brightness profiles of predominantly optically thin Na I tails encompassing these effects together with Na I photoionization as functions of asteroid r and $\dot{r}$. In this section, we apply this model to Phaethon to demonstrate that its observed morphology and photometry are both consistent with Na I activity.

4.3.1 Morphology

One distinctive aspect of Phaethon's activity noticed by Jewitt et al. (2013) and Hui & Li (2017) is its antisunward tail, which seems to lengthen over the course of ~1 day after perihelion, which both studies interpreted as micron-sized dust taking ~1 day to be accelerated by radiation pressure into a tail. Part of this arises from Phaethon's activity being overall much brighter post-perihelion, and a brightening tail rising above the noise level could appear to be lengthening. However, the Na I tail model expects a physical lengthening of the tail over this period as a consequence of the Greenstein effect.

Na I atoms ejected from Phaethon prior to perihelion, when Phaethon itself has $\dot{r} < 0$, will initially largely also have $\dot{r} < 0$, but are accelerated by radiation pressure toward $\dot{r} \sim 0$. At $\dot{r} = 0$, the Na I D lines coincide with the Na I D absorption lines in the solar spectrum driving the fluorescence, which reduces the excitation rate and thus the acceleration of atoms. The lowered acceleration then slows their escape to $\dot{r} > 0$, trapping them in this weakly fluorescing state for a prolonged period, suppressing the tail. In contrast, Na I atoms ejected after perihelion, when Phaethon has $\dot{r} < 0$, will largely have initial $\dot{r} > 0$ which the positive acceleration only further increases, resulting in a bright tail of efficiently fluorescing Na I rapidly accelerating antisunward. Mercury's Na I tail behaves similarly by this mechanism, appearing considerably brighter after perihelion (Schmidt et al. 2010b).

Figure 4.4 illustrates the modeled lengthening of Phaethon's tail over the days surrounding perihelion. It also demonstrates from stacking pre- and post-perihelion

data from similarly high phase angles α—where Phaethon's activity outshines its surface, as discussed in Section 4.3.2—to similar signal-to-noise ratios (S/N) that the brightness of the tail relative to the head is indeed higher post-perihelion than pre-perihelion.

We also performed syndyne analysis of Phaethon's tail in the 2022 C2 Orange stack, taking advantage of its high $\alpha \approx 166°$ that exaggerates the small deviations in tail direction from antisunward indistinguishable by earlier analyses of HI1 observations at lower α (Hui & Li 2017; Jewitt et al. 2013). Due to Phaethon's orbit around the Sun, the otherwise convenient, sunward-aligned frame is actually a rotating reference frame, so Na I or dust initially accelerating antisunward will follow curved trajectories in this frame due to Coriolis acceleration, with slower particles exhibiting greater curvature. Finson & Probstein (1968) defines a parameter β as the ratio between the radiation pressure acceleration and solar gravity, which is nearly constant for dust grains of a given size. As sunlight is predominantly comprised of photons with a wavelength on the order of $\sim$1 μm, micron-sized grains have the highest scattering efficiency and thus the highest $\beta \sim 1$ (Gustafson et al. 2001; Kimura 2017) corresponding to the least curved dust trajectories. Na I atoms, however, have much higher $\beta \sim$ 7–75, depending on $\dot{r}$, and so will form a tail that is much less curved than any dust tail. As Figure 4.4 shows, the curvature of the observed tail appears consistent with Na I, but excludes $\beta = 1$ dust.

Note that this tail morphology also excludes atomic oxygen (O I)—which is both abundant in meteoritic material (Lodders 2021) and often observed as a dissociation product of cometary volatiles (Decock et al. 2013)—from responsibility for the observed flux. While its forbidden 557.7 nm, 630.0, and 636.4 nm [O I] lines do fall within the Orange and outside the Blue filter bandpasses like Na I D emission, O I cannot form a tail resolvable by our data: These weak [O I] lines support minimal momentum transfer from sunlight corresponding to only $\beta \sim 4 \times 10^{-5}$ (Fulle et al. 2007), sufficient to propel the atoms antisunward by just $\sim$10–40 km, or $\sim$0.001 px in the 2022 LASCO C2 frames, over their $\sim$0.5–1 d photoionization lifetime at $r \approx 0.14$ au (Fulle et al. 2007; Huebner & Mukherjee 2015). We are furthermore unaware of any plausible, unseen parent compounds with $\beta \gg 1$ that could have distributed O I along the observed tail prior to dissociation, or any alternative candidate species that could plausibly match both the tail morphology and Blue–Orange contrast expected for Na I.

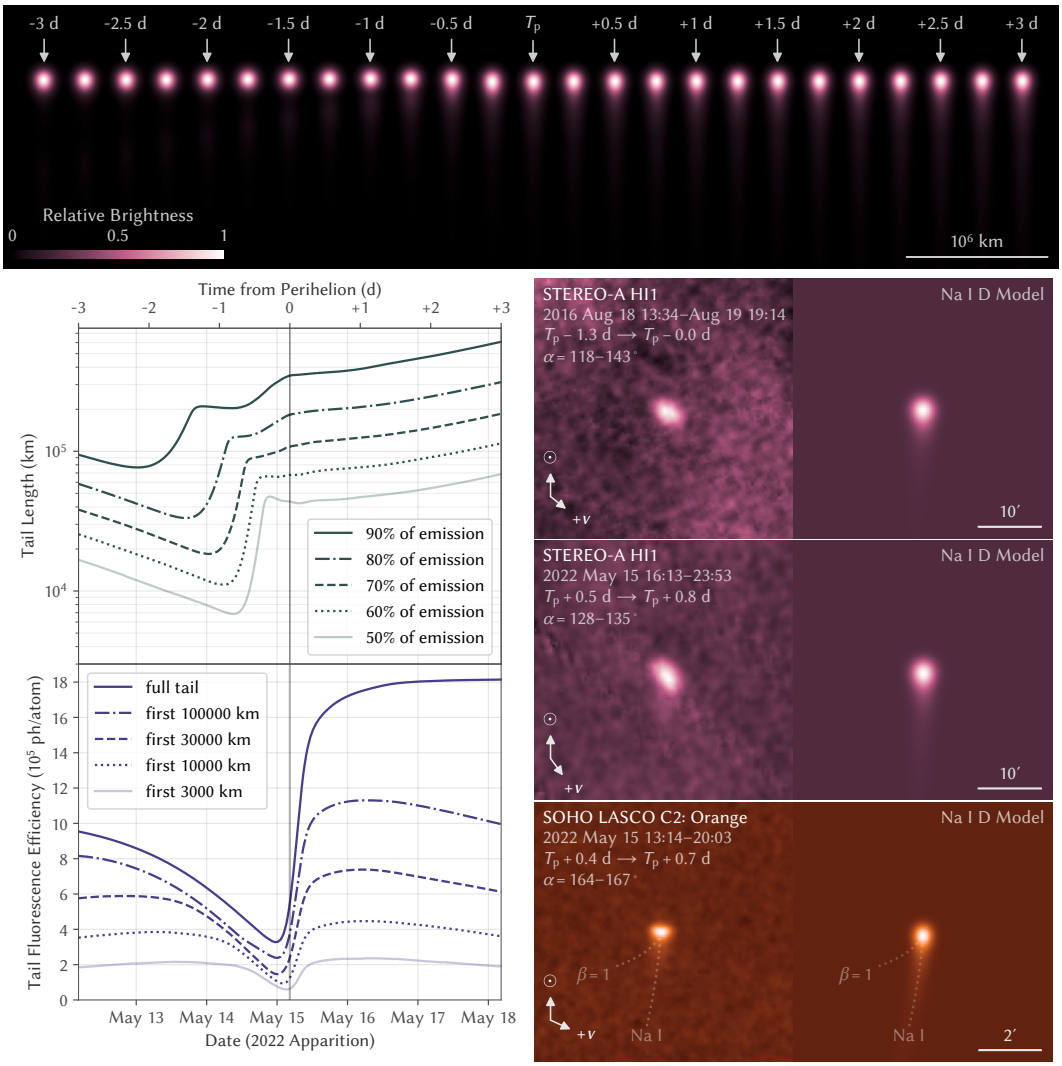

Figure 4.4: *Top:* Visualization of the modeled Na I D tail brightness profile from 3 days before to 3 days after perihelion (T_p), smoothed to a FWHM of 250,000 km to approximate the HI1 appearance at $\alpha \sim 90°$, and normalized to the brightness of the head to illustrate the increasing brightness of the tail relative to the head following perihelion. *Lower left:* Evolution in the lengths of tail containing 50–90% of the total Na I D emission, and the effective fluorescence efficiency of the first 3000–100,000 km of the tail and that of the full tail—defined as the mean number of Na I D photons emitted per atom while within that section of tail, or equivalently, the total Na I D photon emission rate from that tail section divided by the Na I production rate. *Lower right:* Comparison of Phaethon's observed and modeled Na I D morphology in HI1 under similar observing geometry and stacked to similar S/N in 2016 before perihelion and in 2022 after perihelion, as well as in LASCO C2 at higher α and resolution in 2022 after perihelion. Models use symmetric 3′ (HI1) and 30″ (C2) FWHM PSFs to approximate the actual, slightly trailed PSFs. Dotted curves in the C2 panel trace the expected positions of a tail of $\beta = 1$ (micron-sized) dust and one of Na I, demonstrating that the observed tail is compatible only with the latter.

4.3.2 Photometry

The other major distinctive aspect of Phaethon's activity is its asymmetric light curve that consistently rises sharply at perihelion into a peak ~0.5 days later, before fading and vanishing days later. To explore this behavior, we constructed light curves by first dividing the data into bins spanning a certain time interval, and performing a median stack of each bin to improve resistance to cosmic rays and other artifacts. For our primary science data, we used bin sizes varying from 45 min for the 2022 C2 Orange data, which had the highest S/N, to 6 h for C3 Clear data, with the lowest S/N. We measured photometry from each stacked frame within apertures of radii $\rho = 45''$ in C2, $\rho = 2'$ in C3, and $\rho = 3'$ in HI1, which were selected to maximize S/N to point sources while ensuring robustness to typical errors in the astrometric solutions of each camera. These apertures were accompanied by background annuli with $2\rho/3\rho$ inner/outer radii, which were sufficiently large to have minimal tail contamination. We then convolved each frame with the photometric aperture and used the standard deviation within the background aperture as the measurement uncertainty.

Before analyzing the activity, the flux from Phaethon's surface must be subtracted from the photometry. We measured this brightness directly by performing photometry of a separate copy of the HI1 data with ~2 day time bins, then fitted an $H = 14.33 \pm 0.10$, $G_{12} = 0.76 \pm 0.29$ model (Muinonen et al. 2010) through only the points at $r > 0.2$ au well beyond where activity has previously been reported, which we presume to capture only the inactive solid surface (as validated retrospectively by the Na I production model we fit in Section 4.3.2.1). Spectra show that Phaethon has a slightly blue optical color, with reflectance differing by $\lesssim$10% between HI1 and the C2 and C3 bandpasses used (Binzel et al. 2001; de León et al. 2010). We consider this difference inconsequential for our purposes, and used this same fitted HG_{12} model to subtract the surface contribution from the rest of our photometry, and thus isolate the brightness of the activity alone. Additionally, while the HG_{12} model may not properly capture the fading of the surface at high $\alpha \gtrsim 100°$, the minimal surface contribution to overall brightness at these α becomes dwarfed by the phase-independent activity brightness, and so contributes minimal error to the measured activity brightness. Figure 4.5 shows the result, normalized for observer distance, which reaffirms the initial finding that Phaethon's activity appears much brighter through Orange than any other filter.

Next, we used the Na I tail model to translate the fluxes measured within the different photometric apertures to the Na I emission rate of the full tail, as well as

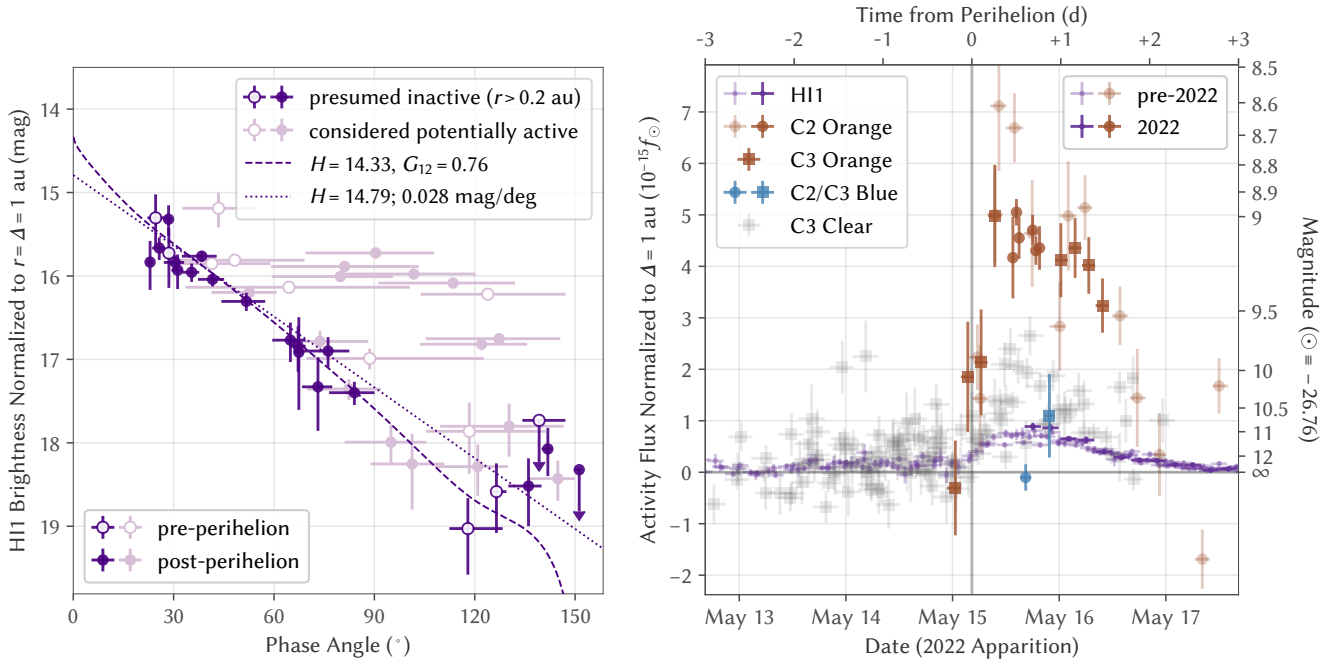

Figure 4.5: *Left:* Phase angle dependence of Phaethon's r- and Δ-normalized HI1 brightness. Excluding all bins extending to $r < 0.2$ au isolates measurements presumed to be free of activity to yield our $H = 14.33 \pm 0.10$, $G_{12} = 0.76 \pm 0.29$ surface reflection model, with a linear fit shown for comparison. *Right:* Surface-subtracted flux from all 18 apparitions, normalized to $\Delta = 1$ au, expressed relative to the mean solar flux through each bandpass ($f_\odot$). Dark/light symbols for C2 Orange and HI1 highlight observations from 2022/earlier apparitions. Note that these fluxes are measured within differently sized apertures of 45″ radius for C2, 2′ for C3, and 3′ for HI1, so the plotted flux differences correspond only approximately to physical colors. Vertical error bars indicate $\pm 1\sigma$, upper limits indicate $+3\sigma$, and horizontal error bars indicate the full range of the observations contributing to each point for both of these and all following plots.

the corresponding Na I production rate $Q(\text{Na I})$. The results in Figure 4.7 show the Orange/Clear/HI1 emission and production rate curves to essentially coincide, demonstrating the associated colors remain consistent with those expected for Na I D by the calibrations.

Moreover, unlike the light curves and Na I D emission rates, the $Q(\text{Na I})$ actually appears nearly symmetric about perihelion. The same Greenstein effect that suppresses the pre-perihelion length of the tail by the feedback effect described in Section 4.3.1 likewise suppresses the total brightness of the pre-perihelion tail. The pre-perihelion Na I atoms spending a prolonged time with low fluorescence efficiency trapped at $\dot{r} \sim 0$ will emit fewer Na I D photons before photoionizing than post-perihelion atoms, which remain at $\dot{r} > 0$ with high fluorescence efficiencies throughout their lifetime. The sudden brightness surge at perihelion therefore reflects not a surge in Phaethon's actual activity, but one in the overall fluorescence efficiency of Phaethon's Na I tail, a quantity we define to be the total number of Na I D photons emitted per atom released into the tail—equivalent to the Na I D photon emission rate from the tail divided by $Q(\text{Na I})$—as plotted in Figure 4.4.

4.3.2.1 Sodium Production Fit

To quantify Phaethon's Na I production, we used a Markov-chain Monte Carlo (MCMC) process with our Na I tail model to fit the photometry. We used a functional form

$$Q(\text{Na I}) = Q_{\max} \times \left(\frac{q}{r_{\Delta t}}\right)^n \tag{4.1}$$

for the production rate $Q(\text{Na I})$ at a given time, where $r_{\Delta t}$ is the r of Phaethon at time Δt earlier. The $q = 0.140$ au is Phaethon's perihelion distance, while $Q_{\max}$, n, and Δt are fittable, physical parameters, with $Q_{\max}$ being the peak $Q(\text{Na I})$, n indicating the r^{-n} dependence of $Q(\text{Na I})$, and Δt being the offset of $Q(\text{Na I}) = Q_{\max}$ from perihelion. We used a log-uniform prior for $Q_{\max}$ and uniform priors for n and Δt.

We also included several extra parameters to capture systematic effects from imperfect calibrations, modeling, and data reduction. First, we added the $r = 1$ au Na I lifetime τ_{Na} (which scales to the actual Na I lifetime at r as $\tau_{\text{Na}} \times r^2$) as a free parameter with a log-uniform prior to capture the otherwise uncharacterized uncertainty associated with our chosen 7.59×10^{-6} s^{-1} photoionization rate at $r = 1$ au (Huebner & Mukherjee 2015), which actually differs from earlier values by several tens of

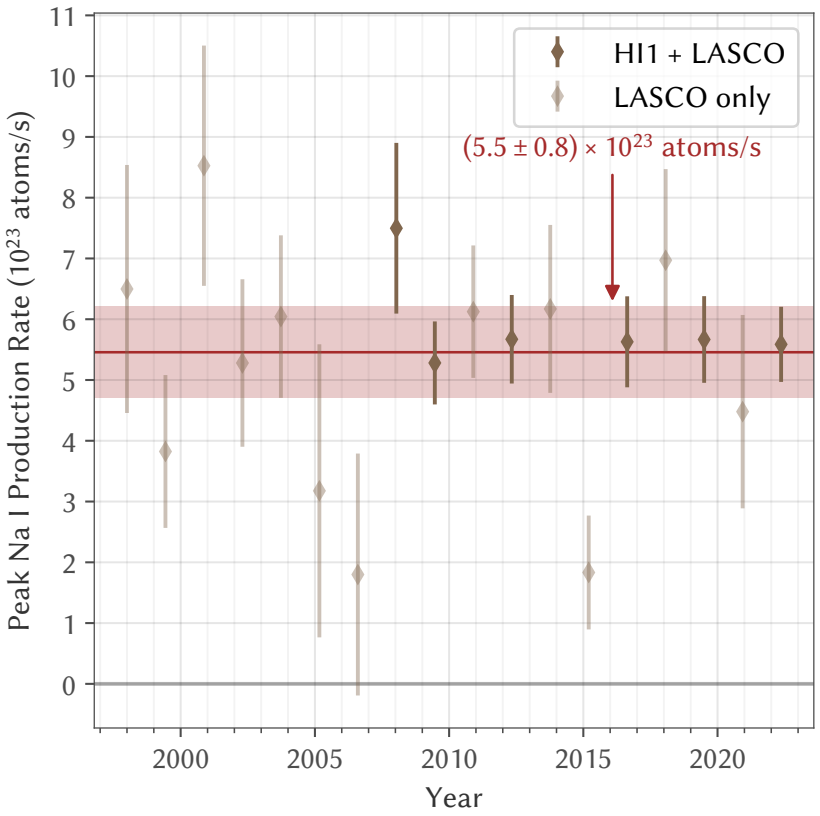

Figure 4.6: Peak Na I production rate $Q_{\max}$ at each apparition, fitted with all other parameters constrained to the results of the all-apparition fit. No trends appear evident, with the $Q_{\max}$ of individual apparitions generally consistent with the all-apparition fit of $(5.5 \pm 0.8) \times 10^{23}$ atoms s^{-1}.

percent (c.f., Fulle et al. 2007; Huebner et al. 1992). We also use this value to correct the HI1 Na I D sensitivity calibration from Appendix 4.6.1, which is sensitive to τ_{Na} through its reliance on the brightness of distant portions of Mercury's Na I tail.

We then introduced three parameters representing the offsets from the calibrated Orange, Orange–Clear difference, and HI1 magnitudes. Note that these offsets may not necessarily reflect only errors in the photometric calibrations, but could also capture errors in the modeled Na I tail profiles since Orange (mostly C2), Clear (C3), and HI1 observations tend to capture flux from different lengths of tail due to photometric aperture and field of view differences between the cameras. We used a normally distributed prior with mean 0 mag and standard deviation 0.2 mag for all three parameters as a crude, initial estimate for the absolute uncertainties of the calibrations.

We also introduced a variability parameter ξ prior to allow for underestimated uncer-

tainties or variability between apparitions, and an outlier parameter ϵ to minimize the potential for large outliers to skew the fit, with flat priors constrained to positive values for both. We incorporated these parameters by modeling the residual likelihood distribution for each observation with calculated uncertainty σ by a Voigt profile, the convolution of a normal distribution with standard deviation $\xi\sigma$ and a Cauchy–Lorentz distribution with scale parameter $\epsilon\sigma$.

We used emcee (Foreman-Mackey et al. 2013) to sample the posterior distribution with 100 walkers. Following standard procedures, we considered the sampling converged at 50 times the maximum autocorrelation time estimated for the parameters, disposed of initial samples totaling two times the maximum autocorrelation time, and thinned the remaining samples by half the minimum autocorrelation time to obtain the posterior samples. We provide the resulting mean ± 1σ values of all parameters from our fit to all 18 apparitions of Phaethon observations in Table 4.3, alongside those for equivalent fits to observations of 322P/SOHO and 323P/SOHO discussed in Section 4.4.

We overlaid the fitted $Q_{\max} = (5.5 \pm 0.8) \times 10^{23}$ atoms s^{-1}, $n = 13.7 \pm 0.5$, and $\Delta t = (+3.0 \pm 0.8)$ h model over the data in Figure 4.7, which demonstrates that it successfully reproduces the observed photometric behavior. Moreover, the fitted $\tau_{\mathrm{Na}} = (40 \pm 3)$ h (corresponding to an actual lifetime of (0.78 ± 0.06) h at $r = 0.14$ au) is comparable to the 37 h lifetime from the Huebner & Mukherjee (2015) Na I photoionization rate at $r = 1$ au, while the fitted color offsets are all <0.1 mag, further reinforcing that the observed brightening arises from Na I D emission. The $n = 13.7 \pm 0.5$ is far steeper than that expected from Na I production mechanisms like photon-stimulated desorption, solar wind ion sputtering, and meteoroid impact vaporization (Schmidt et al. 2012), but is consistent with the sharp temperature dependence expected of thermal desorption which we therefore consider to be principally responsible for the observed Na I activity. The small $\Delta t = (+3.0 \pm 0.8)$ h offset of peak Na I production from perihelion is comparable to Phaethon's 3.6 h rotation period (Hanuš et al. 2016), and appears consistent with thermal lag for Na I sourced from a depth on the order of ~0.1 m, roughly the diurnal thermal skin depth (Masiero et al. 2021).

We then explored the potential variability of Phaethon's activity between apparitions by repeating the MCMC sampling process for each individual apparition of Phaethon. We constrained these fits with a restrictive prior constructed from the all-apparition fitted posterior crudely approximated as a normal distribution with

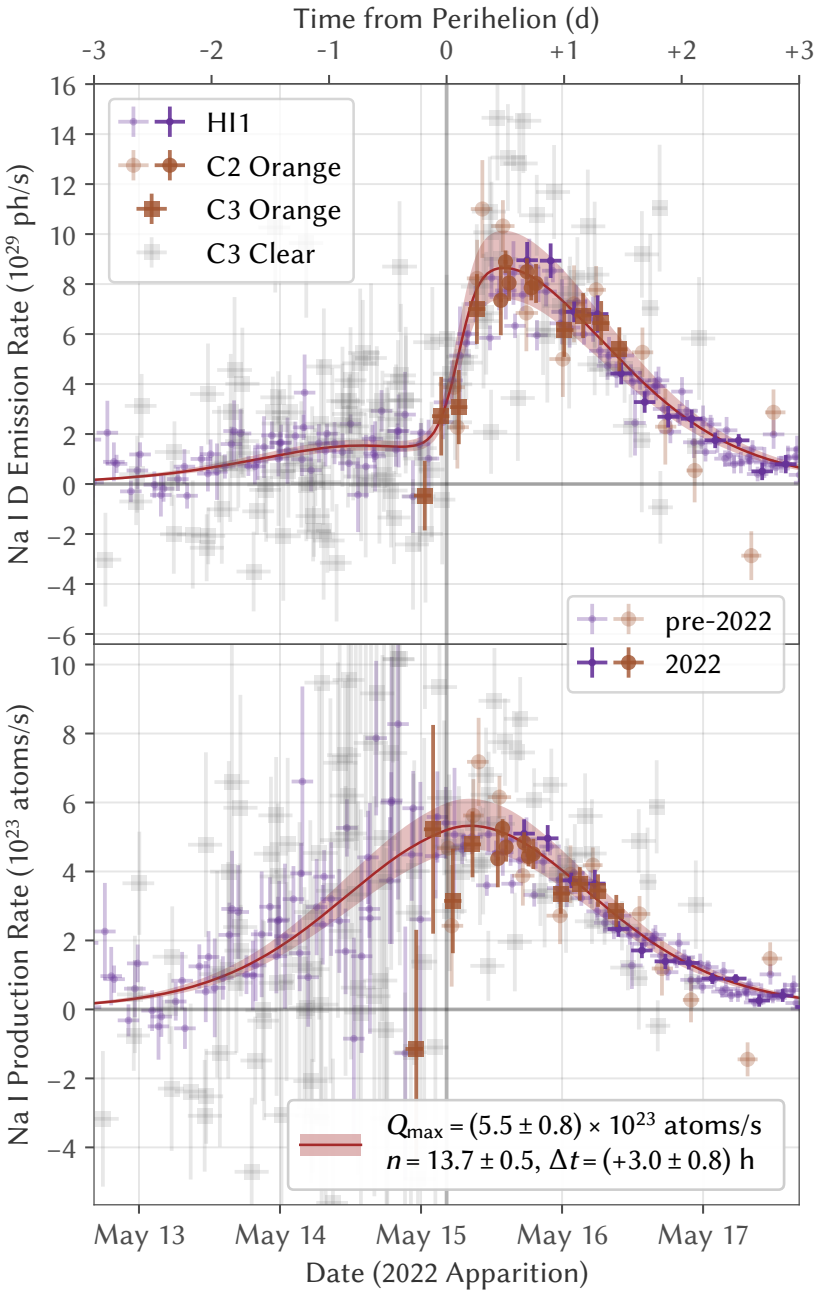

Figure 4.7: Total Na I D emission rate (top) and Na I production rate (bottom) from Phaethon near perihelion as measured by LASCO and HI1 over all 18 observed apparitions, with the fitted model shown in brown. Darker symbols, again, highlight observations from the 2022 apparition. While fitted by the model, offsets between the different bandpasses have not been corrected for these plotted points to visually demonstrate the close agreement between the observed colors and those expected for Na I D emission. We did, however, use the nominal, fitted $\tau_{Na} = 40$ h rather than the a priori 37 h to calibrate the plotted HI1 photometry, which amounted to a 13% difference in those points.

Table 4.3: Na I Model Parameters

Parameter	Units	(3200) Phaethon	322P/SOHO[a]	323P/SOHO[a]	Prior
perihelion distance[b], q	au	0.140	0.054	0.048	fixed
Fitted Parameters (Mean ± 1σ)					
peak Na I production rate[b], $Q_{\max}$	atoms s^{-1}	$(5.5 \pm 0.8) \times 10^{23}$	$(3.9 \pm 0.6) \times 10^{25}$	$(3.5 \pm 0.9) \times 10^{24}$	$Q_{\max}^{-1}$
slope of Na I production rate[b], n	–	13.7 ± 0.5	8.8 ± 0.3	9.8 ± 1.3	uniform
time offset of Na I peak[b], Δt	h	$+3.0 \pm 0.8$	-0.5 ± 0.2	-1.0 ± 0.5	uniform
Na I lifetime $\propto r^2$ at $r = 1$ au, $\tau_{\rm Na}$	h	40 ± 3	[41 ± 2][c]	[42 ± 3][c]	$\tau_{\rm Na}^{-1}$
Orange photometry offset from calibration	mag	$+0.01 \pm 0.16$	[−0.03 ± 0.10][c]	[−0.02 ± 0.16][c]	0 ± 0.2[d]
Clear–Orange offset from calibration	mag	-0.09 ± 0.06	[−0.11 ± 0.06][c]	[−0.08 ± 0.06][c]	0 ± 0.2[d]
HI1 photometry offset from calibration	mag	-0.00 ± 0.15	[−0.27 ± 0.12][c]	–	0 ± 0.2[d]
fractional photometric variability[e], ξ	–	0.08 ± 0.03	0.36 ± 0.03	0.32 ± 0.11	$\xi > 0$
relative outlier wing width[e], ϵ	–	0.10 ± 0.04	0.14 ± 0.06	0.20 ± 0.11	$\epsilon > 0$
Derived Properties (Mean ± 1σ)					
total Na I production, $\bar{Q}$	atoms orbit^{-1}	$(1.09 \pm 0.15) \times 10^{29}$	$(3.7 \pm 0.6) \times 10^{30}$	$(1.6 \pm 0.4) \times 10^{29}$	–
Clear photometry offset from calibration	mag	-0.08 ± 0.16	–	–	–
Orange–HI1 offset from calibration	mag	$+0.01 \pm 0.13$	–	–	–
Clear–HI1 offset from calibration	mag	-0.08 ± 0.13	–	–	–

[a]322P and 323P models may not accurately capture the physics of those comets as they exhibit systematic residuals to a much greater degree than the Phaethon model, so physical parameters likely have true errors far exceeding the computed uncertainties.

[b]$Q(\text{Na I}) = Q_{\max} \times (q/r_{\Delta t})^n$, where $r_{\Delta t}$ is r at time Δt earlier.

[c]Bracketed values were constrained with normally distributed priors with the mean ± 1σ of the values fitted for Phaethon, and so should not be used except as crude indicators of modeling error.

[d]Normally distributed priors with listed mean ± 1σ.

[e]Residual probability distribution for a point with formal uncertainty σ is modeled as a core normal distribution with standard deviation $\xi\sigma$ convolved with an outlier Cauchy–Lorentz distribution with scale parameter $\epsilon\sigma$.

independent parameters, except leaving $Q_{\max}$ unconstrained with a uniform prior. The resulting $Q_{\max}$ of individual apparitions plotted in Figure 4.6 show considerable scatter, but no clear trend. Note, in particular, the low scatter of apparitions with HI1 observations—especially after excluding 2008, where STEREO-B HI1 missed the post-perihelion peak—suggests the true variability in Phaethon's activity between apparitions is likely no more than a few percent over decade timescales.

4.4 Context

4.4.1 Sodium Volatility on Sunskirting Objects

Na I D emission has routinely been documented in the spectra of nearly all bright comets observed at $r \lesssim 0.6$ au since 1882 (e.g., Adel et al. 1937; Evans & Malville 1967; Huggins 1882; Newall 1910) and occasionally at even $r \sim 1$ au (Cremonese et al. 1997; Oppenheimer 1980). Analysis of the spatial and velocity profiles often show the Na I to originate both from an extended, coma source—likely dust grains—and directly from the nucleus itself (Brown et al. 1998; Combi et al. 1997; Schmidt et al. 2015).

In contrast, Na I D emission has never previously been reported from any formally designated asteroid, like Phaethon, on which classical cometary volatiles are assumed to be absent. However, Masiero et al. (2021) found that at the temperatures Phaethon experience at perihelion, the Na content of chondritic asteroidal material will volatilize and escape, which they propose could even drive comet-like dust production. With a fresh surface initially containing Na in metallic form at a roughly chondritic 0.5% abundance by mass, they estimated Phaethon could attain $Q_{\max} \sim 6 \times 10^{26}$ atoms s^{-1} near perihelion, or three orders of magnitude above the peak production rate we derive. This difference is not entirely surprising as Na will become increasingly depleted near the surface over repeated apparitions if not replenished, thus lowering the production rate over time. Most of the Na is also likely bonded within silicate materials rather than present in pure metallic form, which can change its thermal properties. The apparent depletion of Na in most Geminids meteoroids provides further evidence for such Na volatilization near Phaethon's orbit (Abe et al. 2020).

4.4.1.1 322P/SOHO and 323P/SOHO

Many of SOHO's sunskirting comets may also be asteroids whose Na content has been volatilized by their proximity to the Sun. Two of these, 322P/SOHO

and 323P/SOHO, have been recovered by nighttime telescopes as inactive nuclei at $r \sim 1$ au where classical comets driven by water ice sublimation are active (Hui et al. 2022; Knight et al. 2016). Both nuclei also exhibited asteroid-like characteristics, being much smaller in size, displaying bluer colors, and at least 322P featuring a much higher albedo than typical cometary nuclei. Like Phaethon, these comets exhibit a strongly orange photometric color while active with little phase angle dependence, indicative of Na I D emission with a lack of the micron-sized dust grains typically characteristic of active comets, but approach the Sun to a much closer $q \sim 0.05$ au than Phaethon (Knight et al. 2010; Llebaria et al. 2006).

LASCO has observed six apparitions each of 322P and 323P since 1999. We reduced the photometry of all apparitions in the same manner as for Phaethon, and plot the resulting Na I D emission rates in Figure 4.8. Both 322P and 323P appear much brighter than Phaethon, by ~4 mag and ~2 mag, respectively. They also vary in brightness between apparitions to a much greater degree, with 322P fluctuating by a factor of two and 323P by several times. Much of the variability of 323P arises from its highly erratic orbit, which brought its perihelion distance from $q = 0.052$ au in 1999 to $q = 0.048$ au for 2004, 2008, and 2012, then down to $q = 0.039$ au for 2016 and 2021; isolating the 2004–2012 apparitions reduces the variability to the photometric noise level.

We then fit this data with the same MCMC procedure as described for Phaethon in Section 4.3.2.1, except with τ_{Na} and the color offsets constrained by priors of normal distributions with the mean $\pm$ 1σ of the values fitted for Phaethon. Results are again presented in Table 4.3. Note, however, that neither comet's light curve appears as well fit by this Na I model: While they share the qualitative similarity of a pre-perihelion plateau in brightness followed by a sharp increase to a post-perihelion peak, the model overestimates the sharpness of the peak as well as the degree of pre/post-perihelion asymmetry for both comets. Therefore, one or more of the model assumptions must break down for these comets and the fitted parameters, provided in Table 4.3, should be treated as only rough estimates. Likely sources of error include significant contributions to Na I production from extended sources like an unseen dust tail as well as optical depth modeling limitations at the much higher Q(Na I) of these comets.

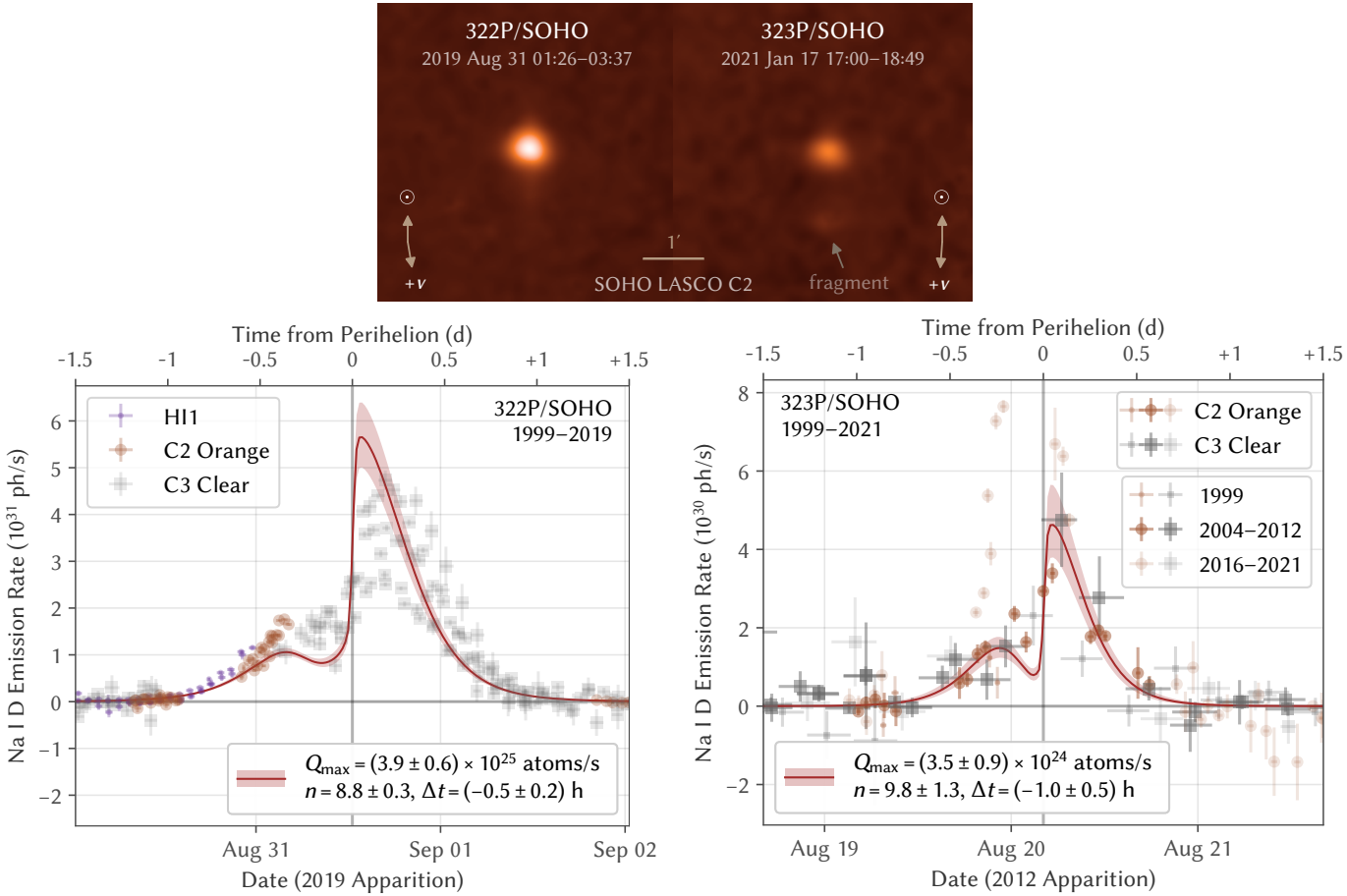

Figure 4.8: *Top:* 322P/SOHO and 323P/SOHO seen by LASCO C2 during their latest apparitions. Note the presence of a fragment leading 323P/SOHO by ∼1′. *Bottom:* Na I D emission rates for 322P/323P, with models fitted to all apparitions of 322P, and to the 2004–2012 apparitions of 323P while its orbit had q = 0.048 au. These models do not fit the observations as well as the one for Phaethon, possibly due to some combination of spatially extended Na I production and optical depths higher than those valid for the approximations used.

4.4.1.2 Less Active Sunskirting Asteroids

A number of formally designated asteroids approach the Sun more closely than Phaethon, yet none have ever been seen to be active (Holt et al. 2022). All are much smaller than Phaethon, but several are still sufficiently large for observable activity if they had surfaces of comparable volatility. We selected favorable apparitions for a trio of asteroids with $q < 0.1$ au: (137924) 2000 BD_{19} in 2018, (374158) 2004 UL in 2009, and (394130) 2006 HY_{51} in 2014. In each case, the asteroid crossed the LASCO C2 field of view at high phase angles immediately after perihelion, when Na I tail fluorescence was most efficient. We processed all C2 Orange frames in the same manner as done for Phaethon, but were unable to detect any of the asteroids in the combined stacks.

Table 4.4 provides the 3σ upper limits for the asteroid trio—all $\sim 10^{23}$ atoms s^{-1}—in comparison to the fitted Na I production rates for Phaethon, 322P, and 323P. We then approximately normalize the production rates for surface area by dividing by $10^{-0.4H}$, a quantity proportional to the geometric albedo times the cross sectional area, where the geometric albedo of all six objects likely all fall within a few factors of Phaethon's 11% (MacLennan et al. 2022). The results plotted in Figure 4.9 illustrate that the 3σ upper limits on normalized Na I production by the asteroid trio cannot exclude a value comparable to that measured for Phaethon at its perihelion. However, these limits constrain the Na I production of the asteroid trio closer to the Sun than Phaethon ever reaches, and Phaethon's extremely steep $n = 13.7 \pm 0.5$ activity fall-off suggests its Na I production would likely be much higher at those distances as well, complicating the comparison.

Appendix 4.6.3 presents a rudimentary thermal desorption model for an isothermal blackbody asteroid to extrapolate Phaethon's Na I to lower r for this comparison. The steep $n = 13.7 \pm 0.5$ appears inconsistent with the sublimation of metallic Na, but is well-modeled if the Na sequestered beyond $\sim$0.1 m below the surface had a modified $L = (1.8 \pm 0.2)$ eV $atom^{-1}$ = (170 ± 20) kJ mol^{-1}. This derived L agrees well with the empirically determined $\sim$1.8 eV $atom^{-1}$ average binding energy for desorption of Na bound to oxide surfaces (Madey et al. 1998). This value also falls within the 100–400 kJ mol^{-1} range previously measured for Kreutz sungrazing comets (Sekanina 2003), which may share a similar mechanism for Na I activity.

We overlay both the metallic Na and modified L extrapolations of Phaethon's normalized Na I production to lower r in Figure 4.9. 322P falls very near the modified L extrapolation, especially considering the additional uncharacterized uncertainties

Table 4.4: Na I Production by Sunskirting Asteroids & Comets

Name	H (mag)[a]	Observation Period (UT)	r (au)[b]	Q(Na I) (atoms s^{-1})[c]
(3200) Phaethon	14.33 ± 0.06[d]	1997–2022	0.140	$(5.5 \pm 0.9) \times 10^{23}$
322P/SOHO	20.19[e]	1999–2019	0.054	$(3.9 \pm 1.5) \times 10^{25}$
323P/SOHO	21.49 ± 0.08[f]	2004–2012	0.048	$(3.5 \pm 1.5) \times 10^{24}$
(137924) 2000 BD_{19}	17.47[g]	2018 Jul 25–26	0.092–0.095	$<8 \times 10^{22}$
(374158) 2004 UL	18.72[g]	2009 Apr 12	0.093–0.099	$<9 \times 10^{22}$
(394130) 2006 HY_{51}	17.24[g]	2014 Nov 22	0.083–0.099	$<1.0 \times 10^{23}$

[a]Absolute magnitude, transformed to V assuming solar color.

[b]Heliocentric distance corresponding to provided Q(Na I); equal to perihelion distance q for Phaethon/322P/323P.

[c]Na I production rate at r. Uncertainties for Phaethon/322P/323P aim to capture variability and systematic fitting error, and are computed as $(\sigma(Q_{\max})^2 + (\xi Q_{\max})^2)^{1/2}$, where $\sigma(Q_{\max})$ is the 1σ fit uncertainty of $Q_{\max}$. Upper limits are 3σ.

[d]From HG_{12} fit in Figure 4.5.

[e]From HG_1G_2 fit by Knight et al. (2016).

[f]From HG_{12} fit by Hui et al. (2022).

[g]From H, $G = 0.15$ fit by the Minor Planet Center.

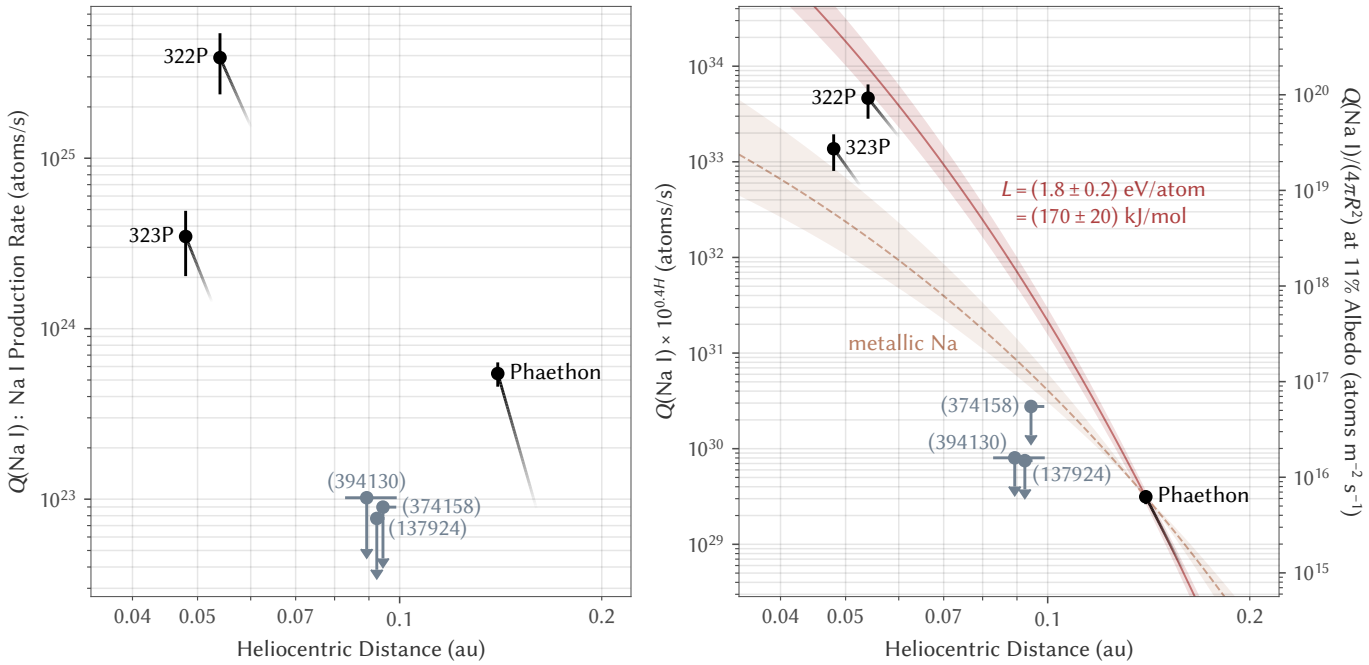

Figure 4.9: *Left:* Na I production of Phaethon, 322P, and 323P at perihelion with mean slopes indicated by a faded line, as well as the 3σ upper limits for the asteroids (137924), (174158), and (394130). *Right:* Na I production multiplied by $10^{0.4H}$ (proportional to Na I production per unit reflection cross section) for the same objects. The $n = 13.7 \pm 0.5$ of Phaethon's activity is considerably steeper than expected for sublimation of metallic Na, and instead implies a modified latent heat of $L = (1.8 \pm 0.2)$ eV atom^{-1} = (170 ± 20) kJ mol^{-1}. The uncertainties illustrated for the metallic Na and modified L extrapolations reflect uncertainties in Phaethon's Na I production rate and subsurface temperature, as elaborated in Appendix 4.6.3.

arising from thermal model simplifications, albedo differences, and the systematic errors in 322P's Na I production model. In contrast, 323P falls an order of magnitude below the modified L extrapolation, while the $+3\sigma$ limits for the asteroid trio fall 1–2 orders of magnitude below. The latter limits fall below even the shallower metallic Na extrapolation.

This initial comparison appears to show 322P's surface to be comparably volatile to Phaethon's surface, 323P's to be modestly less so, while those of (137924), (374158), and (394130) have become more deeply devolatilized. We therefore conclude that Phaethon's Na I activity near perihelion, while not unique, is still unusual as it is not broadly shared among the overall population of sunskirting asteroids, so proximity to the Sun alone cannot explain its presently high surface volatility compared to other asteroids with comparable or lower q.

4.4.2 Sodium-Driven Mass Loss Potential

In the Whipple (1951) gas drag model, dust grains can be ejected from the surface when the outward gas drag they experience there exceeds the gravity holding them down. Phaethon's current $Q(\text{Na I}) = (5.5 \pm 0.8) \times 10^{23}$ atoms s^{-1} near perihelion produces an average gas flux of $\sim 2 \times 10^{16}$ atoms m^{-2} s^{-1} over the $\sim 4\pi \times (5.4\text{ km}/2)^2$ surface area. With Phaethon near equinox at perihelion (Masiero et al. 2021), solar heating should be fairly well-distributed over most of its surface and theoretically can support nearly isotropic subsurface Na desorption with minimal day–night variation. In practice, surface variations may effect significant local variations in Na I flux, and we crudely estimate the peak Na I flux at $\sim 10^{17}$ atoms m^{-2} s^{-1}.

With a thermal Na I outflow speed of ~ 1 km s^{-1}, the peak drag force on a dust grain of radius R_g with a drag coefficient on the order of unity is $\sim 10^{-12}\text{ N} \times (R_g/1\text{ mm})^2$. Estimates for the true density of both Geminid meteoroids and Phaethon vary widely, but assuming a typical bulk density of ~ 2.6 g cm^{-3} for dust grains (Borovička et al. 2010) and ~ 1.6 g cm^{-3} for the bulk asteroid itself, the surface gravity of $\sim 10^{-3}$ m s^{-2} exerts a force of $\sim 10^{-7}\text{ N} \times (R_g/1\text{ mm})^3$ on the grains, exceeding the drag force for all except very small grains of $R_g \lesssim 1$ μm. While we technically cannot observationally constrain the abundance of submicron, Rayleigh scattering grains which rapidly drop in mass-normalized scattering efficiency $\propto R_g$, we placed tight bounds on the presence of micron-sized grains in Section 4.2.2.1, so consider Phaethon's current Na I activity as unlikely to be driving significant dust production—at least on its own.

Phaethon, however, is also rotating with a rapid 3.6 h period near the critical limit, producing an equatorial centrifugal acceleration $\sim 10^{-3}$ m s^{-2} that nearly entirely offsets the gravitational acceleration in those regions. Nakano & Hirabayashi (2020) proposed that Phaethon's rotation was recently even faster and above the critical limit, which would have allowed it to shed dust grains and even boulders with no size limit. If Phaethon's effective surface gravity remains below ~1% of its non-rotating value anywhere on the surface, the observed Na I activity could then lift $R_g \sim 0.1$ mm grains from those areas which our high phase angle observations do not usefully constrain. However, such activity might be accompanied by purely rotationally driven mass loss from areas with slightly centrifugal acceleration that then exceeds the gravity, and the much greater efficiency of this process would likely marginalize the contribution of Na I gas drag to dust production.

Na I production could also theoretically alter Phaethon's rotation to indirectly drive mass loss through rotational instability, analogous to how the sublimation of icy volatiles visibly torque and disrupt comet nuclei (e.g., Bodewits et al. 2018). Marshall et al. (2022) recently reported Phaethon's rotational period to be decreasing at 4 ms yr^{-1}, or a rotational acceleration of 2.1×10^{-5} deg day^{-2}. However, Na I appears to again contribute incidentally at best: under the most favorable setup of Na I coherently directed along the equator, the observed, orbitally averaged Na I production $\bar{Q} = (1.09 \pm 0.15) \times 10^{29}$ atoms orbit^{-1} would torque Phaethon by ~200 N m. Even then, this maximum torque would rotationally accelerate Phaethon—treated as a uniform sphere—by only $\sim 2 \times 10^{-7}$ deg day^{-2}. More conventional thermal torque amplified by Phaethon's high surface temperatures and temperature gradients at perihelion may be a more plausible culprit in this case (e.g., Vokrouhlickỳ et al. 2015), but will require more detailed modeling to verify.

4.4.3 Sodium as a Tracer for Mass Loss

Regardless of its actual contribution to driving further mass loss, Na I activity may still serve as an useful indicator for mass loss from any mechanism. Phaethon's current Na I production depletes the ~0.5% by mass of Na from $\sim 10^6$ kg orbit^{-1} of chondritic material (Lodders 2021), representing the mass loss required per orbit to sustain the Na I production in steady state. This amount far exceeds the $\lesssim 10^3$ kg of micron-sized dust ejected near perihelion, as found in Section 4.2.2.1—ruling out such dust as a major source of Na I—but remains well below the $\gtrsim 10^{10}$ kg orbit^{-1} needed to sustain the Geminids stream (Jewitt & Li 2010). The true dust production may be much lower or entirely absent, as Phaethon's Na I activity is not necessarily

in steady state.

In the absence of unseen dust production clearing away devolatilized material covering Phaethon's surface, the devolatilized layer will gradually deepen and increasingly suppress the Na I production rate over time. Measuring the Na abundance near the surface by comparing the Na I production with that expected for a fresh surface can therefore, at least in theory, provide an estimate for when the surface was last cleared. In Appendix 4.6.3, we use our simple Na desorption model with crudely estimated surface characteristics to find that Phaethon's current ~0.1 m layer of devolatilized material suppresses its Na I production by a factor of $\sim 10^{-3}$, corresponding to a surface devolatilized over $\lesssim 10^4$ yr. This current bound is not yet particularly useful at constraining mass loss, as dynamical simulations indicate Phaethon has likely only spent a cumulative ~10 kyr within at least the last 100 kyr with $q \lesssim 0.15$ au where solar heating at perihelion is comparable to at present (MacLennan et al. 2021), so the visible Na I activity could, in theory, reflect only the brevity of Phaethon's sunskirting history.

However, the Geminids meteoroid stream did presumably form from Phaethon within the bounded time frame ~1–10 kyr ago (Ryabova 1999). Ejection of the stream's $\sim 10^{13}$ kg mass (Blaauw 2017)—a sizable fraction of Phaethon's own $\sim 10^{14}$ kg presently—was almost certainly associated with significant resurfacing of Phaethon that replenished its surface Na content from previously buried material. With better characterization of the surface material, and appropriate thermophysical and dynamical models, the observed Na I production can conceivable set more stringent timing constraints. In this way, Na I activity could serve as an observationally convenient, long-lasting record of significant mass loss in an asteroid's history even long after the mass loss event itself.

In Appendix 4.6.3, we calculate that Phaethon's Na I production depletes the equivalent of only a ~1 μm layer of subsurface material in a single apparition, explaining the lack of a discernible secular decline in Na I production over decade timescales over which the devolatilized layer deepens by only a minute fraction. The much stronger Na I activity of 322P and 323P, however, would deplete a more considerable ~1–10 cm of material per apparition. Sustaining this level of activity over the multiple observed apparitions likely requires the surfaces of both objects to be actively eroding at perihelion, presumably driven by their high Na I production and rapid rotation rates (Hui et al. 2022; Knight et al. 2016). Indeed, while 322P has never been observed away from the Sun after perihelion to ascertain its perihelic

dust production, Hui et al. (2022) found that 323P generated a debris field during its perihelion passage bright enough to be observed at $r \sim 1$ au. The active fragment we found in LASCO C2 data from the 2021 apparition (see Figure 4.8) further reinforces this finding.

At $q \sim 0.05$ au, both objects fall within the Granvik et al. (2016) limit for <1 km diameter asteroids to be thermally disrupted, so their ongoing erosion appears likely to end only with their destruction. Likewise, the $q = 0.08$–0.10 au of (137924), (374158), and (394130) place them beyond this zone, and their lack of observed Na I activity indicates an absence of significant mass loss in at least the last few centuries, assuming decay timescales longer than a few decades like that of Phaethon. Phaethon itself has remained at even higher $q > 0.1$ au over the past 100 kyr, reaching a minimum $q = 0.126$ au only recently, ~2 kyr ago (MacLennan et al. 2021; Williams & Wu 1993)—evidently too distant for mass loss to sustain itself and escalate into total disruption as 322P and 323P appear to be doing, given Phaethon's ongoing existence with minimal mass loss. Ye & Granvik (2019) suggested through meteoroid stream analysis that asteroids on Phaethon-like orbits may still undergo partial disruption by some thermally related mechanism at an average ~2 kyr cadence, but ultimately survive unlike objects much closer in.

While tempting to ascribe Phaethon's dramatically higher mass loss required during Geminids formation to increased solar heating at a slightly closer $q = 0.126$ au than the present $q = 0.140$ au, that difference alone would not obviously alter the key, qualitative characteristics of the Na I activity. Direct extrapolation of Phaethon's modern Na I production rate to $r = 0.126$ au yields a four-fold increase from its current perihelion rate to $Q(\text{Na I}) \sim 2 \times 10^{24}$ atoms s^{-1}, which leaves previous order of magnitude estimates derived from the modern Na I production substantially unchanged.

However, if the devolatilized layer were also much thinner or entirely absent, Na I production could have been up to six orders of magnitudes higher through two effects discussed in more detail in Appendix 4.6.3:

1. Removal of the ~0.1 m devolatilized layer serving as a diffusive barrier to Na I from below, increasing Na I production by up to a factor of $\sim 10^3$.
2. Na-bearing material exposed on the surface can reach subsolar temperatures of ~1000 K far above the ~700 K peak subsurface temperatures, which could raise overall Na I production by another factor of $\sim 10^3$.

Such an extremely high $Q(\text{Na I}) \sim 10^{30}$ atoms s^{-1} could potentially lift even meter-sized boulders without any rotational aid, but would require highly efficient surface clearing to sustain, as it would devolatilize a ∼10 m layer of material, or $\sim 10^{12}$ kg—approaching the $\sim 10^{13}$ kg of the entire Geminids stream—in one single apparition. Incomplete clearing of devolatilized surface material—particularly since only a fraction of the surface near the subsolar point can be maximally active at any time—would realistically lower this rate by one or more orders of magnitude, even if Phaethon were initially fully resurfaced in fresh, subsurface material.

Any such hypothetical elevation of Na I production, however, requires a resurfacing mechanism to initially clear the devolatilized layer over a sizable portion of the surface. A disruptive trigger event—for example, from rotational instability or a large impact exposing subsurface material—must necessarily have reset the surface volatility to initiate any Na-supported Geminids formation. The upcoming DESTINY$^+$ flyby mission aims to provide resolved imaging of Phaethon's surface which could yield clearer evidence for such phenomena (Arai et al. 2018; Ozaki et al. 2022).

4.4.3.1 Visibility of the Geminids Formation Process

The recency of the Geminids formation within the past few thousand years raises the intriguing, if remote, prospect of the event being seen and recorded by ancient sky watchers during this period. A $Q(\text{Na I}) \sim 10^{30}$ atoms s^{-1} is required for Phaethon to reach a magnitude of $V \sim -5$, necessary for naked eye observation in daylight at its $\lesssim 7°$ elongation at perihelion (Sekanina 2022). While pushing the theoretical upper limit for Na I thermally desorbed directly from the surface, such a rate could be readily attained through the accompanying dust production which provides a means to far more efficiently excavate Na, since dust grains may still retain a sizable fraction of their Na until after ejection, thus dramatically increasing the total exposed surface area.

One potential modern analog to Phaethon during Geminids formation is the sun-grazing comet C/2012 S1 (ISON), which brightened to $V \sim -3$ at $r \sim 0.1$ au (Knight & Battams 2014) roughly one week after its ∼1 km diameter nucleus (Lamy et al. 2014) apparently disintegrated (Sekanina & Kracht 2014). As illustrated in Figure 4.10, its intense brightness was confined almost exclusively to Na I D emission, which corresponded to $Q(\text{Na I}) \sim 10^{29}$ atoms s^{-1} that exceeded even its own $Q(H_2O) = (2.2 \pm 0.5) \times 10^{28}$ molecules s^{-1} at $r = 1.00$ au (Combi et al. 2014).

This Q(Na I) sustained over its ~1 day period of near-peak activity produced a total of $\sim 10^{34}$ atoms of Na I, corresponding to the Na content in $\sim 10^{11}$ kg of cometary material with a chondrite-like ~0.5% Na abundance by mass—comparable to the total mass of a ~1 km diameter nucleus with a typical cometary bulk density of ~0.6 g cm^{-3} (Weissman & Lowry 2008). C/2012 S1's extreme but otherwise asteroid-like behavior therefore involves the loss of a sizable fraction if not a majority of its original Na content, likely facilitated by its earlier disintegration into a field of debris much smaller than the original nucleus. Such debris would have been rapidly depleted of icy cometary volatiles much farther from the Sun—eliminating the source of classical cometary activity—but would have retained most of its more refractory Na content until reaching sunskirting distances where this Na could be impulsively released.

While C/2012 S1 was still too faint to be widely seen at its peak, the Geminids meteoroid stream has a combined mass on the order of $\sim 10^{13}$ kg that is $\sim 10^{2}\times$ larger (Blaauw 2017). The formation of the latter could therefore have involved considerably brighter events if a sizable fraction of the total mass was released in one or a few cataclysmic events. An ejection of $\sim 10^{12}$ kg of debris with a ~0.5% Na mass fraction contains $\sim 10^{35}$ atoms of Na which, when released over the span of one to a few days near perihelion, provides the requisite $\sim 10^{30}$ atoms s^{-1} for clear daylight visibility.

The likely absence of a prominent, cometary tail of micron-sized dust accompanying the bright Na I D emission would cause Phaethon and its debris to take a distinctly orange/red hue with nearly starlike naked eye morphology due to the short lifetime of Na I at its perihelion. Although not directly related to the formation of the Geminids, this description does notably fit reports of a daylight object seen briefly in 1921 at Lick Observatory and a few other sites (Pearce 1921; Sekanina & Kracht 2016), which may have been the Na I D emission of debris from another disrupted asteroid or comet. Reports of similar starlike objects beside the Sun also appear in Chinese records, although the credibility of most of these claims cannot be reliably established (Strom 2002). A more thorough investigation into potential observations of Phaethon, or lack thereof, during its formation of the Geminids could provide a unique source of direct observational constraints on the process.

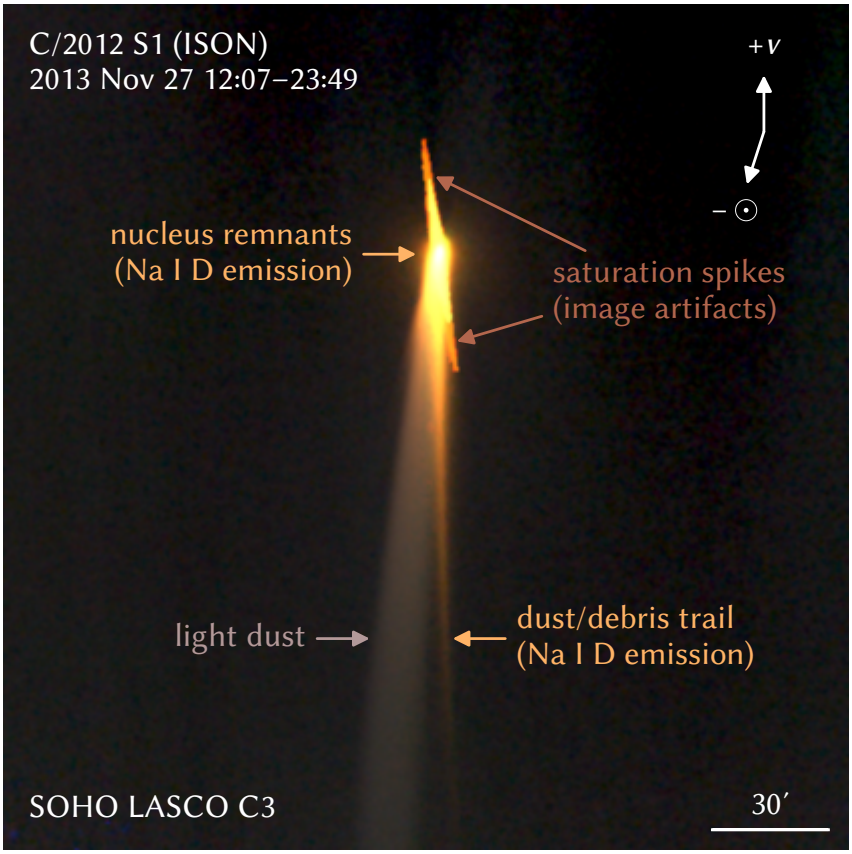

Figure 4.10: LASCO C3 color composite (RGB = Orange/Clear/Blue) of the disintegrating Oort Cloud comet C/2012 S1 (ISON) at r = 0.1 au, which may serve as a visual if not physical analog for a more active, Geminids-forming Phaethon. Bright Na I D emission, which appears with a golden hue in this image, highlights the remnants of the nucleus and a heavy ($\gtrsim$millimeter-sized) dust/debris trail. As with Phaethon's observed activity, this Na I D emission far outshines the sunlight scattered by light (micron-sized) dust grains that typically dominates the optical brightness of active comets at similar r.

4.5 Conclusions

We observed the perihelic brightening of sunskirting asteroid and Geminids parent (3200) Phaethon with the SOHO LASCO coronagraphs and the STEREO HI1 imagers over a total of 18 apparitions. We used three distinct lines of evidence to demonstrate that this brightening is from Na I D emission rather than dust:

1. Photometric colors: Phaethon's activity appears much brighter in Orange-filtered LASCO images than in Clear-filtered LASCO or HI1 images, and cannot be seen at all in Blue-filtered LASCO images. The measured colors match those expected for pure Na I D emission by our calibrations.

2. Tail morphology: Phaethon's tail grows in length and intensity from before to after perihelion as expected from effects of radiation pressure, Doppler shift, and solar Fraunhofer lines for a tail of Na I. The tail's curvature also appears consistent with Na I and inconsistent with dust.

3. Light curve pattern: Phaethon's brightness is sharply asymmetric about perihelion, being much greater after than before perihelion, which is again well-modeled by a tail of Na I with nearly symmetric Na I production. The fitted Na I lifetime of (40 ± 3) h at $r = 1$ au is likewise consistent with its photoionization under solar radiation.

We then analyzed the Na I production of Phaethon, compared it to those of other sunskirting comets and asteroids, and drew several key conclusions and inferences:

1. Phaethon attains a consistent peak Na I production rate of $(5.5 \pm 0.8) \times 10^{23}$ atoms s^{-1} at (3.0 ± 0.9) h after perihelion, with a steep heliocentric distance dependence of $r^{-13.7 \pm 0.5}$.

2. The total $(1.09 \pm 0.15) \times 10^{29}$ atoms $orbit^{-1}$ corresponds to the depletion of Na from $\sim 10^6$ kg $orbit^{-1}$ of chondritic material, although Phaethon's actual ongoing mass loss may be much lower as Na I activity is not necessarily sustained in steady state and could instead be decaying over timescales longer than a few decades.

3. Phaethon's Na I activity is likely driven by thermal desorption of Na, which is bound with an effective latent heat of (1.8 ± 0.2) eV $atom^{-1}$ = (170 ± 20) kJ mol^{-1} and sequestered beneath an effective ~0.1 m deep devolatilized layer.

4. Sunskirting comets 322P/SOHO and 323P/SOHO are likely asteroids experiencing high levels of heating at $r \sim 0.05$ au sufficient to actively erode their surfaces, which clears away Na-depleted material to sustain their strong Na I activity.

5. No activity was seen from sunskirting asteroids (137924), (374158), and (394130), indicating they exhibit much lower surface volatility than Phaethon, and likely have not experienced significant mass loss within the last few centuries. Sublimation-driven mass loss at their $r \sim 0.1$ au, alone, does not

appear capable of clearing Na-depleted material at a rate sufficient to sustain Na I production indefinitely.

6. While Na I gas drag could potentially drive further mass loss itself, Na I production and thus Na I D emission will accompany mass loss exposing fresh, subsurface material by any mechanism. Phaethon was likely much brighter from such emission during the Geminids formation period due to efficient excavation of subsurface Na, potentially even briefly to the point of daylight visibility.

Future investigations extending our findings with more sophisticated thermophysical and dynamical modeling of Phaethon and the Geminids stream may provide more detailed insight into the mechanics of Phaethon's Na I activity and its role, if any, in the still enigmatic Geminids formation process.

4.6 Appendix

4.6.1 HI1 Sodium Sensitivity

Like Phaethon, Mercury has also been known to generate a tail of Na I accelerated by radiation pressure, albeit with atoms likely sourced from predominantly non-thermal processes (Potter et al. 2002). Following reports of this tail's unexpectedly high brightness in HI1 imagery under the preflight transmission profiles (Schmidt et al. 2010a), Halain (2012) retested the HI1 engineering qualification model in 2010 and found that the filter bandpass had not only degraded from aging since the initial measurements in 2005, but was also affected by vacuum and the low operational temperatures. These effects combined to produce a net ~20 nm blueward shift in the filter transmission that still left the 589.0/589.6 nm Na I D lines just beyond the new ~595–720 nm FWHM interval, but substantially raised their relative transmission by an order of magnitude from 1–2% to ~15% that is sufficient to attribute the observed brightness of Mercury's tail to Na I D emission alone. The next brightest species seen in Mercury's tail at optical wavelengths is K I (Lierle et al. 2022), but its equivalent 766.5/769.9 nm resonance lines have <1% relative transmission through HI1, while K I is produced at only ~1% the rate of Na I and photoionizes more rapidly (Huebner & Mukherjee 2015), so negligibly contributes to the tail's brightness in HI1 imagery.

Both of the STEREO HI instruments have high precision, time-dependent photometric calibrations available for broadband source photometry derived by monitoring a

sample of stars over the course of the mission (Tappin et al. 2017, 2022). These calibrations, however, are only minimally sensitive to the exact transmission profiles. As the Na I D lines fall near the edge of the HI1 bandpass, HI1's sensitivity to them is strongly dependent on the precise bandpass shift and could theoretically vary substantially over the mission lifetime. We therefore opted to perform a separate calibration of HI1's sensitivity to pure Na I D emission using Mercury's tail as a flux standard.

Schmidt et al. (2010b) measured Mercury's Na I escape rate to be $Q(\text{Na I}) = 1.26 \times 10^{24}$ atoms s^{-1} at a true anomaly of $\theta = 68°$ near the seasonal peak in radiation pressure and $Q(\text{Na I}) \approx 5 \times 10^{23}$ atoms s^{-1} at $\theta \approx 115°$ using a similar tail model as the one we describe in Appendix 4.6.4 and used for Phaethon. We assume the tail brightness at these θ remains similar at every orbit, and select the HI1 data near these θ for flux calibration. However, light scattered by Mercury's bright, daylit surface introduces diffraction and saturation artifacts in HI1 imagery that complicates measurements of the comparatively faint Na I tail. We limited our analysis to epochs where Mercury is observed at high phase angles $\alpha > 145°$ to minimize the light from the daylit surface and simultaneously maximize the observed Na I column density, as the tail is projected nearly along the line of sight in this geometry.

We selected seven epochs from 2007 to 2021 that met our criteria for analysis, as listed in Table 4.5. At each epoch, we stacked all frames from a 2–3 day period, and show a cutout of the tail at every epoch in Figure 4.11. We then extracted the linear brightness profile of the tail out to 1° using 8′ wide rectangular photometric apertures extending from Mercury in the antisunward direction, and using the 8′ on both sides of this tail region for background determination. We excluded the innermost 10′ of the tail, where artifacts associated with light from the surface are noticeable. Next, we used a quadratic polynomial fit of Schmidt et al. (2010b)'s Na I escape rates with respect to θ to determine the expected $Q(\text{Na I})$ at each epoch, which we estimated as being ±10% from the true value. We then computed the expected Na I D tail profiles with our Na I tail model, and fitted them with the observed tail profiles to determine the Na I D sensitivity of the instruments.

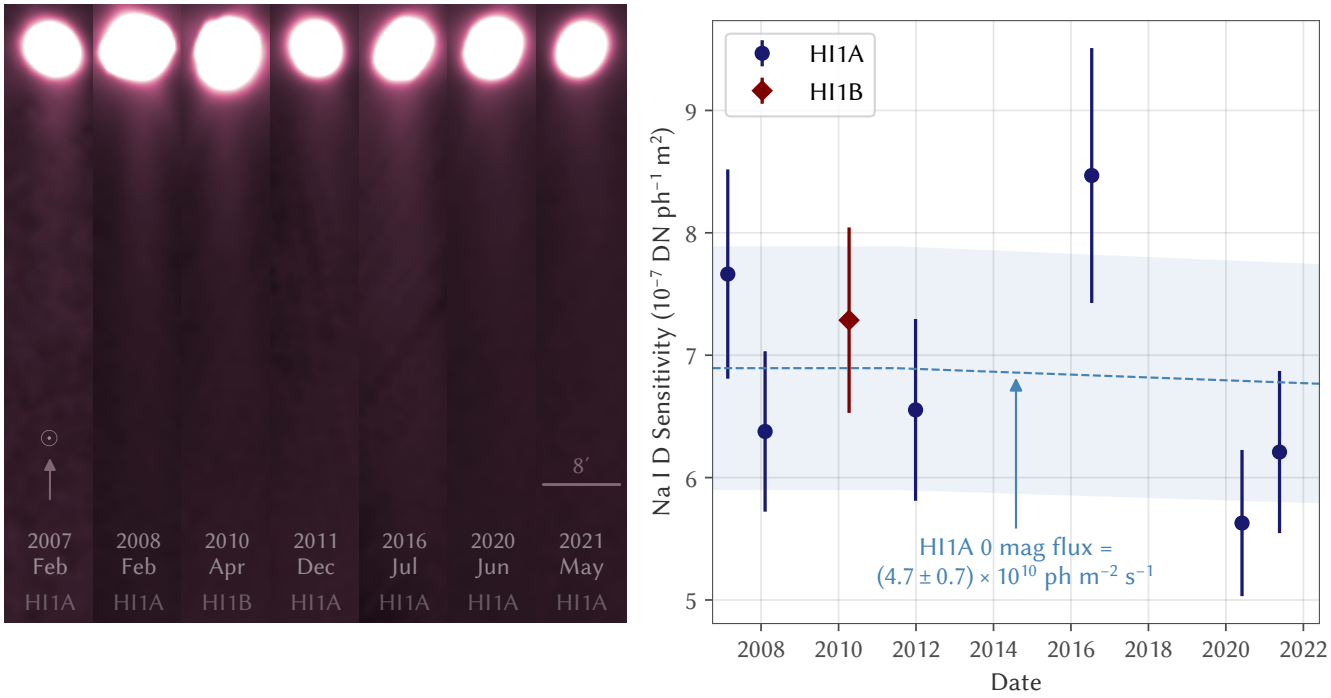

Figure 4.11: *Left:* Mercury and its Na I tail seen by the HI1 cameras of STEREO-A (HI1A) and STEREO-B (HI1B) at 7 epochs. The Na I tail extends downward (antisunward) from Mercury in all frames; the diagonal branches extending from Mercury in the 2008 and 2010 frames are saturation artifacts, while diagonal stripes along the tail are residual star trails from imperfect background subtraction. *Right:* HI1 sensitivity to Na I D photons, as measured by the fitted brightness of Mercury's tail at each epoch. The computed 0 mag flux of $(4.7 \pm 0.7) \times 10^{10}$ ph m^{-2} s^{-1} (equivalent to a $V = 0$ Na I D source magnitude of $+0.89 \pm 0.16$) under the Tappin et al. (2022) HI1A broadband photometric calibration is indicated by the dotted line and shaded region. The uncertainties in these values were generously estimated by the scatter of the HI1A points, allowing for potentially correlated measurement errors comparable to this scatter. Note that Na I D sensitivity varies with the assumed $r = 1$ au ionization rate, with the values in this plot computed for an assumed rate of 7.59×10^{-6} s^{-1} (Huebner & Mukherjee 2015).

We provide the computed sensitivities for a nominal $r = 1$ au Na I photoionization rate of 7.59×10^{-6} s^{-1} (Huebner & Mukherjee 2015) in Table 4.5 and plot them in Figure 4.11. Our measurements appear consistent with a fixed 0 mag flux of $(4.7 \pm 0.7) \times 10^{10}$ ph m^{-2} s^{-1} over the full 2007–2021 calibration period for STEREO-A HI1. The single measurement for STEREO-B HI1 in 2010 suggests this camera has comparable Na I sensitivity. This result indicates the shift in bandpass had likely already completed by the commencement of STEREO mission operations, so we consider the relative Na I D sensitivity to be constant over the operating lifetimes of both cameras.

Additionally, all of our tail brightness measurements are weighted toward distant portions of Mercury's tail where the fraction of surviving Na I and thus the relative brightness of the tail are sensitive to the assumed Na I lifetime. Earlier estimates by Huebner et al. (1992) and Fulle et al. (2007) differ from our nominal value by tens of percent, which would shift the calibrated Na I D sensitivity beyond our stated uncertainties. Figure 4.12 shows the variation in the STEREO-A HI1 Na I D calibration across a range of assumed Na I lifetime, which we incorporated as an Na I lifetime-dependent calibration into our photometric model to address this concern.

The final fit to Phaethon's photometry in Section 4.3.2.1 provided an equivalent $r = 1$ au Na I lifetime of (40 ± 3) h, corresponding to a photoionization rate of $(7.0 \pm 0.6) \times 10^{-6}$ s^{-1} that is close to the selected Huebner & Mukherjee (2015) value. This retrospective analysis scales the 0 mag flux to $(5.3 \pm 0.7) \times 10^{10}$ ph m^{-2} s^{-1}, which remains consistent with the a priori value.

4.6.2 LASCO Photometric Calibration

We consider LASCO observations spanning its multi-decade lifetime, over which variations in detector sensitivity could significantly affect photometry. Existing calibrations of both LASCO C2 (Colaninno & Howard 2015; Gardès et al. 2013; Llebaria et al. 2006) and C3 (Thernisien et al. 2006) cover only a small fraction of the mission lifetime and/or do not calibrate filters used by our observations. We therefore opted to perform a photometric calibration encompassing the entire time period to ensure the validity of our photometry.

By convention, SOHO and STEREO zero-point magnitudes are set to provide the Johnson V magnitudes of solar-colored stars, which defines a magnitude system where the mean magnitude of the Sun from 1 au is -26.76 in all bandpasses

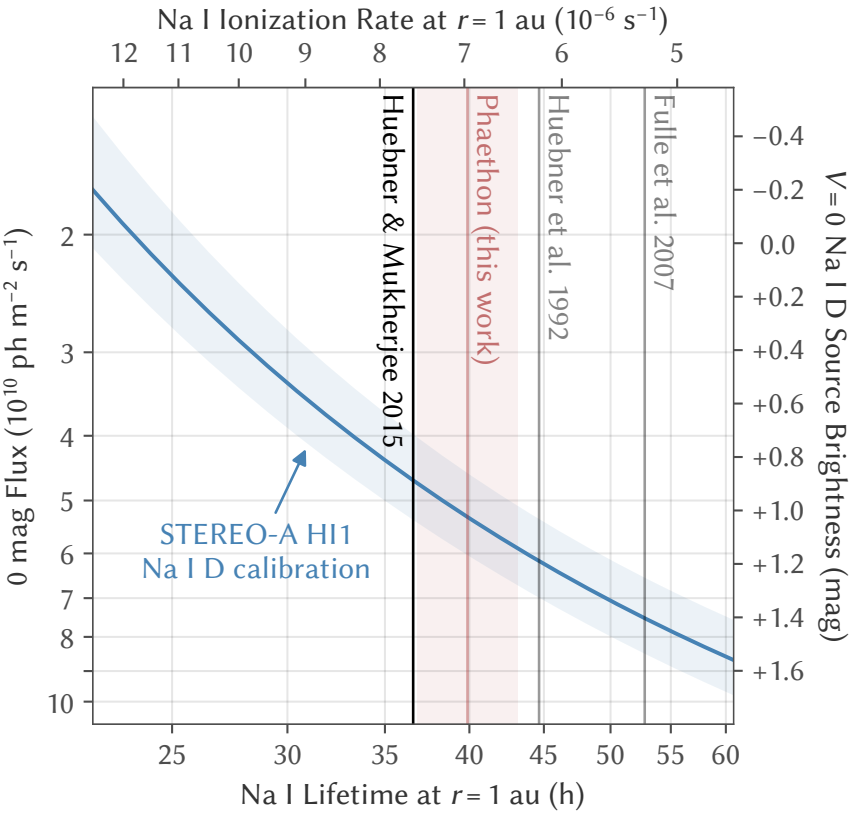

Figure 4.12: Variation of the STEREO-A HI1 Na I D calibration with assumed Na I lifetime at $r = 1$ au (with $\propto r^2$ scaling). Values from Huebner & Mukherjee (2015, quiet and active Sun mean; selected as our nominal a priori value), Huebner et al. (1992, quiet and active Sun mean), and Fulle et al. (2007) are indicated by their labeled vertical lines. We also indicate the $r = 1$ au equivalent (40 ± 3) h lifetime from our Phaethon photometric fit, for comparison.

Table 4.5: Observations of Mercury's Tail Used for Na I D Sensitivity Calibration

Instrument	Observation Time (UT)	α (°)[a]	θ (°)[b]	Q(Na I) (atoms s^{-1})[c]	Na I D Sensitivity (DN ph^{-1} m^2)[d]	0 mag Flux (ph m^{-2} s^{-1})[d,e]
STEREO-A HI1	2007 Feb 20–21	158–166	62–70	1.25×10^{24}	$(7.7 \pm 0.9) \times 10^{-7}$	$(4.2 \pm 0.5) \times 10^{10}$
STEREO-A HI1	2008 Feb 07–08	147–158	61–71	1.25×10^{24}	$(6.4 \pm 0.7) \times 10^{-7}$	$(5.0 \pm 0.5) \times 10^{10}$
STEREO-B HI1	2010 Apr 09–10	148–159	62–73	1.25×10^{24}	$(7.3 \pm 0.8) \times 10^{-7}$	$(4.3 \pm 0.4) \times 10^{10}$
STEREO-A HI1	2011 Dec 27–28	158–166	112–119	6.3×10^{23}	$(6.6 \pm 0.7) \times 10^{-7}$	$(4.9 \pm 0.6) \times 10^{10}$
STEREO-A HI1	2016 Jul 14–15	155–164	68–76	1.24×10^{24}	$(8.5 \pm 1.0) \times 10^{-7}$	$(3.8 \pm 0.5) \times 10^{10}$
STEREO-A HI1	2020 May 30–Jun 02	152–167	105–120	7.1×10^{23}	$(5.6 \pm 0.6) \times 10^{-7}$	$(5.6 \pm 0.6) \times 10^{10}$
STEREO-A HI1	2021 May 20–21	159–167	116–123	5.3×10^{23}	$(6.2 \pm 0.7) \times 10^{-7}$	$(5.1 \pm 0.5) \times 10^{10}$

[a]Phase angle of Mercury from observing spacecraft.

[b]True anomaly of Mercury.

[c]Estimated Na I escape rate with assumed ±10% uncertainty, fitted from observations by Schmidt et al. (2010b).

[d]For $r = 1$ au equivalent Na I ionization rate of 7.59×10^{-6} s^{-1} (Huebner & Mukherjee 2015).

[e]Na I D flux producing magnitude 0 under the Tappin et al. (2022) HI1A and Tappin et al. (2017) HI1B calibrations.

(Willmer 2018). We based our calibration on a single, high quality flux standard star to minimize complications with variability and color transformations. We chose to use 39 Tau due to its brightness ($V = 5.90$), its minimal (<0.1 mag) variability (Gaia Collaboration et al. 2022), its nearly solar optical colors (Farnham et al. 2000), and its proximity to the ecliptic plane that causes it to transit both the C2 and C3 fields of view over several days each May.

We processed all frames containing 39 Tau over 1996–2022 in the same manner as the science data, producing a yearly median stack for every filter with at least three frames present, and performing aperture photometry within a 45″ radius for C2 and a 2′ radius for C3. Under the synoptic programs in which these data were collected, only C2 Orange and C3 Clear frames are collected at full resolution, with all other frames recorded with 2×2 binning yielding a slightly larger effective PSF. To mitigate this effect, we corrected the measured fluxes to larger apertures of 2′ in C2 and 5′ in C3, which we treat as equivalent to an infinite aperture fully capturing the flux of a point source. We measured the C2 PSF from 39 Tau itself and found a minimal correction factor of 1.01× regardless of binning. However, we measured the C3 PSF from the neighboring star 37 Tau due to the presence of a $V = 8$ star ∼3′ northeast of 39 Tau that prevents the use of apertures much larger than our 2′ radius, and found correction factors of 1.1× for unbinned frames and 1.3× for 2×2 binned frames.

Figure 4.13 plots these resulting zero-points which are generally consistent with the previously published calibrations over their respective time periods, along with a gradual sensitivity decline of (-2.6 ± 0.6) mmag yr^{-1} in C2 Orange and (-1.8 ± 0.4) mmag yr^{-1} in C3 Clear, which we adopt as the rates for all C2 and C3 bandpasses, respectively. For comparison, Llebaria et al. (2006) measured −8 mmag yr^{-1} for C2 Orange over 1996–2004, and Thernisien et al. (2006) measured (-4.8 ± 1.1) mmag yr^{-1} for C3 Clear over 1996–2003. A subsequent recalibration of C2 Orange by Gardès et al. (2013) measured −3.8 mmag yr^{-1} over 1999–2009, while Colaninno & Howard (2015) measured (-2.2 ± 0.3) mmag yr^{-1} over 1996–2013, the latter comparable to our 1996–2022 result.

Unlike HI1, LASCO cannot readily detect Mercury's Na I tail due to its lower instrumental sensitivities and the brighter coronal background within its fields of view. However, none of the LASCO filters have a bandpass cut-on or -off near the Na I D lines, so minor shifts in bandpass like those of HI1 will not significantly alter the Na I D sensitivity. The preflight filter transmission profiles show that only

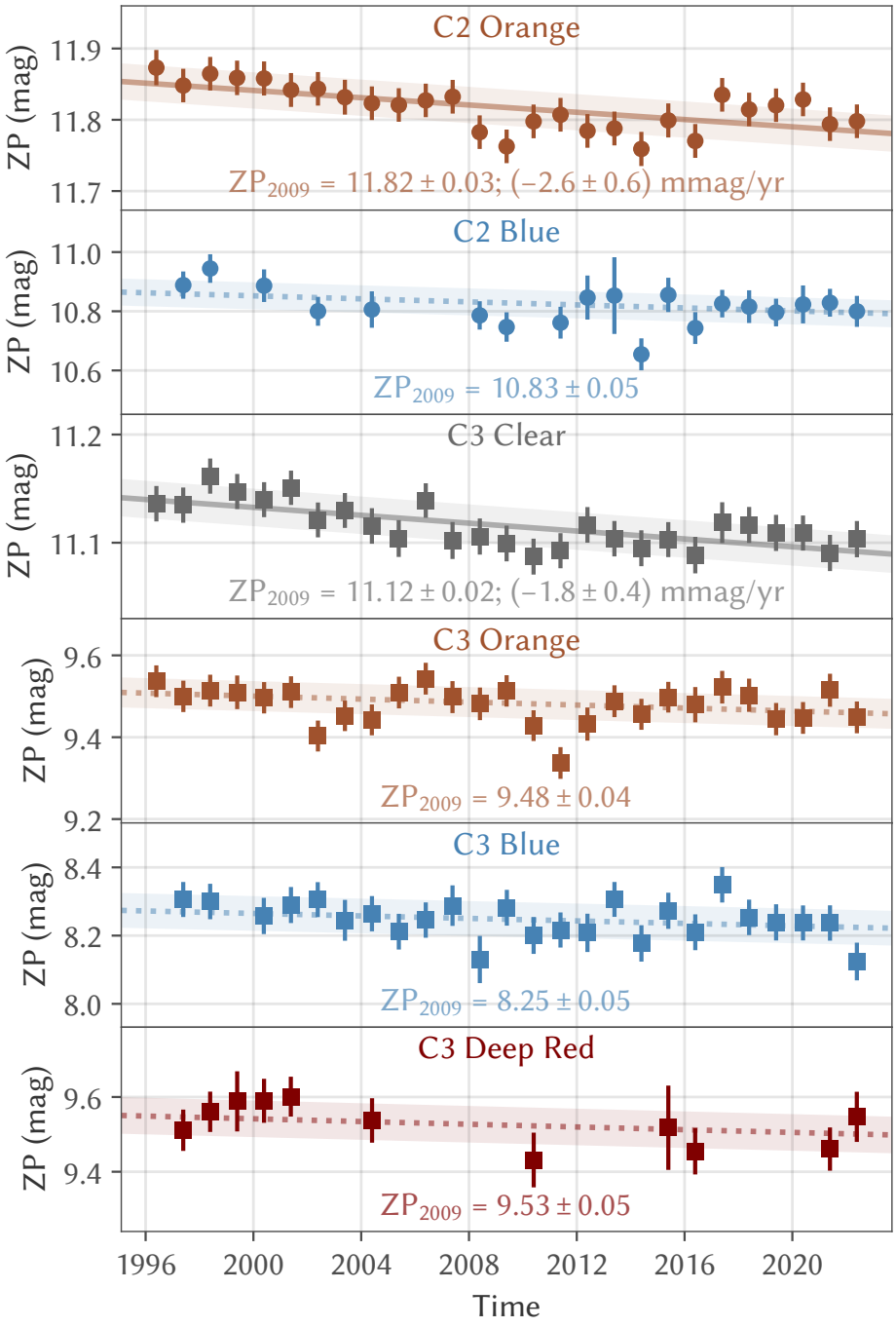

Figure 4.13: LASCO C2 and C3 zero-point (ZP) magnitudes derived from 39 Tau. The lines and associated shading indicate linear fits to the zero-points, with the slopes in all C2 and C3 assumed to match the fitted slopes of C2 Orange and C3 Clear, respectively.

C2 Orange, the nearly identical C3 Orange, and C3 Clear transmit Na I D emission, with 589 nm near the peak transmission of all three filters.

However, the cut-on wavelength of C3 Clear is below 500 nm where no transmission or detector quantum efficiency (QE) data appear to be available for C3. Given the similarities of the C2 and C3 detectors and their measured >500 nm QE profiles, we use the C2 detector QE as that of the C3 detector below 500 nm, and use the mean 500–510 nm transmission of C3 Clear filter as its assumed transmission at <500 nm to obtain an initial estimate for the full C3 Clear bandpass.

This estimated C3 Clear bandpass is 5.5× more sensitive to a solar-colored source than C3 Orange, corresponding to a 1.86 mag higher zero-point magnitude for C3 Clear. However, the measured zero-point of C3 Clear is only (1.64 ± 0.05) mag higher than that of C3 Orange, or ∼4.5× greater solar sensitivity in the former. Even 0% transmission below 500 nm yields too high of a solar sensitivity, suggesting the transmission longward and/or shortward of the Orange bandpass interval is lower than predicted from preflight transmission and QE alone, possibly from the LASCO optics. The precise profile, however, is not required for quantifying Na I D sensitivity. We assume the central portion of the Clear profile—including the Orange bandpass interval—remains fixed, then compensate for the (0.22±0.05) mag discrepancy in zero-point color by contracting the effective Clear bandpass by (18 ± 4)% (i.e., lowering the Clear sensitivity anywhere outside the Orange bandpass interval to reach the observed zero-point color).

Na I D emission with a Johnson V magnitude of 0 would appear as magnitude +0.39 ± 0.05 in this corrected C3 Clear bandpass, or ∼1.3 mag fainter than the −0.94 expected for the C2 and C3 Orange bandpasses. Table 4.6 provides the final solar and Na I D photometric calibration parameters for LASCO C2/C3, as well as the HI1 Na I D sensitivity obtained in Appendix 4.6.1 for comparison. We also include a posteriori values for Na I D calibration parameters, which have been corrected for the Na I lifetime and color offsets fitted from Phaethon's photometry in Section 4.3.2.1, although all values remain consistent with the a priori calibration.

4.6.3 Thermal Desorption of Sodium

In order to extrapolate Phaethon's Na I production to $r < 0.14$ au for comparison with 322P, 323P, and other sunskirting asteroids, we consider a rudimentary sublimation model for a fast rotating, isothermal blackbody asteroid following the approaches of Huebner (1970), Sekanina (2003), and Cranmer (2016). From the Clausius–

Table 4.6: SOHO LASCO/STEREO HI1 Bandpass Photometric Properties

Bandpass		Photometric Zero-point[a]		Na I D Calibration			
				A Priori[b]		A Posterori[c]	
Instrument	Filter	At 2009.0 (mag)	Slope (mmag yr^{-1})	0 mag Flux (ph m^{-2} s^{-1})[d]	$V = 0$ (mag)[e]	0 mag Flux (ph m^{-2} s^{-1})[d]	$V = 0$ (mag)[e]
SOHO LASCO C2	Orange	11.81 ± 0.02	-2.8 ± 0.6	8.6×10^9	-0.94	$(8.7 \pm 1.3) \times 10^9$	-0.94 ± 0.16
	Blue	10.81 ± 0.06		–	–	–	–
SOHO LASCO C3	Clear[f]	11.11 ± 0.02	-1.9 ± 0.4	$(2.9 \pm 0.2) \times 10^{10}$	$+0.39 \pm 0.05$	$(2.7 \pm 0.4) \times 10^{10}$	$+0.31 \pm 0.16$
	Orange	9.48 ± 0.04		8.6×10^9	-0.94	$(8.7 \pm 1.3) \times 10^9$	-0.94 ± 0.16
	Blue	8.24 ± 0.05		–	–	–	–
	Deep Red[g]	9.53 ± 0.05		–	–	–	–
STEREO HI1[h]	–	–	–	$(4.7 \pm 0.7) \times 10^{10}$	$+0.89 \pm 0.16$	$(5.3 \pm 0.7) \times 10^{10}$	$+1.02 \pm 0.15$

[a]Fitted zero-point linear model, with intercept at year 2009.0. Slopes fitted only for C2 Orange and C3 Clear, and assumed to be identical for the other C2 and C3 bandpasses.

[b]Relative sensitivity to Na I D emission expected from LASCO bandpass profiles and HI1 Mercury tail observations.

[c]Na I D sensitivity metrics corrected from fit to Phaethon's photometry.

[d]Na I D flux producing magnitude 0.

[e]Magnitude of a Johnson $V = 0$ source emitting only Na I D.

[f]A priori Na I D calibration based on assumed bandpass, as described in text.

[g]Not used for Phaethon observations; included for reference only.

[h]From STEREO-A HI1 calibration in Appendix 4.6.1; STEREO-B treated as identical.

Clapyeron relation, the vapor pressure over a surface of temperature T comprised of a substance with a unit latent heat of sublimation L is

$$P_v(T) = P_0 \exp\left(-\frac{L}{k_B}\left(\frac{1}{T} + \frac{1}{T_0}\right)\right) \tag{4.2}$$

where k_B is the Boltzmann constant, $P_0 \equiv 398$ MPa, and T_0 is a material-dependent temperature with $T_0 \sim 5000$ K for typical refractory, asteroidal materials (Cranmer 2016). For metallic Na, $L = 1.097$ eV atom^{-1} = 105.8 kJ mol^{-1} and $T_0 = 4660$ K (Huebner 1970).

Phaethon's surface, however, is likely not comprised of a single substance, but instead of a number of different materials spanning a wide range of volatility each with their own unique vapor pressure functions. For simplicity, we assume the observed Na I originates exclusively from a single volatile substance—which we assume is pure Na, but could in theory be an Na-bearing compound that only later produces Na I upon dissociation—that is embedded within an otherwise perfectly refractory substrate that contributes no additional vapor pressure.

Suppose momentarily that this Na were segregated in large, macroscopic clumps covering a fraction f_{eff} of the surface, and thus occupying a volume fraction f_{eff} of the surface material. The effective vapor pressure over the surface—and thus the expected Na I production rate—would be f_{eff} times that of if the volatile covered the full surface. In reality, the Na is unlikely be segregated in this manner, and is most likely more finely divided throughout the refractory substrate to which the atoms are largely individually bonded. Moreover, the steep dependence of vapor pressure and thus Na loss on temperature likely causes the surface material within the upper few centimeters, which reaches subsolar temperatures of ~1000 K near perihelion, to fully devolatilize within hours of exposure to such temperatures, as Masiero et al. (2021) experimentally demonstrated for chrondritic meteorites serving as analogs to Phaethon's surface.

As we have found no evidence for ongoing resurfacing activity clearing the devolatilized surface material, we presume the sources of Na responsible for the observed activity are sequestered some distance beneath the surface where cooler peak temperatures have sufficiently slowed their depletion for their continued presence. We model the subsurface Na abundance as a step function, with 0% Na in the devolatilized layer and a constant effective Na fraction f_0 beneath. We found in Section 4.3.2.1 that the peak in Phaethon's Na I production lagged its perihelion

by (3.0 ± 0.8) h, a value comparable to its 3.6 h rotation period; if fully attributed to the thermal propagation time into the active subsurface layer, the observed offset suggests the devolatilized layer extends to roughly the diurnal skin depth, a thickness of $\Delta z \sim 0.1$ m.

Under this revised picture, f_{eff} evidently no longer measures the now ~0% surface Na content, but still serves as a proxy for subsurface volatility that encapsulates both the actual subsurface Na abundance below the devolatilized layer and the resistance of this devolatilized layer to the diffusion of Na I through it. We use the model by Schorghofer (2008) for the sublimation through a medium of porosity $\phi \sim 0.5$, grain radii $R_g \sim 0.1$ mm, and tortuosity $\tau_{\text{tort}} \sim 1$, as assumed by Masiero et al. (2021), and find the effect of the devolatilized layer on Na desorption below to be

$$\frac{f_{\text{eff}}}{f_0} \approx \frac{4\pi\phi R_g}{(8+\pi)(1-\phi)\tau_{\text{tort}}\Delta z} \sim 10^{-3} \tag{4.3}$$

indicating that such a devolatilized layer can indeed significantly suppress Na loss from below. We caution, however, that the lack of reliable constraints on the input parameters limits this estimate to an order of magnitude uncertainty at best.

One additional consequence of the Na being largely sequestered beyond the diurnal skin depth is that Na desorption should have little diurnal variation, as the temperature of the Na-bearing subsurface remains near the diurnally-averaged surface temperature at all times. As Phaethon is near equinox at perihelion, its subsurface temperature there and thus Na I production likely exhibits only minimal day–night asymmetry, although the latitudinal variation in diurnally-averaged insolation will still restrict the strongly temperature-dependent Na desorption to a fraction $f_T < 1$ of the surface at any instant.

At its fitted $n = 13.7 \pm 0.5$, Phaethon's Na I production falls off to 1/2 the peak rate at 1.05× its perihelion distance where solar flux is $1.05^{-2} = 0.90\times$ the perihelion value. If this variation with incident solar flux holds locally across the entire surface, then local Na I loss near perihelion/equinox should fall to 1/2 the equatorial rate at roughly ±25° latitude where insolation is $\cos(25°) \approx 0.90\times$ the equatorial value, bounding an equatorial region with >1/2 the peak Na I flux that occupies a fraction $f_T \approx 0.42$ of Phaethon's surface. This fraction depends slightly on n—increasing to just $f_T \approx 0.52$ at 322P's lower $n = 8.8 \pm 0.3$—as well as on less well-constrained properties including local variation in subsurface Na content/depth, deviations from the modeled spherical shape, and associated seasonal effects.

We then treat this equatorial region of area $4\pi R^2 f_T$ as the only active portion of the radius R asteroid, which we model as having a uniform subsurface temperature T_{Na} equal to the temperature of the desorbed Na I. The Hertz–Knudsen equation then gives

$$\frac{Q(\mathrm{Na\ I})}{4\pi R^2} = \frac{\alpha_s f_T f_{\mathrm{eff}} P_v(T_{\mathrm{Na}})}{\sqrt{2\pi m_{\mathrm{Na}} k_B T_{\mathrm{Na}}}} \tag{4.4}$$

where $m_{\mathrm{Na}} = 23$ u is the atomic mass of Na, and α_s is the sublimation efficiency which we treat as roughly unity, as typical of atoms and small molecules (Van Lieshout et al. 2014). Thermal radiation from the asteroid is set by the actual surface temperature T_s through the Stefan–Boltzmann law integrated over its surface A. The energy balance between the incident solar flux $S(r) = (1361\ \mathrm{W\ m^{-2}}) \times (1\ \mathrm{au}/r)^2$ (Prša et al. 2016) with the outgoing thermal radiation and the sublimation power then gives

$$\begin{aligned}(1 - A_B) S(r) \times \pi R^2 &= \varepsilon \sigma_{\mathrm{SB}} \oiint_A T_s^4 \, dA' + L \times Q(\mathrm{Na\ I}) \\ &\equiv \varepsilon \sigma_{\mathrm{SB}} T_{\mathrm{eff}}^4 \times 4\pi R^2 + L \times Q(\mathrm{Na\ I})\end{aligned} \tag{4.5}$$

for which we choose a convenient Bond albedo $A_B = 0.05$ and effective emissivity $\varepsilon = 0.95$ while neglecting surface roughness and thermal inertia, and defining an effective temperature T_{eff} as the temperature of an isothermal sphere equal in size to and radiating the same power as the actually non-isothermal asteroid. In practice, we found that the $Q(\mathrm{Na\ I})$ of Phaethon, and even of 322P and 323P, are so small that the sublimation term $L \times Q(\mathrm{Na\ I})$ actually contributes negligible cooling for all plausible L, so T_{eff} becomes well-approximated at all relevant r by the standard isothermal blackbody temperature

$$T_{\mathrm{eff}}(r) \approx \left(\frac{S(r)}{4\sigma_{\mathrm{SB}}} \right)^{1/4} \equiv T_1 \times \sqrt{\frac{1\ \mathrm{au}}{r}} \tag{4.6}$$

with $T_1 = 278$ K, giving $T_{\mathrm{eff}}(0.14\ \mathrm{au}) = 743$ K at Phaethon's perihelion. We then approximate the subsurface temperature T_{Na} as the surface temperature T_s averaged along the equator (i.e., the diurnally-averaged temperature at any point on the equator). The relation between T_{Na} and T_{eff} is therefore dependent on the thermal properties of the surface material. For a crude, NEATM-like $T_s \propto (\cos\psi)^{1/4}$ at solar zenith angles $\psi < 90°$ that neglects nightside surface temperature (Harris

1998), we find $T_{\mathrm{Na}} \approx 0.6 T_{\mathrm{eff}}$. However, thermophysical modeling of Phaethon by both Yu et al. (2019) and Masiero et al. (2021) found equatorial nightside surface temperatures near perihelion to be a non-negligible ~50% of the subsolar temperature (~1000 K), which raises the diurnally-averaged equatorial temperature to a much higher $T_{\mathrm{Na}} \approx T_{\mathrm{eff}}$. We therefore adopt this value as our nominal estimate for the temperature driving Na desorption.

With their model, Yu et al. (2019) actually computed slightly higher peak diurnally-averaged surface temperatures of ~800 K. Masiero et al. (2021), meanwhile, directly computed the perihelion temperature of material ~0.1 m beneath the surface at near-equatorial latitudes and found it to be a slightly cooler ~600–700 K, possibly due in part to thermal lag shifting the peak subsurface temperatures to a few hours after perihelion. Given these comparisons, we consider our $T_{\mathrm{Na}} \approx T_{\mathrm{eff}}$ approximation likely accurate to ±100 K at Phaethon's perihelion, corresponding to ±37 K in T_1.

With this subsurface temperature model, Na I production scales with r as

$$Q(\mathrm{Na\ I}) \propto r^{1/4} \exp\left(-\frac{L}{k_B T_1} \times \sqrt{\frac{r}{1\ \mathrm{au}}}\right) \tag{4.7}$$

The logarithmic slope of Na I with r then becomes a pure function of r and L:

$$n \equiv -\frac{\partial \ln Q}{\partial \ln r} = \frac{L}{2 k_B T_1} \times \sqrt{\frac{r}{1\ \mathrm{au}}} - \frac{1}{4} \tag{4.8}$$

Phaethon's fitted $n = 13.7 \pm 0.5$ is considerably steeper than the $n = 9.6 \pm 0.8$ expected for metallic Na at $r = 0.14$ au, and instead corresponds to Na more tightly bound with $L = (1.8 \pm 0.2)$ eV atom^{-1} = (170 ± 20) kJ mol^{-1}. Phaethon's $Q(\mathrm{Na\ I}) = (5.5 \pm 0.8) \times 10^{23}$ atoms s^{-1} at $r = 0.14$ au then corresponds to an effective Na fraction of $f_{\mathrm{eff}} = 10^{-4.5 \pm 0.5}$ by Equation (4.4)—equivalent to a subsurface Na fraction $f_0 \sim 10^{-2}$–10^{-1} beneath the $\Delta z \sim 0.1$ m thick devolatilized layer by Equation (4.3), which we consider broadly consistent with the ~0.5% Na mass abundance typical of chondritic meteorites (Lodders 2021) given the abundance of poorly-constrained parameters contained in these estimates.

This model can also set a rough bound on the age of Phaethon's surface t_1 since it was last resurfaced (i.e., when $f_{\mathrm{eff}}/f_0 \approx 1$). Treating f_0 as approximately an Na mass fraction, Phaethon's current orbitally averaged Na I loss rate $\bar{Q} = (1.05 \pm 0.15) \times 10^{29}$ atoms orbit^{-1} = $(7.3 \pm 1.0) \times 10^{28}$ atoms yr^{-1} deepens the devolatilized layer at a rate

$$\Delta\dot{z} \sim \frac{\bar{Q} m_{\mathrm{Na}}}{4\pi R^2 \rho f_0} \sim 10^{-14}\ \mathrm{m\ s^{-1}} \tag{4.9}$$

for Phaethon's radius $R = 2.7$ km and bulk density $\rho = 1.6$ g cm^{-3} (MacLennan et al. 2021).

More generally, $\bar{Q} \propto f_{\mathrm{eff}}$ at constant T, by Equation (4.4), and $f_{\mathrm{eff}} \propto 1/\Delta z$, by Equation (4.3), and $\Delta\dot{z} \propto \bar{Q} \propto 1/\Delta z$. Then, after integrating time $0 \rightarrow t_1$ corresponding to f_{eff} from f_0 to its current $\sim 10^{-3} f_0 \ll f_0$:

$$\Delta z \propto t_1^{1/2} \implies \frac{\Delta\dot{z}}{\Delta z} \sim \frac{1}{2t_1} \tag{4.10}$$

Then, $t_1 \sim \Delta\dot{z}/(2\Delta z) \sim 10^4$ yr for the current values of $\Delta\dot{z}$ and Δz. In reality, the Na increasingly deviates from the isothermal blackbody temperature at lower Δz, where Na is closer to the surface and thus experiences more extreme diurnal temperature fluctuations. Under those past conditions, $\bar{Q}$ and thus $\Delta\dot{z}$ would both be higher than these scaling approximation imply, so the computed t_1 actually reflects a rough upper bound on the surface age of $\lesssim 10^4$ yr.

We caution that this age may not necessarily be the actual time since the surface was last cleared, but rather the cumulative duration over which the surface has experienced a comparable degree of heating as on its present orbit. Phaethon has only spent ~10 kyr total at $q \lesssim 0.15$ au over the past 100 kyr, so our $\lesssim 10^4$ yr bound remains insufficient to distinguish a true resurfacing event, as might be associated with the Geminids formation, from the brevity of Phaethon's sunskirting history. More useful bounds require higher precision calculations, likely from proper thermophysical and dynamical modeling in conjunction with better constrained surface material properties.

4.6.4 Sodium Tail Model

Here, we describe a numerical model for the brightness profile of a predominantly optically thin Na I tail, which we used to quantify the Na I D emission of Phaethon and other sunskirting objects.

We begin with a fully optically thin tail model, similar to those previously used by Cremonese et al. (1997) and Schmidt et al. (2010b). We model Na I fluorescence with two independent two-level systems corresponding to the 589.0 nm D_2 and 589.6 nm D_1 transitions, and treat the instantaneous fraction of excited atoms as

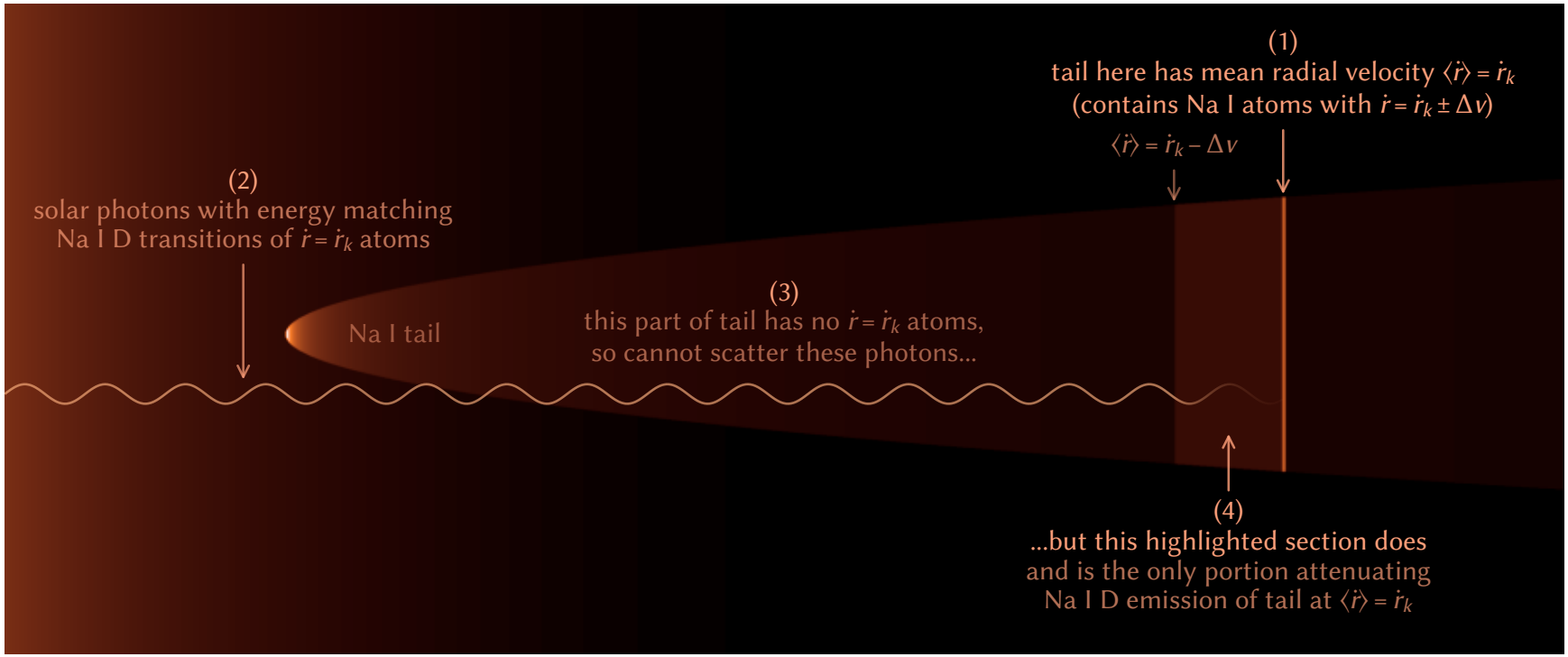

Figure 4.14: Illustration explaining the Na I tail model's simplified treatment of optical depth along the tail, where only the Na I atoms immediately sunward of any point along the tail contribute to the attenuation of Na I D emission at that point.

zero, neglecting the impact of other transitions, as appropriate for Na I excited only by stimulated absorption of solar photons. We use Na I D transition parameters from Sansonetti (2008) and the disk-averaged solar spectrum from Neckel (1999) to compute the corresponding fluorescence efficiencies (emission rates per atom) as functions of heliocentric distance r and radial velocity $\dot{r}$, capturing the Swings effect (Swings 1941). We correct for anisotropic scattering by the D_2 line by multiplying its contribution to the flux observed at phase angle α by $0.967 \times (1 + 0.102 \cos^2 \alpha)$ (Chamberlain 1961).

Next, we numerically integrate the motion of an atom released at initial $r = r_0$ and $\dot{r} = \dot{r}_0$, and accelerated antisunward at $\ddot{r}$ by the momentum transfer of $D_2 + D_1$ absorption. The linear tail brightness profile for an Na I source at this r_0 and $\dot{r}_0$ then corresponds to the emission rate at the r and $\dot{r}$ along the tail, divided by $\dot{r} - \dot{r}_0$ into an emission rate per unit length, and modulated by the photoionization of Na I. We initially used a photoionization rate of $(7.59 \times 10^{-6}\ \mathrm{s}^{-1}) \times (1\ \mathrm{au}/r)^2$ from the mean of the quiet and active Sun rates found by Huebner & Mukherjee (2015), but also later directly fitted for (the reciprocal of) this value in Section 4.3.2.1.

We crudely estimate the Na I outflow speed v_{out} as the thermal speed $(8k_B T(r)/(\pi m_{\mathrm{Na}}))^{1/2}$ for the isothermal blackbody temperature $T(r)$ from Equation (4.6). These values theoretically influence the morphology of an optically thin Na I tail in two distinct ways, although neither actually substantially affects our modeling of LASCO/HI1 observations of sunskirting objects:

1. A population of Na I with a broadly distributed $\dot{r}$ around a mean $\langle \dot{r} \rangle$ will sample a broad region of the solar spectrum, and thus fluoresce with different efficiency than a different population of Na I where all atoms have the $\dot{r} = \langle \dot{r} \rangle$. We approximated this effect by taking an ensemble average of tail profiles with initial $\dot{r}$ normally distributed about the nominal $\dot{r}_0$ with standard deviation v_{out}, but found its impact to be minimal at the $v_{\mathrm{out}} \sim 1$ km s^{-1} of sunskirting objects. The solar spectrum near the Na I D lines is fairly smooth at ~ 1 km s^{-1} scales, and requires much a wider spread in $\dot{r}$ before any difference in fluorescence efficiency becomes noticeable.

2. The outflow speed becomes the expansion rate of Na I parcels propagating down the tail, which sets the tail width of the portion with Na I age t at $2v_{\mathrm{out}}t$. LASCO and HI1, however, cannot resolve the width of Phaethon's tail near perihelion: in one $t \sim 0.8$ h photoionization lifetime at $r = 0.14$ au,

the tail broadens to only $2v_{\rm out}t \sim 5000$ km, or $\sim 7''$ from the closest distance $\Delta = 0.86$ au—below the $12''$ pixel scale of our highest resolution, LASCO C2 imagery. Rapid photoionization limits the broadening of Na I tails of other sunskirting objects at lower r to be even narrower.

Now, we consider the impact of optical depth on tail profiles. A rigorous optically thick model with proper treatment of multiple scattering and particle dynamics would be far too computationally intensive for our analysis. Instead, we use a leading order approximation at low optical depths that neglects the impact of optical depth on the acceleration of Na I. This simplification allows the use of the optically thin linear Na I density Λ to derive the optical depth and associated dimming along the tail.

The principal effect of optical depth is to reduce the number of scatterable solar Na I D photons surviving into the tail before being scattered out of the tail by Na I, and thus reduce the effective fluorescence efficiency of atoms in the tail. While scattered Na I D photons can be rescattered by additional Na I atoms on their way out of the tail, one scattered Na I D photon will eventually escape the tail for every solar photon that excites an Na I atom in the tail. The optical depth along the observer line of sight should therefore only minimally affect the observed tail brightness through anisotropic redirection of scattered Na I D photons, favoring directions out of the tail with relatively lower optical depth, which we neglect in our model.

A solar photon can only be scattered by an Na I atom if it has a wavelength λ matching that of one of the Na I D lines in the rest frame of the atom, neglecting the natural line shapes. In practice, the Na I will have some nonzero velocity dispersion Δv, so any portion of the tail can scatter solar photons within a Doppler shift of $\pm\Delta v$. The $\dot{r}$ increases monotonically along the tail, so for each point along the tail with mean radial velocity $\dot{r}$, only the atoms directly sunward of that point with mean radial velocity between $\dot{r} - \Delta v$ and $\dot{r}$ contribute to the optical depth, corresponding to a segment of tail $L = \Delta v \times \dot{r}/\ddot{r}$ in length. Figure 4.14 illustrates this explanation.

We then model the tail as a series of these independent, cylindrical segments, where each segment corresponding to Na I atoms of age t has radius $v_{\rm out}t$, and therefore volumetric number density $N = \Lambda/(\pi v_{\rm out}^2 t^2)$. We define $\sigma_k \propto \Delta v^{-1}$ as the effective scattering cross section of Na I atoms to scatterable photons within a $\pm\Delta v$ Doppler shift of the Na I D_k line, for which $\sigma_2 \Delta v = (5.0 \times 10^{-13})$ m^3 s^{-1} and

$\sigma_1 \Delta v = (2.5 \times 10^{-13})$ m^3 s^{-1}. The optical depth of the D$_k$ line for each segment is then

$$\begin{aligned} \tau_k &= NL\sigma_k \\ &= \frac{\Lambda}{\pi v_{\text{out}}^2 t^2} \times \frac{\Delta v \times \dot{r}}{\ddot{r}} \times \sigma_k \\ &= \frac{\Lambda \dot{r}}{\ddot{r} t^2} \times \frac{\sigma_k \Delta v}{\pi v_{\text{out}}^2} \end{aligned} \tag{4.11}$$

which we note does not actually depend on any particular choice of Δv, since Δv is only included as part of the fixed factor $\sigma_k \Delta v$. We also note that $\tau_k \propto r^{-2} \propto T^{-1}$, so the optical depth is actually somewhat sensitive to our crudely estimated Na I temperature, although the overall impact of this large uncertainty on the actual tail profile remains minimal at the low optical depths for which this model is valid.

Finally, we modulate the optical thin Na I D$_k$ fluorescence efficiency along the tail by a factor of $(1 - \exp(-\tau_k))/\tau_k$ to produce our final estimate for the tail brightness profile. We caution that since $\tau_k \to \infty$ as $t \to 0$, even low Q(Na I) sources can produce a section of optically thick tail that may not be well-reproduced by this model. However, our model suffices to confirm that Phaethon's observable Na I tail is largely optically thin—with optical depth affecting its integrated brightness by up to only ~10%—which validates the physical parameters we fit under that assumption.

References

Abe, S., Ogawa, T., Maeda, K., & Arai, T. 2020, P&SS, 194, 105040

Adel, A., Slipher, V., & Ladenburg, R. 1937, ApJ, 86, 345

Arai, T., Kobayashi, M., Ishibashi, K., et al. 2018, LPI, 49, 2570

Asher, D., Bailey, M., Hahn, G., & Steel, D. 1994, MNRAS, 267, 26

Battams, K., & Knight, M. M. 2017, RSPTA, 375, 20160257

Battams, K., & Watson, A. 2009, IAUC, 9054, 3

Bewsher, D., Brown, D., Eyles, C., et al. 2010, SoPh, 264, 433

Biesecker, D., Lamy, P., Cyr, O. S., Llebaria, A., & Howard, R. 2002, Icar, 157, 323

Binzel, R. P., Harris, A. W., Bus, S. J., & Burbine, T. H. 2001, Icar, 151, 139

Blaauw, R. 2017, P&SS, 143, 83

Bodewits, D., Farnham, T. L., Kelley, M. S., & Knight, M. M. 2018, Natur, 553, 186

Borovička, J., Koten, P., Spurnỳ, P., et al. 2010, in Icy Bodies of the Solar System, Vol. 263 (Cambridge University Press), 218–222

Bottke Jr, W. F., Morbidelli, A., Jedicke, R., et al. 2002, Icar, 156, 399

Brown, D., Bewsher, D., & Eyles, C. 2009, SoPh, 254, 185

Brown, M., Bouchez, A., Spinrad, H., & Misch, A. 1998, Icar, 134, 228

Brueckner, G., Howard, R., Koomen, M., et al. 1995, SoPh, 162, 357

Cassidy, T., Schmidt, C., Merkel, A., Jasinski, J., & Burger, M. 2021, PSJ, 2, 175

Chamberlain, J. W. 1961, Physics of the Aurora and Airglow (Academic Press)

Colaninno, R., & Howard, R. 2015, SoPh, 290, 997

Combi, M., Fougere, N., Mäkinen, J., et al. 2014, ApJL, 788, L7

Combi, M. R., DiSanti, M. A., & Fink, U. 1997, Icar, 130, 336

Cranmer, S. R. 2016, EM&P, 118, 51

Cremonese, G., Boehnhardt, H., Crovisier, J., et al. 1997, ApJL, 490, L199

Davies, J., Green, S., Stewart, B., Meadows, A., & Aumann, H. 1984, Natur, 309, 315

de León, J., Campins, H., Tsiganis, K., Morbidelli, A., & Licandro, J. 2010, A&A, 513, A26

Decock, A., Jehin, E., Hutsemekers, D., & Manfroid, J. 2013, A&A, 555, A34

Domingo, V., Fleck, B., & Poland, A. I. 1995, SoPh, 162, 1

Evans, C., & Malville, J. M. 1967, PASP, 79, 310

Eyles, C., Harrison, R., Davis, C. J., et al. 2009, SoPh, 254, 387

Farnham, T. L., Schleicher, D. G., & A'Hearn, M. F. 2000, Icar, 147, 180

Finson, M., & Probstein, R. F. 1968, ApJ, 154, 327

Foreman-Mackey, D., Hogg, D. W., Lang, D., & Goodman, J. 2013, PASP, 125, 306

Fox, K., Williams, I. P., & Hughes, D. W. 1984, MNRAS, 208, 11P

Fulle, M., Leblanc, F., Harrison, R., et al. 2007, ApJ, 661, L93

Gaia Collaboration, Vallenari, A., Brown, A., Prusti, T., et al. 2022, arXiv:2208.00211

Gardès, B., Lamy, P., & Llebaria, A. 2013, SoPh, 283, 667

Granvik, M., Morbidelli, A., Jedicke, R., et al. 2016, Natur, 530, 303

Green, S., Meadows, A., & Davies, J. 1985, MNRAS, 214, 29P

Greenstein, J. 1958, ApJ, 128, 106

Gustafson, B. Å., Kolokolova, L., Xu, Y.-l., Greenberg, J. M., & Stognienko, R. 2001, in Interplanetary Dust (Springer), 509–567

Gustafson, B. Å. S. 1989, A&A, 225, 533

Halain, J.-P. 2012, PhD thesis, Université de Liège

Hanuš, J., Delbo, M., Vokrouhlickỳ, D., et al. 2016, A&A, 592, A34

Hanuš, J., Vokrouhlickỳ, D., Delbo, M., et al. 2018, A&A, 620, L8

Harris, A. W. 1998, Icar, 131, 291

Holt, C. E., Knight, M. M., Kelley, M. S., et al. 2022, PSJ, 3, 187

Howard, R. A., Moses, J., Vourlidas, A., et al. 2008, SSRv, 136, 67

Hsieh, H. H., & Jewitt, D. 2005, ApJ, 624, 1093

Huebner, W. 1970, A&A, 5, 286

Huebner, W., & Mukherjee, J. 2015, P&SS, 106, 11

Huebner, W. F., Keady, J. J., & Lyon, S. 1992, Ap&SS, 195, 1

Huggins, W. 1882, Natur, 26, 179

Hui, M.-T. 2023, AJ, 165, 94

Hui, M.-T., & Li, J. 2017, AJ, 153, 23

Hui, M.-T., Tholen, D. J., Kracht, R., et al. 2022, AJ, 164, 1

Jewitt, D. 2005, AJ, 129, 530

Jewitt, D., Asmus, D., Yang, B., & Li, J. 2019, AJ, 157, 193

Jewitt, D., & Li, J. 2010, AJ, 140, 1519

Jewitt, D., Li, J., & Agarwal, J. 2013, ApJL, 771, L36

Jones, G. H., Knight, M. M., Battams, K., et al. 2018, SSRv, 214, 20

Kaiser, M. L., Kucera, T., Davila, J., et al. 2008, SSRv, 136, 5

Kimura, H. 2017, ApJL, 839, L23

Knight, M. M., A'Hearn, M. F., Biesecker, D. A., et al. 2010, AJ, 139, 926

Knight, M. M., & Battams, K. 2014, ApJL, 782, L37

Knight, M. M., Fitzsimmons, A., Kelley, M. S., & Snodgrass, C. 2016, ApJL, 823, L6

Lamy, P., Faury, G., Llebaria, A., et al. 2013, Icar, 226, 1350

Lamy, P. L., Toth, I., & Weaver, H. A. 2014, ApJL, 794, L9

Li, J., & Jewitt, D. 2013, AJ, 145, 154

Lierle, P., Schmidt, C., Baumgardner, J., et al. 2022, PSJ, 3, 87

Lisse, C., & Steckloff, J. 2022, Icar, 381, 114995

Llebaria, A., Lamy, P., & Danjard, J.-F. 2006, Icar, 182, 281

Lodders, K. 2021, SSRv, 217, 1

MacLennan, E., Marshall, S., & Granvik, M. 2022, Icar, 388, 115226

MacLennan, E., Toliou, A., & Granvik, M. 2021, Icar, 366, 114535

Madey, T. E., Yakshinskiy, B. V., Ageev, V. N., & Johnson, R. E. 1998, JGRE, 103, 5873

Mann, I., Kimura, H., Biesecker, D. A., et al. 2004, SSRv, 110, 269

Marcus, J. N. 2007, ICQ, 29, 39

Marshall, S., Devogele, M., Taylor, P., et al. 2022, in AAS/DPS Meeting, Vol. 54, 514.07

Masiero, J. R., Davidsson, B. J., Liu, Y., Moore, K., & Tuite, M. 2021, PSJ, 2, 165

Muinonen, K., Belskaya, I. N., Cellino, A., et al. 2010, Icar, 209, 542

Nakano, R., & Hirabayashi, M. 2020, ApJL, 892, L22

Neckel, H. 1999, SoPh, 184, 421

Newall, H. 1910, MNRAS, 70, 459

Oppenheimer, M. 1980, ApJ, 240, 923

Ossing, D. A., Cox, M. W., Wilson, D., et al. 2018, in SpaceOps Conference, Vol. 2018, 2565

Ozaki, N., Yamamoto, T., Gonzalez-Franquesa, F., et al. 2022, AcAau, 196, 42

Pearce, J. 1921, JRASC, 15, 364

Potter, A., Killen, R., & Morgan, T. 2002, M&PS, 37, 1165

Prša, A., Harmanec, P., Torres, G., et al. 2016, AJ, 152, 41

Ryabova, G. 1999, SoSyR, 33, 224

Sansonetti, J. 2008, JPCRD, 37, 1659

Schleicher, D. G., & Bair, A. N. 2011, AJ, 141, 177

Schmidt, C., Baumgardner, J., Mendillo, M., Davis, C., & Musgrave, I. 2010a, in AAS/DPS Meeting, Vol. 42, 21.05

Schmidt, C. A., Baumgardner, J., Mendillo, M., & Wilson, J. K. 2012, JGRA, 117, A03301

Schmidt, C. A., Johnson, R. E., Baumgardner, J., & Mendillo, M. 2015, Icar, 247, 313

Schmidt, C. A., Wilson, J. K., Baumgardner, J., & Mendillo, M. 2010b, Icar, 207, 9

Schorghofer, N. 2008, ApJ, 682, 697

Sekanina, Z. 2003, ApJ, 597, 1237

—. 2022, arXiv:2202.01164

Sekanina, Z., & Kracht, R. 2014, arXiv:1404.5968

—. 2016, ApJ, 823, 2

Strom, R. 2002, A&A, 387, L17

Swings, P. 1941, LicOb, 19, 131

Tappin, S., Eyles, C., & Davies, J. 2017, SoPh, 292, 28

—. 2022, SoPh, 297, 37

Thernisien, A., Morrill, J., Howard, R., & Wang, D. 2006, SoPh, 233, 155

Thernisien, A., Morrill, J., Llebaria, A., et al. 2003, in AGUFM, Vol. 2003, SH41B–0461

Van Lieshout, R., Min, M., & Dominik, C. 2014, A&A, 572, A76

Vokrouhlickỳ, D., Bottke, W., Chesley, S., Scheeres, D., & Statler, T. 2015, The Yarkovsky and YORP Effects (Tucson, AZ: Univ. of Arizona Press), 509–531

Weissman, P. R., & Lowry, S. C. 2008, M&PS, 43, 1033

Whipple, F. L. 1951, ApJ, 113, 464

—. 1983, IAUC, 3881, 1

Wiegert, P. A., Houde, M., & Peng, R. 2008, Icar, 194, 843

Williams, I., & Wu, Z. 1993, MNRAS, 262, 231

Willmer, C. N. 2018, ApJS, 236, 47

Ye, Q., & Granvik, M. 2019, ApJ, 873, 104

Ye, Q., Knight, M. M., Kelley, M. S., et al. 2021, PSJ, 2, 23

Yu, L. L., Ip, W. H., & Spohn, T. 2019, MNRAS, 482, 4243

Chapter 5

CONCLUSIONS

A wide range of small objects in the solar system exhibit comet-like characteristics at some point in their evolution, whether physically or behaviorally. The preceding chapters explored a small sample of these "cometoids" at various evolutionary stages in distinct regions of the solar system.

Chapter 2 presented the results of an occultation survey constraining the size distribution of kilometer-scale objects in the Kuiper Belt—the distant population from which Jupiter-family comets are sourced. This size distribution would be useful to compare against the more easily characterized properties of these directly observable comets to evaluate the physical evolution after solar heating. However, the star field chosen for the survey proved too dense for the accurate photometry of individual stars needed to isolate occultations, resulting in a considerable loss of sensitivity yielding final constraints comparable to results obtained by prior surveys.

A future occultation survey of a similar design would benefit in efficacy from choosing a lower density field with cleanly separated stars, with the loss in stars potentially offset through the use of larger sensors provided by recent advancements in imaging technology. A survey sufficiently sensitive to provide a large sample of occultations—calibrated with a similarly sensitive control sample to validate those events—will constrain not only the size distribution, but also the spatial (distance and inclination) distribution of these otherwise invisible objects, details useful for dynamical modeling of the solar system.

Chapter 3 used color imaging and imaging polarimetry to explore the pre-perihelion behavior of dust from the dynamically new comet C/2017 K2 (PANSTARRS) before it entered the inner solar system directly from the Oort Cloud. The comet exhibited an optical halo of dust around the nucleus with a relatively bluer color and weaker polarization than the outer coma, which, together with the coma brightness profile, suggests the nucleus may be surrounded with an abundance of micron-sized water ice grains that sublimate as they drift away.

Such a feature does not appear common for dynamically older comets, but the sample of comets with simultaneously measured color and polarization in the outer solar system remains too small for statistically robust conclusions. One other useful

comparison of this result would be against this same comet at the same distance post-perihelion, to evaluate if the comet retains this halo or if the typical fading of dynamically new comets could be explained by changes in dust properties arising from changes in nucleus surface characteristics after heating. A larger sample of similar observations will, of course, again be needed to generalize any conclusions.

Chapter 4 investigated (3200) Phaethon, an object physically dissimilar to classical comets with its lack of ice and apparent origin within the inner solar system, yet regularly exhibits comet-like activity near the Sun from volatilization of sodium. This activity appears similar to that of numerous objects designated as comets found by SOHO's LASCO coronagraphs, suggesting these may share physical similarities with Phaethon. It remains unclear, however, what fraction of these objects were always asteroidal having formed with low ice content, and what fraction are devolatilized nuclei of classical comets that have exhausted their ice from time spent near the Sun.

Closer investigation of members of known, classical cometary fragmentation families in comparison with these near-Sun objects of potentially asteroidal origin may reveal differences in formation characteristics surviving the deep thermal processing all of these objects have experienced. Such characterization will be useful for tracking and comparing the end-states of objects from the Oort Cloud, Kuiper Belt, and the asteroid belt, which probes differences in their structure and composition, and thus formation environment in the early solar system.

The aging SOHO spacecraft and its LASCO coronagraphs are set to be replaced in the next few years, with new Compact Coronagraph (CCOR) instruments set to be launched with a series of National Oceanic and Atmospheric Administration (NOAA) spacecraft. Unlike LASCO, these CCOR units were not principally designed for scientific investigations, but rather to support realtime space weather forecasting, and trade many of LASCO's capabilities—including interchangeable color filters, polarizers, and a wider field-of-view—for reduced cost/complexity and increased reliability. Detailed investigations of near-Sun comets may require dedicated instruments designed to safely observe near the Sun with imaging and spectroscopy capabilities beyond the needs of heliospheric monitoring.

Cometary science largely remains an observationally driven field, with new findings often contingent on the cooperation of nature itself. Even the most capable telescopes remain incapable of summoning bright comets favorable for study. New technology, however, has continued to provide access to ever fainter related targets,

opening access in recent decades to populations of objects from the Kuiper Belt down to the surface of the Sun. Minor planet surveys, in particular, have been discovering comets and related objects at increasingly greater distances from the Sun, facilitating the early study of dynamically new comets while less thermally evolved farther into the outer solar system, as well as of near-Sun objects while away from the Sun in observations for comparison with classical comets and asteroids. The upcoming commencement of both the ground-based Rubin Observatory's optical Legacy Survey of Space and Time (LSST) and the NEO Surveyor mission's thermal infrared survey should dramatically improve sensitivity to these faint objects over the next decade.